Master's Thesis
Physical Oceanography

# Wave Measurements Using Ship Mounted Sensors as part of the One Ocean Expedition

Geophysical Institute
University of Bergen


**Author: Judith Thu Ølberg**

Supervisors: Lars Robert Hole, Birgitte Rugaard Furevik and Patrik Bohlinger

June 2023

## Acknowledgements

First, I would like to thank my supervisors for their positive support during this project and for giving me the freedom to form my own thesis. Thanks to Lars Robert Hole and Birgitte Rugaard Furevik for including me in the One Ocean Expedition and giving me the opportunity to sail with Statsraad Lehmkuhl. A special thanks to Patrik Bohlinger for providing model data and teaching me the program Wavy, which has greatly simplified the work of this thesis.

Huge thanks to Fabian Knoblauch for initiating the work on the ship mounted system and sharing the knowledge experienced. Also, thanks to Jean Rabault for providing expertise about the instrumentation.

The warmest thanks to Astrid Bergland for spending two months with me onboard Statraad Lehmkuhl, and help in fixing the wave system and deploying drifters. Also, thanks to Statsraad Lehmkuhl's crew, especially Second Officer Kjell Ove Bongom Smøraas, for helping out with any problem encountered on the ship and for sharing knowledge on sailing.

Lastly, a huge thanks to all fellow students at GFI for making the master studies a memorable time.

**Abstract**

This thesis examines the design and post-processing aspects of wave measurements from ship mounted sensors. The wave measurements exhibit accuracy comparable to wave measuring drifters while offering enhanced spatial coverage and durability. The ship mounted approach is suitable for real-time broadcasting during research expeditions and conventional shipping routes, as well as for the validation of satellite observations and wave models.

The system presented here was deployed on the Norwegian tall ship Statsraad Lehmkuhl during a 22-month circumnavigation of the globe as part of the One Ocean Expedition. The wave measurement system utilizes downward facing altimeter probes to capture sea surface elevation, while ship motion is compensated by inertial motion units. The post-processing of the measurements developed by Knoblauch, 2022 has been corrected, updated, and refined.

With the software update, the significant wave height measurements exhibit a root mean square deviation of 0.36m and a correlation coefficient of 0.96 compared to satellite altimetry. Compared to a third-generation wave model, the root mean squared deviation is 0.53m, and the correlation coefficient is 0.93. The system overestimates the highest waves, particularly during a major winter storm. Regarding peak period measurements, satisfactory results are obtained when waves oppose the sensor and ship speeds remain below 3m/s or when the ship is stationary. Under these circumstances, the root mean squared deviation ranges from 1.76s to 2.04s, while the correlation coefficients range from 0.77 to 0.80, compared to the wave model. However, as ship speeds increase, the quality of peak period measurements deteriorates precipitously, regardless of Doppler shift corrections. The challenges associated with the Doppler shift are suggested to be improved by complementing directional wave- and current measurements from a navigation X-band ship radar.

# Contents

# 1 Introduction

New methods for collecting wave measurements serve both scientific and practical purposes. Wave measurements are essential to advance our understanding of fluxes of mass, momentum, energy, aerosols, carbon dioxide, and other trace gases at the ocean-atmosphere interface (Christensen et al., 2013). Measurements will also contribute to validating satellite observations and numerical wave models, thereby enhancing the accuracy (Amador, Merrifield, and Terrill, 2022). Accurate wave predictions are crucial in navigation and route-choosing routines for maritime transport and fisheries (Cifuentes-Lorenzen et al., 2013). Reliable wave forecasts are also essential to ensure safe offshore operations and design offshore installations according to long-term wave statistics (Reistad et al., 2011).

Waves are measured by in situ instruments deployed on the sea surface or remote sensing instruments mounted above or below the surface (Holthuijsen, 2007a). Traditional in situ instruments are wave buoys and wave staffs, providing high-quality data, but only at specific locations. They are often mounted at existing ocean platforms, concentrated along heavily populated coastlines in the northern hemisphere, leaving many of the open ocean regions critically unsampled (Young, 1999). Certain in situ instruments, such as surface-following drifters and autonomous surface vehicles, can also provide spatial information. Autonomous surface vehicles can be navigated to designated study areas, whereas drifters tend to cluster in eddies or fronts (Amador, Merrifield, and Terrill, 2022). Deploying, maintaining, and recovering these in situ instruments requires costly ship time (Cifuentes-Lorenzen et al., 2013).

Remote sensing instruments may also be installed on stationary and mobile platforms. Fixed offshore structures often employ downward facing radar, laser, or sonic instruments (Bohlinger, Economou, et al., 2023; Malila et al., 2022). These instruments are easy to service and monitor and can operate on long-term resistant to wave-induced damage or loss at sea. Remote observations over larger spatial scales are provided by satellite altimetry, utilized to measure wave field characteristics for many decades (Yang and Zhang, 2019). Altimeters mounted on airplanes, or drones can additionally resolve the directional wave spectra when multiple altimeters are spatially separated (Sun et al., 2005; Pettersson et al., 2003).

A new approach for collecting wave data is to mount downward facing altimeters on ships. Ship mounted instruments can cover great distances of the ocean surface without expensive deployment and retrieval operations (Løken et al., 2021). These instruments can record autonomously and transmit wave parameters in real-time during research expeditions or traditional shipping routes (Christensen et al., 2013). Consequently, they can supplement or replace daily reports from qualified crew members onboard voluntary observing ships (Gulev, Cotton, and Sterl, 1998). A limitation is that the observations acquired from ships will be confined to major shipping routes and avoid extreme weather conditions and the roughest waves.

Wave measuring devices have been installed on ships in the past. Wave staffs mounted at the ship's bow broke at a rate of about two staffs per day due to the mechanical forces in the water (Drennan et al., 1994). Nautical radars on ships operating in X-band wave mode have the advantage of measuring the directional wave spectra, but the wave retrieval method is still under development (Lund, Clarence O. Collins, et al., 2016; Lund, Zappa, et al., 2017; Cifuentes-Lorenzen et al., 2013). Wave properties have also been derived from the vertical position of the vessel recorded by GPS (Clarence O Collins, Rogers, et al., 2015). This approach treats the vessel as a surface following buoy, measuring the low-frequency wave energy. Christensen et al., 2013 presents a methodology combining a downward facing ultrasonic altimeter with the vertical position of the vessel. This combination is expected to perform better, as the altimeter probes facilitate the sampling of higher-frequency waves.

Previous studies with ultrasonic altimeters report the ship mounted system as useful for sig-

nificant wave heights up to 4m, validated against data from conventional wave buoys (Christensen et al., 2013). An ultrasonic sensor of a smaller range exhibited low deviations compared to spectral wave models for significant wave heights up to 1.4m (Løken et al., 2021). A study employing ship mounted laser altimeter reported better performance than the marine X-band radar in estimating significant wave height and lower performance for peak periods (Lund, Zappa, et al., 2017).

Measurements obtained from moving platforms are subject to motion contamination from angular and vertical accelerations and the Doppler effect. Most studies focus on periods when the ship is stationary to avoid the Doppler correction issues. Cifuentes-Lorenzen et al., 2013 studied the motion contamination and found the measurements with laser altimeter adequate at ship speed lower than 3m/s. During rough sea conditions with significant wave heights exceeding 4m, the laser altimeter exhibited more robust estimates than the marine X-band radar. It should be mentioned that Cifuentes-Lorenzen et al., 2013 and Lund, Zappa, et al., 2017 focused on periods when the ship faced the waves to avoid shadowing effects by the ship. A consistent finding across all prior studies is that the ship-mounted instruments demonstrated robustness to enable continuous measurements throughout expeditions lasting up to a maximum duration of one month.

The ship mounted altimeters utilized in this thesis were installed for two years on the Norwegian tall ship Statsraad Lehmkuhl, sailing around the world during the One Ocean Expedition. The wave measurement system incorporates three altimeter probes combined with three motion correction devices installed at the ship's bow (Knoblauch, 2022). Wave measuring surface drifters were deployed from the ship during the expedition to gather wave data for comparison with the ship mounted system. The first drifter deployed in the Caribbean Sea proved robust and well-functioning, with wave statistics within the typical error margin of the direct observation by satellite (Rabault, Nose, et al., 2022). For this thesis, two additional drifters were deployed: one in the North-West Pacific Ocean and the other in the Indian Ocean.

The ship mounted system's accuracy and reliability are evaluated by two key wave parameters: the significant wave height and the peak wave period. Satellite altimeters are utilized to determine the significant wave height due to their ease of processing and high spatial resolution (Young, 1999). Additionally, the third-generation wave model operated by the European Centre for Medium-Range Weather Forecasts provides both wave parameters (ECMWF, 2021b). This wave model offers global coverage and demonstrated superior performance in a comparative study involving five different spectral wave models when evaluated against observations from moored buoys and platforms (Bidlot et al., 2002).

## 1.1 Objectives

This thesis builds upon the research conducted by Knoblauch, 2022 and focuses on the design and post-processing aspects of the ship mounted system installed on the tall ship Statsraad Lehmkuhl. The system is cost-effective, capable of autonomous recording, and adaptable to various platform types, including ships and floating offshore wind turbines, with the potential to significantly increase the number of offshore observations.

The primary objective of this thesis is to provide recommendations for effectively utilizing remote sensing instruments on floating platforms. Specifically, the aim is to determine the optimal instrumentation and positioning of the system based on the data quality and durability of the instruments. Additionally, the influence of ship movement on wave measurements and the contamination caused by the Doppler effect will be investigated. Furthermore, the aim is to improve the system's software and simplify the post-processing routines for future applications. This thesis also seeks to evaluate the accuracy of the wave parameters obtained from

the system and the feasibility of incorporating these parameters into wave validation and data assimilation.

# 2 Data

## 2.1 The Ship Mounted Wave Measurement System

The wave measurement system consists of several instruments at different locations on the ship to find the best instrument combination (Figure 1). It was developed and built by Jean Rabault, Senior Engineer at the Meteorological Institute of Norway, and Fabian Knoblauch as part of his Master's thesis work at The University of Oslo (Knoblauch, 2022). The system comprises three altimeter probes colored blue in Figure 1, three inertial measuring units (IMUs) colored red, and a processing unit colored green.

Two of the altimeter probes operate with ultrasound waves, marked ug1 and ug2, while the third one applies microwaves, marked as radar. The ug1 sensor is placed under the bowsprit tip on steel poles (Figure 2a), while ug2 and radar are mounted on the starboard side of the bow in a solid steel construction (Figure 2b and 2c). The main IMU of the system is safely placed with the processing unit under deck. The extra IMUs are mounted in waterproof cases at exposed locations near the altimeter probes, extra IMU1 at the bowsprit tip, and extra IMU0 at the starboard side of the bow (Figure 1). Table 1 list the horizontal and vertical distance between the main IMU and the extra IMUs, which resembles the distance to the probes.

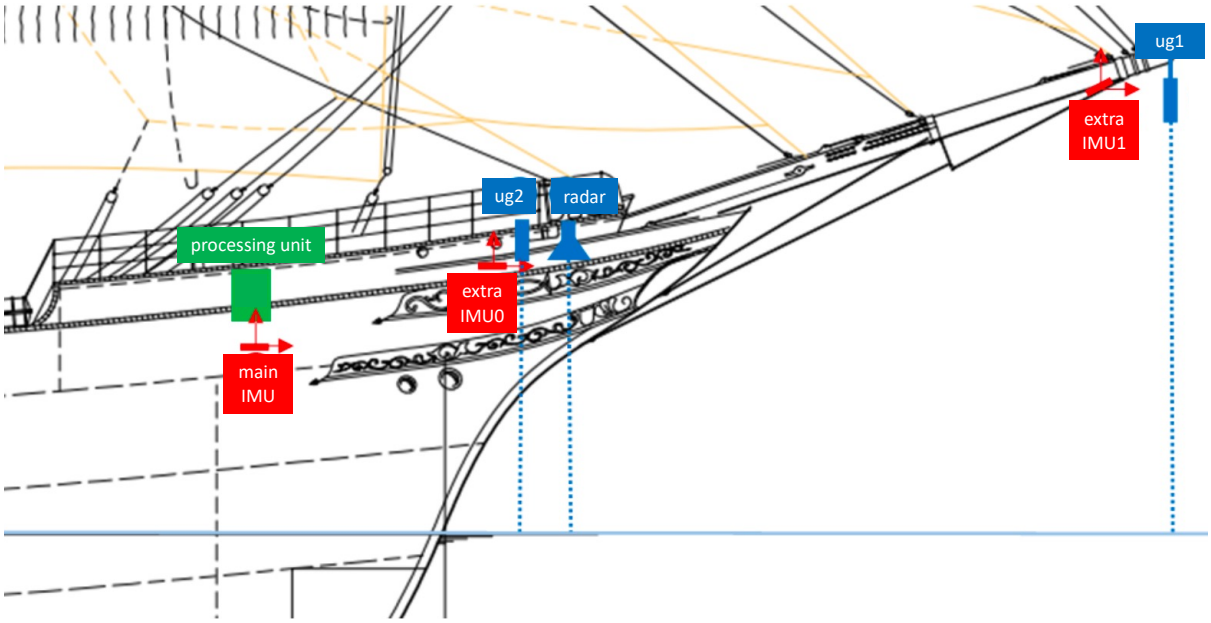


Figure 1: Position of the system components marked on the sketch of Statsraad Lehmkuhl (Knoblauch, 2022). Blue are altimeter probes, red are IMU's and green is the processing unit.

Table 1: Horizontal and vertical distance between the main IMU and extra IMUs (Knoblauch, 2022).

| | From main IMU to extra IMU0 [m] | From main IMU to extra IMU1 [m] |
|---|---|---|
| Horizontal | 4.51 | 19.95 |
| Vertical | 0.98 | 4.82 |

### 2.1.1 Processing Unit

The processing unit comprises affordable, readily available, well-documented hardware such as Arduinos and Raspberry Pis. A Raspberry Pi 4 (RPI) personal computer [1], runs the processing scripts and saves the data. Every 30 minutes, the data measured during the cycle is

[1] https://datasheets.raspberrypi.com/rpi4/raspberry-pi-4-product-brief.pdf

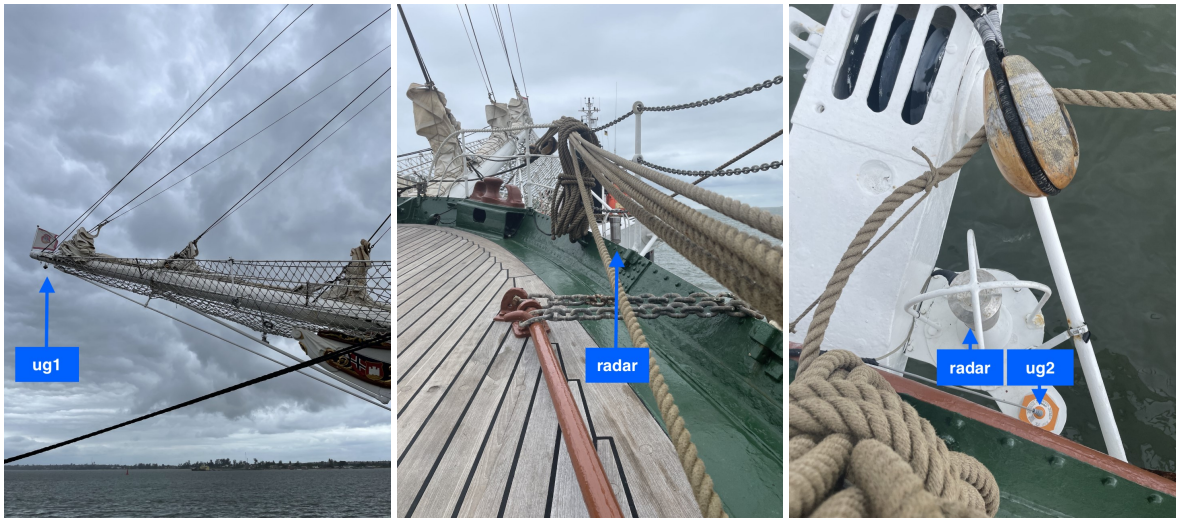


(a) (b) (c)

Figure 2: Pictures of the altimeter probes mounted on Statsraad Lehmkuhl: (a) ug1 under the bowsprit, (b) radar seen from the starboard bow and (c) radar and ug2 in a steel frame on the starboard bow seen from above.

compressed to a lzma file and saved to a connected SSD. The RPI is protected from physical harm and fan cooled by a housing unit. The chosen RPI model does not feature an onboard real-time clock. Therefore an additional clock is fitted to the RPI via a pin connection.

An Arduino Due board [2] process the analog signals of the sensors and sends them to the RPI as binary data packages via a serial connection. An electric circuit shield is pinned on top of the Arduino to handle resistors for amperage to voltage transformation, power distribution for the three altimeter probes, and a voltage-shifting circuit. The main IMU and altimeter probes are connected to the Arduino board and form the main system (left side Figure 3), while the extra IMUs are connected to their own RedBoards[3] (right side Figure 3). They are operating independently of the main system in case of failure of one of the extra IMUs. The RPI is programmed to only reboot if problems occur in the main system. It is linked to the local ship network via an Ethernet cable, allowing the broadcasting of data to the ship's servers and access via SSH connection (Figure 3).

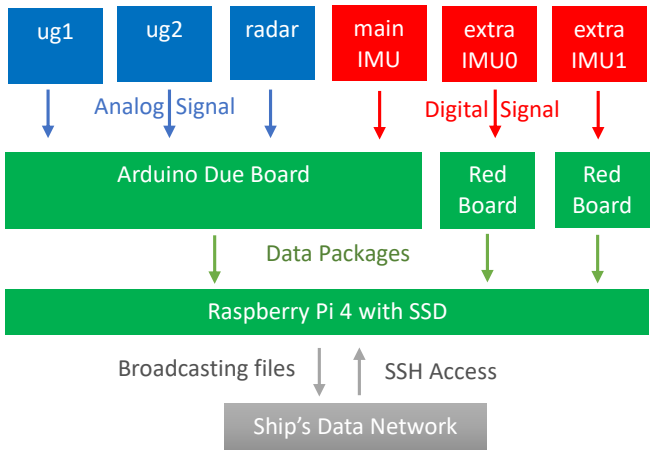


Figure 3: Schematics of the system's data flow (Knoblauch, 2022). The altimeter probes and main IMU form the main system (left), while the extra IMUs operate independently of the main system (right).

[2] https://store.arduino.cc/products/arduino-due
[3] https://www.sparkfun.com/products/15444

### 2.1.2 The Altimeter Probes

The purpose of the altimeter probes is to measure the distance from the ship to the water surface by emitting and receiving reflected signals. Two types of probes are utilized, operating with either ultrasound or microwaves, both from Automation Products Group, Inc. The ultrasonic probes are the model IRU-3433-C60 [4], housed in PC/PET to seal out moisture and resist chemicals. An integrated thermometer compensates the speed of sound in air. At a maximal operating distance, the ultrasonic probe has a minimal response time of 100ms, resulting in a maximal frequency of 10Hz. As radar probe, the True Echo$^{TM}$ Pulse Radar Level Transmitter PRL-050-V024-C4-SS-S6-BF-F [5], with stainless steel horn antenna is used. It is housed in stainless steel material and protected from physical harm with a shield (Figure 2c). During the 2-year expedition period, the instruments should not need any maintenance.

The ultrasonic and radar probes have similar distance ranges of 15.2m and 15m, respectively, and an accuracy of 25% of the detected range (Table 2). The main distinction between them is the transducer frequency and the beam width. Since the beam width of the ultrasonic probe is larger than the radar probe, the maximum footprint diameter is also 32% larger.

Table 2: Specifications of the altimeter probes [4][5].

| | Ultrasonic Probe | Radar Probe |
|---|---|---|
| Distance Range | 0.4 - 15.2m | 0 - 15m |
| Accuracy | $\pm$ 25% of detected range | $\pm$ 25% of measured range |
| Resolution | 2.45 mm | 6.1 $\mu$A |
| Analog output range | 4 - 20 mA | 4 - 20 mA |
| Transducer frequency | 43 kHz | 6.3 MHz |
| Beam Width | 9° | 3° |
| Footprint diameter range | 0.4 - 4.89m | 0 - 1.57m |

### 2.1.3 The Inertial Measurement Units (IMU)

The probes are combined with IMUs to compensate the distance measurements for the ship's motion. IMUs incorporate several physical measurements (3-axis accelerometer, 3-axis gyroscope, and 3-axis magnetometer) with signal processing capabilities in a single device. As a result, the IMU provides the parameters roll, pitch, and yaw, as well as the accelerations in a North-East-Down frame. Two different IMU instruments are utilized in this thesis, with specifications listed in Table 3.

Table 3: Specifications of the IMU sensors[6][7].

| | Main IMU | Extra IMU |
|---|---|---|
| Heave accuracy | 5cm | - |
| Pitch and roll accuracy | 0.5° | - |
| Yaw accuracy | 0.2° | - |
| Yaw range | $\pm$180° | 0-360° |
| Accelerometer range | $\pm$16g | $\pm$16g |
| Gyroscope range | $\pm$2000°/s | $\pm$4000°/s |

The main IMU: VN-100 is produced by VectorNav Technologies[6]. The sensor operates at 800Hz and applies onboard Kalman- together with low-pass filtering of the signal (Rabault, Sutherland, et al., 2020). The IMU is factory calibrated and protected in a robust aluminum closure. The coordinate system of the main IMU is a right-handed Cartesian system with the z-axis pointing downwards. The yaw range is from -180° to 180° (Table 3).

[4] https://www.apgsensors.com/sites/default/files/manuals/IRU-manual.pdf
[5] https://www.apgsensors.com/sites/default/files/manuals/PRL-PRS-manual.pdf
[6] https://www.vectornav.com/products/detail/vn-100

The two extra IMUs are produced by Adafruit [7]. The extra IMUs' purpose is to compare the ship motions at the altimeter's locations with the data measured by the main IMU. They are not used for permanent data collection and, therefore, not designed to withstand very strong an impact by waves. The Coordinate system of the extra IMUs is opposite to the main IMU's coordinate system, with the z-axis facing upwards. The yaw range is from 0° to 360° (Table 3).

The coordinate system of the extra IMU, with the z-axis facing upwards, is chosen as the universal coordinate system, shown in Figure 4. The x-axis is aligned horizontally in the direction from stern to bow, and the y-axis horizontally in the direction from starboard to port. The roll angle increases if the ship tilts from port towards starboard, while the pitch angle increases if the bow is moved downwards during the rotation. The yaw range is chosen as -180° to 180°, with zero along the x-axis. Hereby, yaw values are positive in the anti-clockwise direction and negative in the clockwise direction.

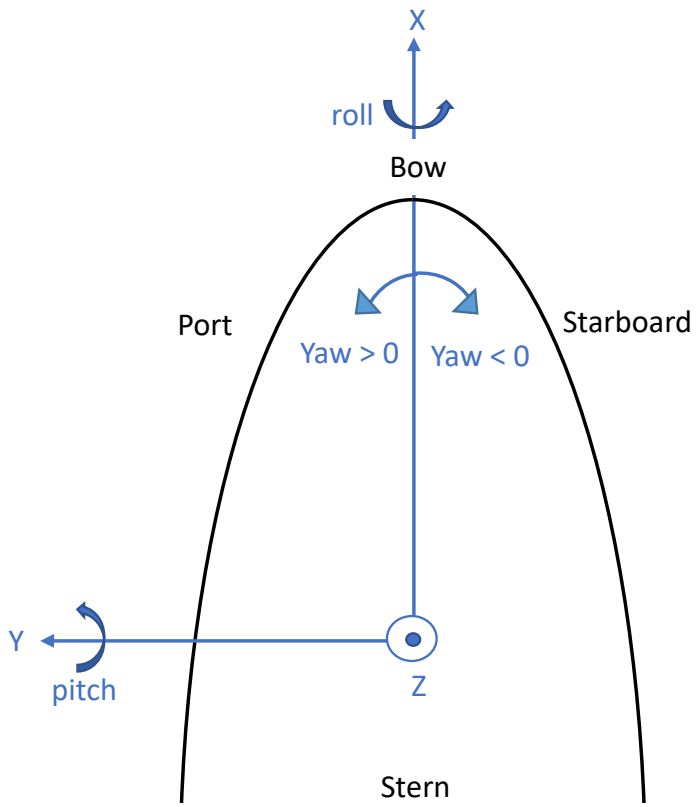


Figure 4: The bow of the ship seen from above illustrating the roll, pitch, and yaw angles in the defined universal coordinate system.

## 2.2 Data Acquisition

The wave measurements presented in this thesis were obtained during The One Ocean Expedition, a circumnavigation of the globe by the 98-meter-long tall ship Statsraad Lehmkuhl[8]. Figure 5 illustrates the sailing route, starting from Arendal the 20.08.21 and ending in Bergen the 15.04.23. The One Ocean Expedition aims to share knowledge and raise awareness about the ocean. The ship was equipped with various scientific equipment not directly employed in this to collect data on meteorology, hydrology, chemistry, biology, and plastic pollution (Huse

[7] https://www.adafruit.com/product/4569
[8] https://oneoceanexpedition.com

G. et al. in preparation). The collected data is available to everyone[9]. Two researchers were always on board Statsraad Lehmkuhl during the expedition, responsible for the data collection and instrument maintenance. I worked as a researcher for two months on the leg from Palau the 27.08.22 to Singapore the 29.10.22.

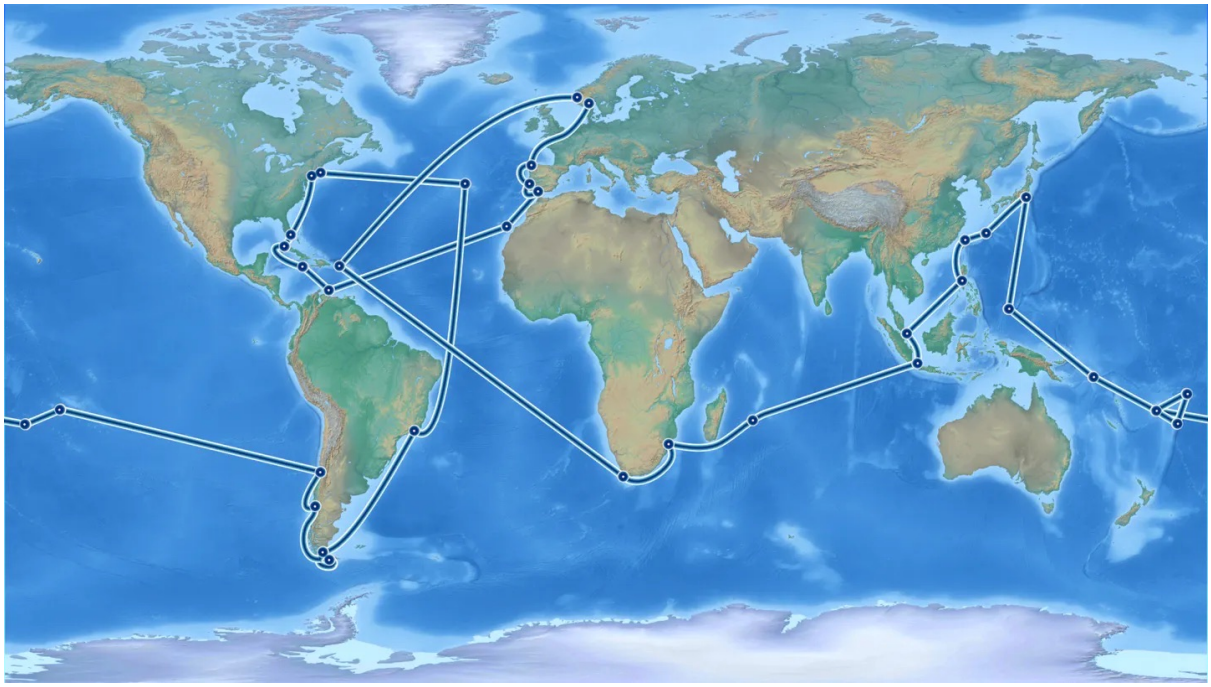

Figure 5: The sailing route of Statsraad Lehmkuhl during the One Ocean Expedition, from Arendal the 20.08.21 to Bergen the 15.04.23. Dots indicate the 36 harbors visited [8].

The main wave system was mounted on Statraad Lehmkuhl by Fabian Knoblauch the 16.06.21. He worked as a researcher from Las Palmas, Gran Canaria, 02.10.21 to Havanna, Cuba, 27.11.21 and mounted the two extra IMUs close to the radar probes the 11.10.21. The extra IMU1 was destroyed the 14.01.22 in a major winter storm in the North Atlantic Ocean [10]. The breakdown of extra IMU1 created an error in the system, which was fixed the 19.01.22 by rebooting the system by the researchers onboard.

The wave system collected data until 29.04.22, when it stopped working. The extra IMU0 was also destroyed on 29.04.22, which may be the reason for the system breakdown. During my time on board, I successfully changed the RPI, Arduino, and main IMU with spare parts stored onboard the ship. The spare parts were identical to the original system, also built by Fabian Knoblauch. I recognized that the duct tape on the Arduino board and cables were melted onto the equipment (Figure 6a), so I used strips and electrician tape to fasten the new parts (Figure 6b). The new system started logging the 15.09.22 and operated until the expedition ended the 15.04.23. The new RPI's clock was shifted 22.5 hours ahead of UTC time, which needs compensation during post-processing.

During my time onboard Statsraad Lehmkuhl, I also deployed one wave measuring drifter (Figure 7a) the 19.09.22 at 07:20 UTC, with help from Statsraad Lehmkuhl's crew. As the sea was too rough to place the drifter directly at the surface from a MOB boat, it was hoisted down in a box attached with ropes (Figure 7b). The deployment ensured that the right side of the drifter was facing up to establish communication with satellites. The drifter was named

[9] https://doi.org/10.21335/NMDC-1572929066

[10] https://www.severe-weather.eu/global-weather/polar-vortex-2022-winter-storm-izzy-snow-mk


(a) (b)

Figure 6: Picture of (a) the original processing unit operating until 29.04.22 and (b) the new processing unit operating from 15.09.22. The system components are identical, but the new unit is mounted with strips and electrical tape instead of duct tape.

Nanmadol after the Super Typhoon in the South Pacific Ocean the 19.09.22 that caused severe damage in Japan[11]. The last transmission from Nanmadol was received the 08.10.22 at 01:30 UTC, providing a 20 days time record. The researchers onboard Statsraad Lehmkuhl deployed the second drifter, Floaty, in the same manner in the Indian Ocean the 20.11.22 at 10:30 UTC. It drifted until 21.12.22 at 07:30 UTC producing a 31 days time record.

(a) (b)

Figure 7: Picture of (a) the drifter and (b) the deployment method in a box attached with ropes.

[11] https://www.bbc.com/news/world-asia-62952942

An overview of the data studied in this thesis, from 04.10.21 to 20.12.22, is shown in Figure 8. The ship track of the original wave system is marked in black, while the new system is marked in grey. Knoblauch, 2022 studied the wave properties during the crossing of the Atlantic, marked red and named leg 2 (Figure 8). Table 4 list the time periods when the ship was stationed in harbor or anchored during the expedition route that I have studied. These wave data are discarded because the wave measurements may be influenced by the harbor constructions and ship traffic.

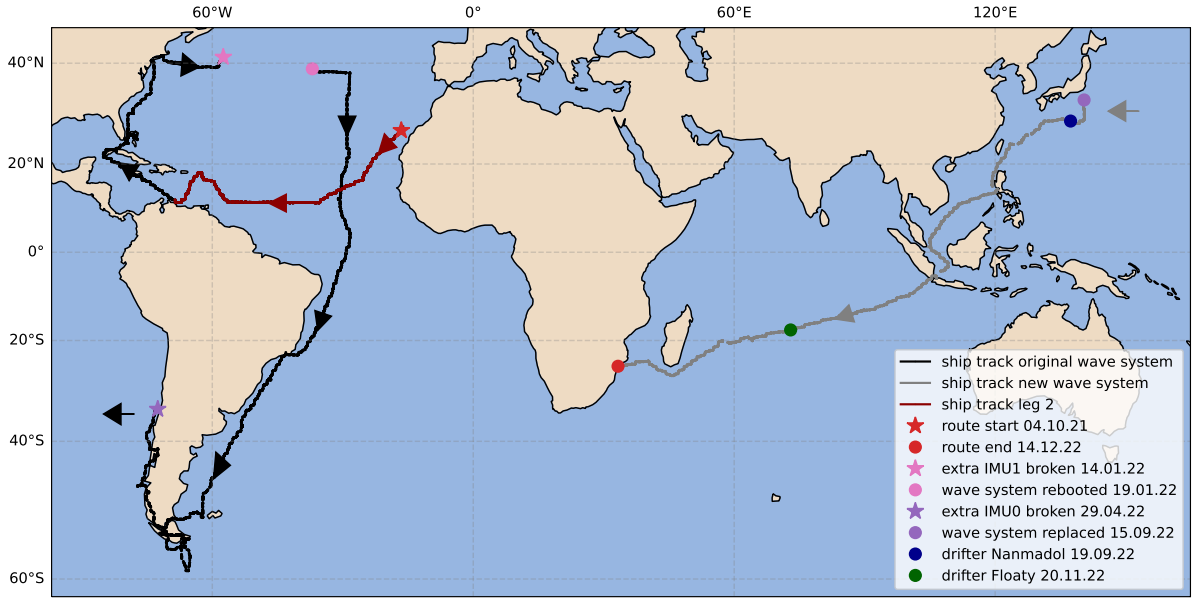


Figure 8: An overview of the ship track, wave sensor challenges, and the drifters studied in this thesis.

Table 4: Time periods at harbor or anchor at the wave sensors UTC time. From 15.09.22, the RPI UTC time is 22.5 hours ahead of UTC time.

| Port, Country | Time Period |
|---|---|
| Las Palmas, Gran Canaria | 30.09.21 10:00 - 04.10.21 17:00 |
| Willhelmstad, Curacao | 04.11.21 12:00 - 08.11.21 22:00 |
| Port Royal, Jamaica | 13.11.21 16:00 - 18.11.21 00:00 |
| Havanna, Cuba | 24.11.21 13:00 - 28.11.21 21:00 |
| Nassau, Bahamas | 02.12.21 13:00 - 06.12.21 05:00 |
| Miami, USA | 07.12.21 17:00 - 10.12.21 21:00 |
| New York, USA | 01.01.22 00:00 - 04.01.22 19:00 |
| Newport, USA | 06.01.22 13:00 - 10.01.22 01:30 |
| Horta, Azores | 22.01.22 09:00 - 25.01.22 16:30 |
| Rio de Janeiro, Brazil | 20.02.22 16:00 - 26.02.22 19:30 |
| Punta Arenas, Chile | 22.03.22 21:00 - 26.03.22 22:00 |
| Ushuaia, Argentina | 29.03.22 15:30 - 01.04.22 13:00 |
| Ushuaia, Argentina | 06.04.22 11:00 - 08.04.22 14:00 |
| Puerto Williams, Chile | 11.04.22 11:00 - 12.04.22 21:00 |
| Puerto Montt, Chile | 22.04.22 12:00 - 25.04.22 02:00 |
| Okinawa, Japan | 23.09.22 09:30 - 27.09.22 15:30 |
| Ishigaki, Japan | 30.09.22 09:30 - 06.10.22 15:30 |
| Manila, Philippines | 11.10.22 03:30 - 14.10.22 18:30 |
| Singapore | 26.10.22 09:30 - 27.10.22 09:00 |
| Jakarta, Indonesia | 04.11.22 23:30 - 08.11.22 17:30 |
| Mauritsius | 29.11.22 11:30 - 04.12.22 16:00 |
| Maputo, Mozambique | 14.12.22 19:30 - 03.01.23 12:00 |

## 2.3 Additional Data

Some additional data are required for post-processing, available from the ship's data log, with minute resolution[9]. The wave sensor does not log coordinates. Therefore latitude and longi-

tude values are needed to reconstruct the sailing route. Ship speed and heading are utilized to correct for the Doppler effect. Wind data is utilized to study the influence on the wave measurements. A wind sensor WSS 550[12] operating with ultrasound is mounted in the Mizzen mast 45 meters above the ocean surface.

During post-processing, the additional data is averaged over 30 minutes to correspond to the resolution of the wave parameters, with a cyclic average for directions. Wind direction and heading are defined in the oceanographic convention, the direction the wind/ship is going towards, relative to the North as zero.

### 2.3.1 Visual Observations

Visual observations of wind speed and sea state are used to quality check the measurements for some extreme events. The officer on watch on Statsraad Lehmkuhl noted visual observations every two hours during the entire expedition. The wind speed is observed according to the Beaufort scale, as a number from 0 as calm, to 12 as hurricane force, with a wind speed over 33m/s. The sea state observations follow the Douglas Sea scale, from 0 as a glassy surface to 9 as a phenomenal sea with wave heights larger than 14m (Haddon, 2015).

### 2.3.2 The Wave Measuring Drifters

Wave measurements from surface drifters are compared to the ship mounted measurements. The OpenMetBuoy-v2021a is an open-source instrument for oceanographic measurements of drift and waves[13]. It monitors drift with a Global Navigation Satellite System (GNSS) module and wave activity with an IMU sensor (Rabault, Nose, et al., 2022). Since the instruments were transported by plane, the lithium batteries were exchanged with three traditional alkaline D-cell batteries. Alkaline batteries are heavier than lithium batters. Thus, a larger rigid plastic enclosure was utilized to compensate for the loss of buoyancy. The resulting size of the drifter was 12cm x 12cm x 10cm (Figure 7a), and its weight was approximately 1kg.

The drifter operates in activity and sleep phases to preserve battery capacity. The position is collected for 2min each 30min, and the wave spectrum is sampled for 20min every 3 hours. The raw wave data are sampled at approximately 800Hz and time-averaged into a 100Hz low-noise sensor value, rejecting individual measurements that deviate more than three standard deviations from the rest. A Kalman filter implementation computes the vertical wave acceleration, which is further time-averaged to 10Hz. The one-dimensional wave spectrum is obtained by fast Fourier transformation with the Welch method for frequencies between 0.05Hz and 0.5Hz, which retains only the relevant frequencies for ocean waves (Rabault, Nose, et al., 2022). The wave data and geographical positioning are packed, buffered, and transmitted via Iridium Satellite Communication using efficient binary encoding.

### 2.3.3 Wave Model Data

The wave measurements are compared to the high-resolution ECMWF Ocean Wave Model (ECWAM). ECWAM has two-way interactions with the atmospheric forecast model IFS and the dynamic ocean model NEMO and its sub-program LIM2 concerning sea-ice (ECMWF, 2021a). Currently, only sea-ice cover interacts with the high-resolution ECWAM, not ocean surface currents (Bidlot J., personal communication, January 2023). The high-resolution ECWAM has a global coverage on 0.125 °x 0.125 °latitude-longitude grid corresponding to 14km grid spacing (ECMWF, 2022). The operational ECWAM assimilates satellite altimeter wave height data from

[12] https://deif-cdn-umbraco.azureedge.net/media/dazjrilw/wss-500-series-data-sheet-4921250078-uk.pdf?rnd=133298405088900000v=8

[13] https://github.com/jerabaul29/OpenMetBuoy-v2021a

Jason-3 and SARAL/AltiKa. Satellite altimeter wind speed is not assimilated in IFS (Abdalla S., personal communication, January 2023).

ECWAM is a third-generation spectral wave model that forecasts the two-dimensional surface spectrum from wave advection, wave refraction, wind-wave generation, non-linear wave interactions, and wave dissipation due to white capping and bottom friction (ECMWF, 2021b). The wave energy spectrum is discretized into 36 frequencies and 36 directions. The model provides a 10-day forecast, twice daily at 00 UTC and 12 UTC. The lead time of the forecast describes the time interval from the initialization of the forecast to the time at which the forecast is valid. In this thesis I will use the best estimate, which is a time series composed of the shortest lead times available. As the model is initialized every 12 hours, the maximum lead time is 11h.

The wave model data are accessed from the Meteorological Archival and Retrieval System (MARS) in GRIB format, where each parameter is assigned a unique Parameter ID[14]. ECWAM's wave parameters are defined for total sea, wind sea, total swell, and three swell partitions by integrating over the respective components of the wave spectrum (ECMWF, 2021b). Wind sea is defined as the wave components that are still influenced by wind forcing, whereas the remaining part of the spectrum is termed swell.

The wave parameters utilized in this thesis are listed in Table 5, with the parameters mainly studied marked in bold. The partition of wind waves and swell is only considered in a study of an extreme event. Wind and wave direction from ECWAM is defined as the direction the wind/waves are coming from, relative to the North as zero. In this thesis, the directions are inverted to follow the oceanographic convention, defined as the direction the wind/waves are going.

Table 5: Wave parameter ID in GRIB format from the wave model ECWAM [14]. The parameters mainly studied is marked in bold.

| Variable Name | Parameter ID |
|---|---|
| **Significant height of combined wind waves and swell** | **140229** |
| Significant height of wind waves | 140234 |
| Significant height of swell waves | 140237 |
| **Peak wave period** | **140231** |
| Wind sea peak period | 500187 |
| Swell peak period | 500189 |
| **Mean wave direction** | **140230** |
| Direction of wind waves | 500072 |
| Direction of swell | 500075 |
| 10-meter wind speed and wind direction | 207 |

### 2.3.4 Satellite Altimetry Data

In addition to model data, satellite altimeters are used to verify the wave measurements. The missions: Sentinel-3A and 3B, Sentinel-6A, CryoSat-2, HaiYang-2B, and CFOSAT are not used for assimilation in ECWAM and can therefore serve as an independent check on the data quality. Altimeter significant wave height and wind speed Level-3 data are accessed from Copernicus Marine Environment Monitoring Service[15]. Data is provided globally with a 3-hour time window and spatial resolution of 7km x 7km. The level-3 data are quality controlled, monitored, inter-calibrated, and filtered for noise (Taburet et al., 2022).

Wave height and wind speed are retrieved as the altimeter transmits a spherical radar signal in the nadir direction, which is reflected at the sea surface and returned to the satellite (Robinson,

[14] https://codes.ecmwf.int/grib/param-db/?filter=grib2

[15] https://data.marine.copernicus.eu/product/WAVE_GLO_PHY_SWH_L3_NRT_014_001/description

2004). If the sea surface is calm, the amplitude of the reflected signal increases immediately as the leading edge of the signal reaches the surface. For a rough sea surface, the amplitude of the reflected signal increases gradually, shown in Figure 9a. The temporal variation of the received signal is called the waveform, illustrated in Figure 9b. Significant wave height is determined from the leading edge slope of the waveform; the steeper slope, the smaller waves. The amplitude of the received signal (P) gives the backscatter coefficient (Passaro et al., 2014). Wind speed is then retrieved from an empirical relation dependent on the backscatter coefficient (Abdalla, 2014), usually evaluated for 10 meters above the sea surface.

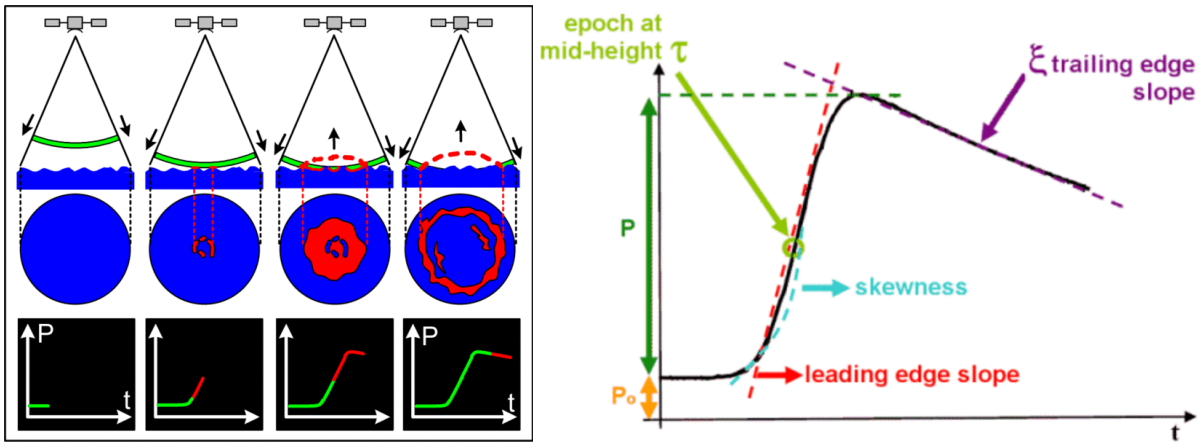


(a) (b)

Figure 9: The altimeter signal reflected at a rough sea surface (a) and the typical waveform of the signal received by the satellite altimeter (b) (Aviso, 2022).

The relevant satellite altimeter missions are in a low-earth or sun-synchronous orbit with 720 - 1336km altitude, listed in Table 6. Due to the low altitude, the satellite missions have good global coverage, illustrated in Figure 10. Within 24 hours, each satellite orbit the Earth's surface typically 10-15 times. Revisit time is the duration between observations at the same point on Earth's surface (Robinson, 2004). Common to all missions except CryoSat-2 is a short revisit time of 10 to 27 days. Combined, the satellite altimeter missions cover large areas of the Earth's surface, providing data for comparison with the ship and drifter tracks.

Hereby, the satellite altimeter is referred to as satellite to avoid confusion with the altimeter probes.

Table 6: Orbit parameters of the satellite altimeter missions utilized in this thesis (Jiang et al., 2017; Donlon et al., 2021; CNES and CNSA, 2012).

| Satellite Name | Launch | Orbit | Altitude [km] | Inclination [°] | Revisit time [days] |
|---|---|---|---|---|---|
| CryoSat-2 (c2) | April 2010 | Low-earth | 720 | 92 | 369 |
| Sentinel-3A (s3a) | February 2016 | Sun-synchronous | 814 | 99 | 27 |
| Sentinel-3B (s3b) | April 2018 | Sun-synchronous | 814 | 99 | 27 |
| HaiYang-2B (h2b) | October 2018 | Sun-synchronous | 973 | 99 | 14 |
| CFOSAT (CFO) | October 2018 | Sun-synchronous | 519 | 97 | 13 |
| Sentinel-6A (s6a) | November 2020 | Low-earth | 1336 | 66 | 10 |

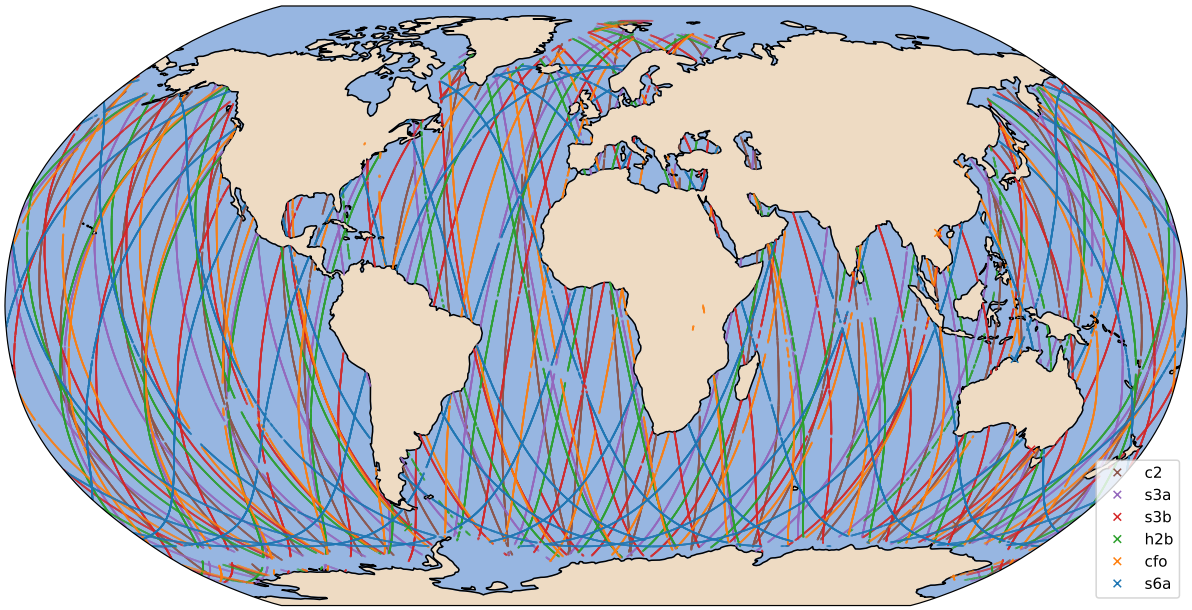


Figure 10: Tracks of the relevant satellite altimeter missions within 24 hours the 14.01.22

# 3 Methods

## 3.1 Post-Processing

The post-processing procedure is developed by Knoblauch, 2022. The software has undergone substantial updates and the latest version is accessible online [16].

### 3.1.1 Time Synchronisation

Although all parts of the system described in Section 2.1 operate at a frequency of 10Hz, the different system components are not synchronized. To obtain the surface elevation, probes and IMU data are needed at the same time instance. To synchronize the instruments, a common time base is defined as 30 minutes with a time step of 0.1s (10Hz). The 30-minute data set of each system component is linearly interpolated over the common time base. The synchronization does not change the frequency resolution of 10Hz and should not impact the results since the maximal difference between measurement and common time base is 0.05s.

### 3.1.2 Determining the Vertical Position of the IMUs

The vertical position of the IMU is required to compensate for the motion of the ship. The vertical acceleration fluctuation is found by subtracting the mean value of each 30-minute file:

$$\ddot{z}(t)' = \ddot{z}(t) - \overline{\ddot{z}(t)} \tag{1}$$

The vertical position is obtained by time integrating the vertical acceleration twice. Assuming that the vertical acceleration resembles an oscillating signal, we can simplify the integration with Fourier transformation. In Fourier space, the double integration is realized by multiplication with a constant $\frac{-1}{\omega^2}$, where $\omega$ is the angular frequency $\omega = 2\pi f$ (Holthuijsen, 2007b). The vertical fluctuation is thereby given by:

[16] https://github.com/joe045/wave_sensors_one_ocean_expedition_2023

$$z(t)' = \mathcal{F}^{-1}\left[\frac{-1}{\omega^2}\mathcal{F}[\ddot{z}(t)'](\omega)\right](t) \tag{2}$$

The transformation into Fourier space and back is performed for each 30-minute file by fast Fourier transformation. Frequencies outside the range $f_{min}$=0.05Hz and $f_{max}$=0.5Hz are removed, similarly to the wave measuring drifters. The Fourier transformation might cause errors at the beginning and end of the file. Therefore the first and last 3 minutes of each data file are excluded after the transformation.

### 3.1.3 Calculation of the Water Surface Fluctuation

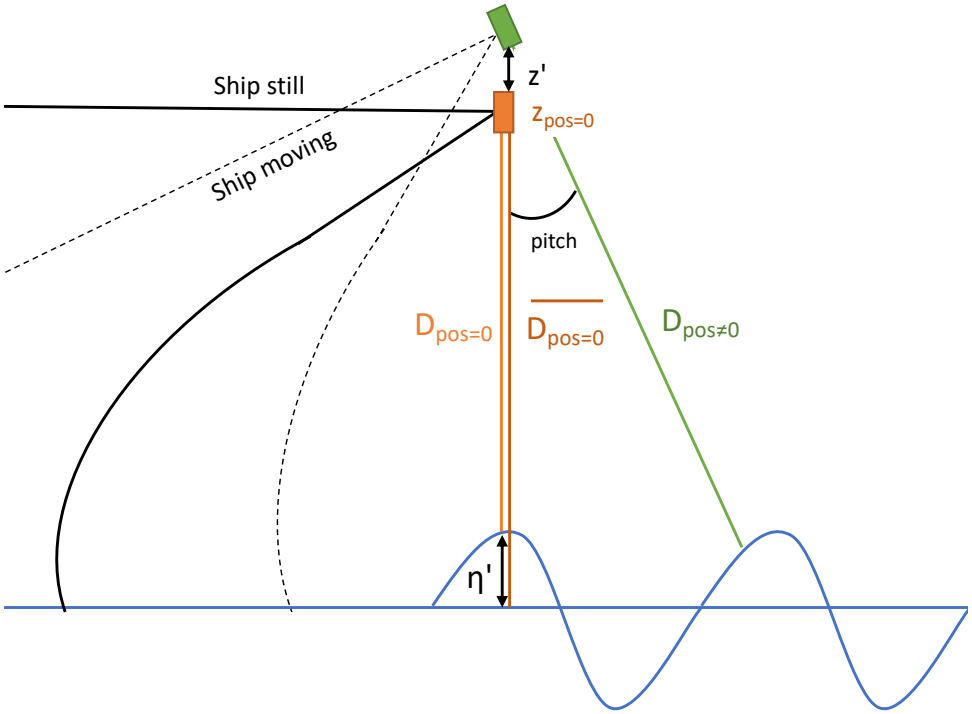


Figure 11: Illustration seen from starboard (as in Figure 1) of the calculation of the water surface fluctuation $\eta'$, for a ship lying still in the water (orange), and a ship moving with the waves (green).

The water surface fluctuation is determined similarly as Christensen et al., 2013. Figure 11 illustrates that if the ship lay entirely still and horizontal in the water, the surface fluctuation measured by the altimeter probe $\eta'_{\text{probe}}$ would be the difference between the measured distance $D_{\text{pos=0}}$ and the mean distance of each data file of 30 minutes $\overline{D_{\text{pos=0}}}$. With the sign convention in Equation 3, a positive fluctuation resembles a crest, and a negative fluctuation resembles a trough.

$$\eta'_{\text{probe}} = \overline{D_{\text{pos=0,probe}}} - D_{\text{pos=0,probe}} \tag{3}$$

The altimeter probe position and angle vary due to the ship's motion under the influence of waves. To find the water surface fluctuation, we must compensate for the ship's movement. Figure 11 shows that the distance measured by the probe $D_{\text{pos}\neq 0}$ is the hypothenuse of an orthogonal triangle. The steady-state distance $D_{\text{pos=0}}$ plus the fluctuating vertical position of the probe z' (Equation 2) is the adjacent cathetus to the pitch angle in the x-z-plane, and to the roll angle in the y-z-plane. The trigonometric relations of the orthogonal triangle give:

$$D_{\text{pos=0,probe+IMU}} = D_{\text{pos}\neq 0}\cos(\text{pitch})\cos(\text{roll}) - \text{z}' \tag{4}$$

Only the fluctuating surface elevation is of interest:

$$\eta'_{\text{probe+IMU}} = \overline{D_{\text{pos=0,probe+IMU}}} - D_{\text{pos=0,probe+IMU}} \tag{5}$$

This formulation is analogous to Equation (1) by Christensen et al., 2013, with the opposite sign convention. Løken et al., 2021 added terms considering the roll and pitch elevation effects due to the horizontal and vertical distance between the probe and the IMU, which is not considered here.

If the altimeter probe is ignored ($D = 0$), the surface fluctuation is determined solely from the vertical fluctuation $\eta'_{\text{IMU}}$, similarly to the wave measuring drifters:

$$\eta'_{\text{IMU}} = \text{z}' \tag{6}$$

### 3.1.4 Correcting for the Doppler Effect

Data recorded while the ship is sailing will contain a Doppler shifted frequency because the waves are moving relative to the ship. Correcting the Doppler shift requires knowing the wave direction and the ship's heading and speed. Since the wave direction was not measured by any system onboard the ship, it is obtained from the ECWAM model data. The observer's velocity $\text{v}_o$, in the direction of the waves, is the ship's velocity $\text{v}_{\text{ship}}$ scaled by the angle $\theta$ between the wave direction and the ship heading:

$$\text{v}_o = \text{v}_{\text{ship}} \cdot \cos(\theta) \tag{7}$$

$$\theta = \text{wave direction} - \text{heading} \tag{8}$$

The observer's velocity $\text{v}_o$ is positive when the ship is sailing with waves (orange-colored area Figure 12) and negative when the ship is sailing into waves (white area Figure 12). The observer's velocity is zero when wave direction and ship heading are perpendicular, resulting in no Doppler Shift. The Doppler shift is most significant when the waves and ship heading are in the same direction, either away or towards each other, and decreases for larger $\theta$ angles between them.

The Doppler correction presented by Knoblauch, 2022 is based on the same equations as previous work (Clarence O Collins, Blomquist, et al., 2016; Cifuentes-Lorenzen et al., 2013; Amador, Merrifield, and Terrill, 2022). The relation between the frequency registered by an observer $f_o$ and the frequency emitted by the sender $f_s$ is given as:

$$f_o = f_s\left(\frac{c \pm \text{v}_o}{c \pm \text{v}_s}\right) \tag{9}$$

The observer's velocity $\text{v}_o$ should be negative when the observer moves away from the source and positive when the observer moves towards the source. Therefore the sign of $\text{v}_o$ is negative in Equation 9 to inverse the sign of $\text{v}_o$ in Figure 12. The velocity of the sender, $\text{v}_s$ is zero, as the waves traveling over the sea are not caused by a distinct sender.

The frequency of the incoming waves $f_s$ is the parameter that will be derived from the measured frequency $f_o$. The signal propagating velocity $c$ is the phase speed of surface gravity

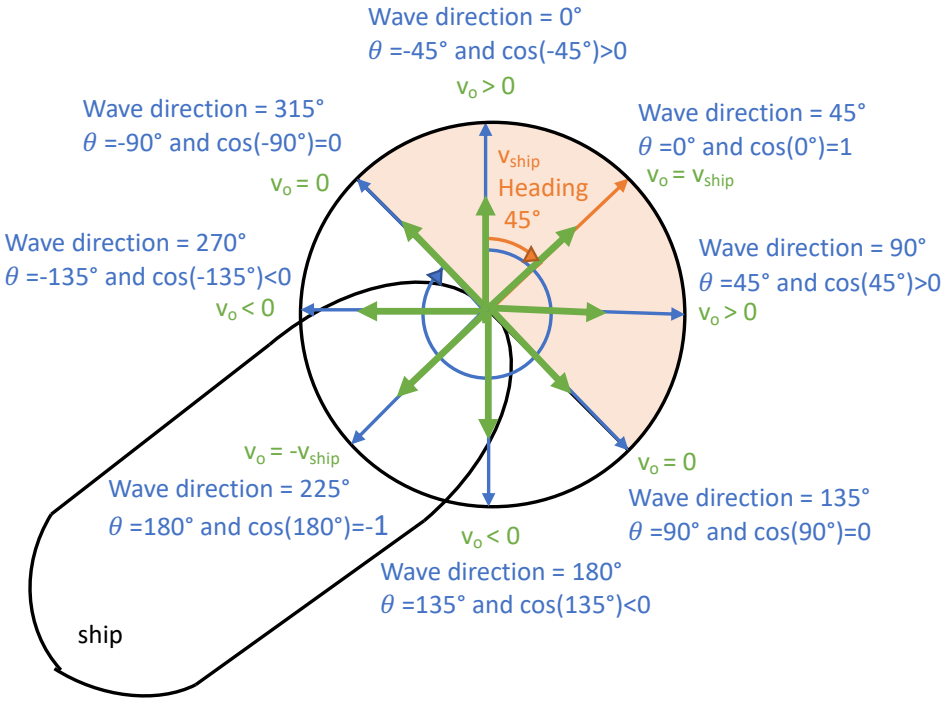


Figure 12: The relation between ship heading (orange), wave direction and $\theta$ (blue), as seen from above. The sign of $v_o$ is positive in the orange-colored area and negative in the white area.

waves. In deep water, the phase speed is the ratio between the gravitational constant $g$ and the angular frequency $\omega = 2\pi f$ (Holthuijsen, 2007d):

$$c = \frac{g}{\omega_s} = \frac{g}{2\pi f_s} \tag{10}$$

Inserting Equation 10 to Equation 9 gives the second order equation for $f_s$:

$$f_s^2 - \frac{g}{2\pi v_o} f_s + \frac{g}{2\pi v_o} f_o = 0 \tag{11}$$

Two solutions for the frequency $f_s$ can be gained from Equation 11:

$$f_{s+,s-} = \frac{g}{4\pi v_o} \pm \sqrt{\frac{g}{2\pi v_o}\left(\frac{g}{8\pi v_o} - f_o\right)} \tag{12}$$

Initially, the Doppler shifted peak period (Equation 16) was calculated from the minimum value of the two Doppler shifted frequencies in Equation 12. This method gives some unrealistic negative peak periods, seen in Figure 4.22 of Knoblauch, 2022. The negative frequency solution usually fits best with the original peak period, but the positive frequency fits better when the ship speed is close to zero. Therefore, I have calculated the peak period from both the negative and positive Doppler shifted frequencies and then chosen the maximum value of the two Doppler shifted peak periods. It should also be noted that I have used data measured at the ship as velocity and heading, while Knoblauch, 2022 estimated the ship's speed and heading from the ship's position.

### 3.2 Wave Spectrum and Wave Properties

The sea surface fluctuation obtained in Section 3.1.3 is not a wave. Figure 13 shows the most common definition of a wave, the surface elevation profile between two successive downward zero-crossings (Holthuijsen, 2007b). The alternative definition of a wave is the profile between two successive upward zero-crossings. Wave height is the vertical distance between a wave's lowest and highest surface elevation, while the wave period is the time interval between the two zero-crossings. The maximum wave height is the largest wave height in the time record.

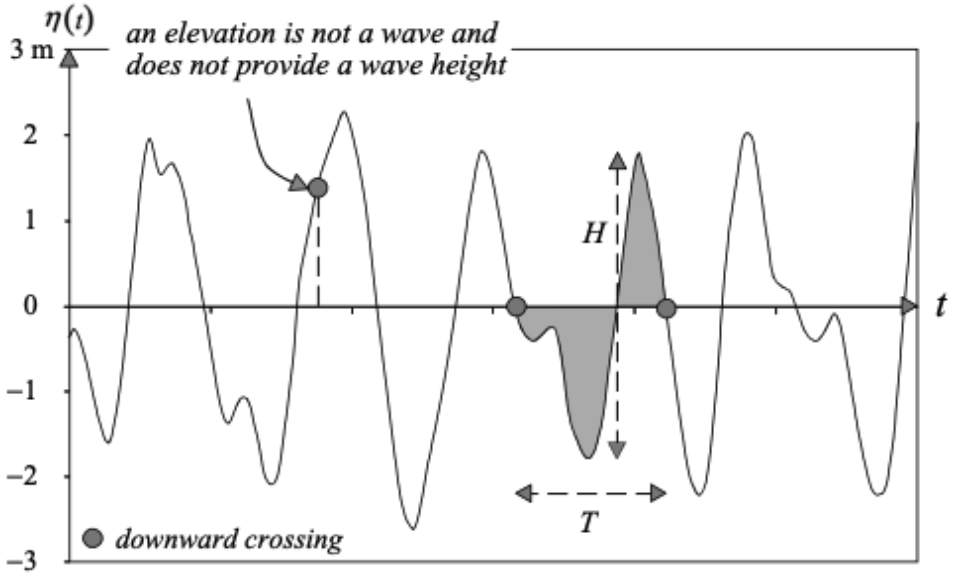


Figure 13: Definition of a wave (dark grey), wave height (H) and wave period (T) (Holthuijsen, 2007b).

Each single wave height and period are not studied individually but rather averaged over a wave record. The ship mounted measurement system has a record length of 30 minutes. This length is chosen because it is short enough to assume the sea state to be statistically stationary, meaning that all statistical characteristics of the waves are assumed to be independent of time (Ochi, 1998a). It is also long enough to reliably characterize the waves with averaging.

In this thesis, waves are described in the form of the wave spectrum and integrated wave parameters. The wave spectrum describes the sea surface as a stochastic process: an ordered set of random variables. Any random variable is fully characterized by its probability density function (Holthuijsen, 2007b). The random-phase/amplitude model assumes the surface elevation to be a sum of a large number of statistically independent, harmonic waves. Each wave have a constant but randomly chosen amplitude (Rayleigh distributed) and a random phase (uniformly distributed). The Central Limit theorem states that the sum of a large number of independent random variables is Gaussian distributed. If the sea state is statistically stationary and the surface elevations are Gaussian distributed, the variance density spectrum provides a complete statistical description of the waves. Only the one-dimensional wave spectrum is considered since the ship mounted system cannot measure directional properties. Although the wave spectrum is based on assumptions, measurements have shown this description to be very representative. Deviations from the Gaussian model typically occur for steep waves and shallow water (Holthuijsen, 2007b).

The one-dimensional variance density spectrum E(f) is obtained by fast Fourier transformation with the Welch method (Welch, 1967). The surface fluctuations for each 30-minute data file are split into segments of 180s which correspond to 1800 data points at the sampling rate of 10Hz. Overlap between segments is set to 90%. A Hann window is applied to each segment to reduce

spectral leakage. Frequencies outside the range $f_{min} = 0.05$Hz and $f_{max} = 0.5$Hz are cut off, similarly to the wave measuring drifters. Integral wave parameters are expressed in terms of the moment of the variance density spectrum (Holthuijsen, 2007c). The spectral moments are computed by integrating the variance density spectrum from the minimum to the maximum frequency equal to the cutoff frequencies:

$$m_n = \int_{f_{min}}^{f_{max}} f^n E(f) df \qquad for \quad n = ..., -2, -1, 0, 1, 2 \tag{13}$$

The integrated significant wave height is estimated from the the zeroth-order moment $m_0$ (Holthuijsen, 2007c; Ochi, 1998b):

$$H_s = 4\sqrt{m_0} \tag{14}$$

Significant wave height is defined as the mean value of the highest one-third of the waves. This statistical measure of wave height is often used because it correlates well with the wave height estimated visually by experienced observers (Holthuijsen, 2007b). Figure 14a illustrates the significant wave height in the Rayleigh distribution, where the white space represents the highest one-third of the waves.

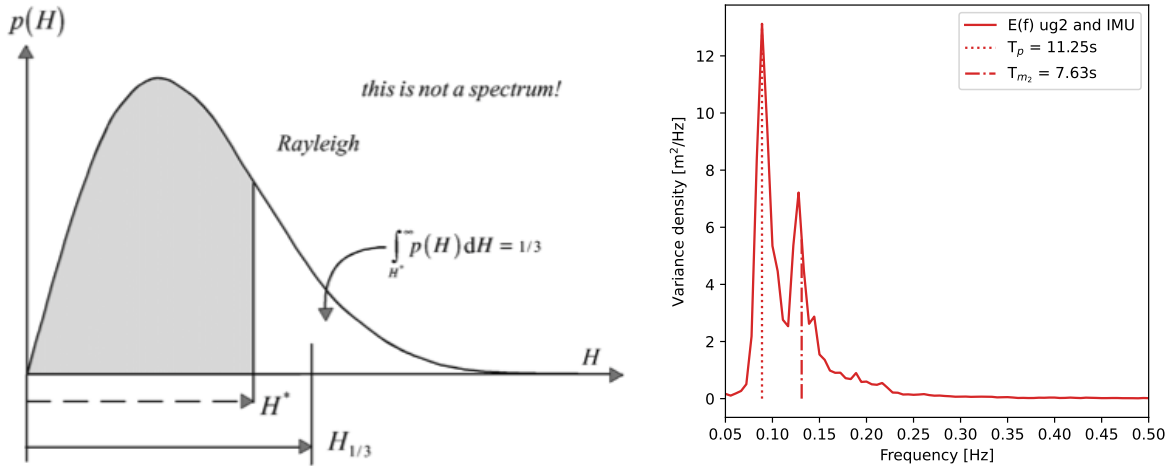


(a) (b)

Figure 14: The (a) significant wave height ($H_{1/3}$) in the Rayleigh distribution (Holthuijsen, 2007c) and (b) variance density spectrum over 30-minutes the 22.10.21 00:00, with the corresponding peak (Tp) and mean ($T_{m_2}$) periods.

The mean zero-crossing period is also defined from the moments of the variance density spectrum (Holthuijsen, 2007c; Ochi, 1998a):

$$T_{m_2} = \sqrt{\frac{m_0}{m_2}} \tag{15}$$

The peak period is defined as the reciprocal of the peak frequency (Bidlot, 2016).

$$T_p = \frac{1}{f(max(E(f)))} \tag{16}$$

In this thesis, the peak period is studied instead of the mean period because it represents the period of the dominant sea state, either wind sea or swell. Since the ship is sailing in areas

where we expect both wind sea, and swell, the mean period might represent a period between these, not corresponding to any realistic wave system. Figure 14b illustrates a variance density spectrum E(f) over 30 minutes from a relatively calm day 22.10.21 in the Atlantic Ocean. The narrowest peak at low frequency corresponds to swell because the swell is rather regular and long-crested (Holthuijsen, 2007b). Wind sea is irregular and short-crested, corresponding to the broader peak at a higher frequency. The peak period of 11.25s represents the swell, while the mean period of 7.63s represents a period slightly lower than the peak period of the wind sea. For the same reason, the peak wave direction would be preferable over the mean wave direction but it is not available in ECWAM (Bidlot J., personal communication, January 2023).

### 3.3 Collocation with Model and Satellite Products using Wavy

The software package Wavy is used to gather satellite and model data and collocate the products with the ship track. It is an open-source code[17] developed by Patrik Bohlinger, researcher at the Meteorological Institute of Norway. The collocation process is constrained by a time window and a distance limit, illustrated in Figure 15. Model and satellite crossings are extracted if they were recorded within the time window (green rectangle). For model data, only the nearest grid cell within the distance limit (red circle) is allowed. This results in two time series, one for the ship measurements and one for the wave model consisting of the same number of values (Bohlinger, Breivik, et al., 2019). For satellite crossings, all values within the distance limit are allowed. For the statistics, the satellite value with the closest distance to the ship is chosen for comparison. I have described an example of collocation with the ship track in the Wavy documentation [18].

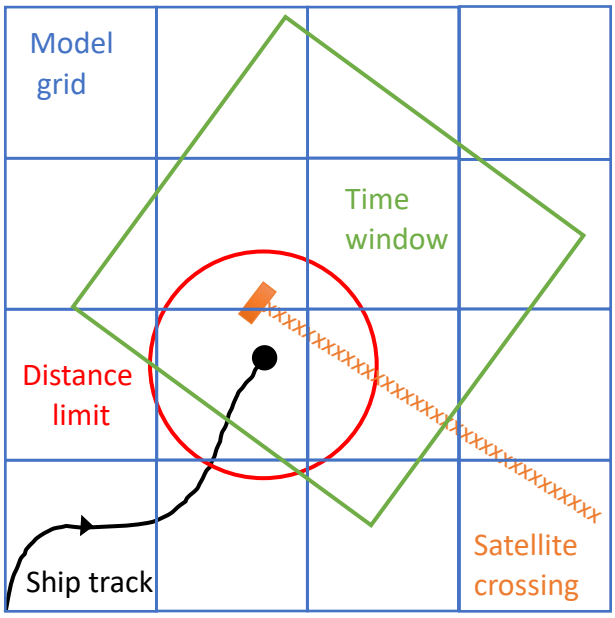


Figure 15: Illustration of the collocation method in Wavy.

The collocation constraints for the ship mounted wave system and the wave measuring drifters are summarized in Table 7. The time window should be less than half the observations' resolution to ensure that no model or satellite values are duplicated. Figure 16a illustrates the satellite crossings obtained along the sailing route, with 581 values from 56 satellite crossings.

[17] https://github.com/bohlinger/wavy
[18] https://wavyopen.readthedocs.io/en/latest/vietnam22.html

For the drifters Nanmadol and Floaty, 16 and 8 crossings were found, respectively (Figure 16b and 16c).

Table 7: Time window and distance limit for the collocation process with Wavy.

| Observation | Time resolution [min] | Time window [min] | | Distance limit [km] | |
|---|---|---|---|---|---|
| | | Satellite | Model | Satellite | Model |
| Ship mounted wave system | 30 | 15 | 15 | 50 | 50 |
| Wave measuring drifters | 180 | 90 | 15 | 90 | 50 |

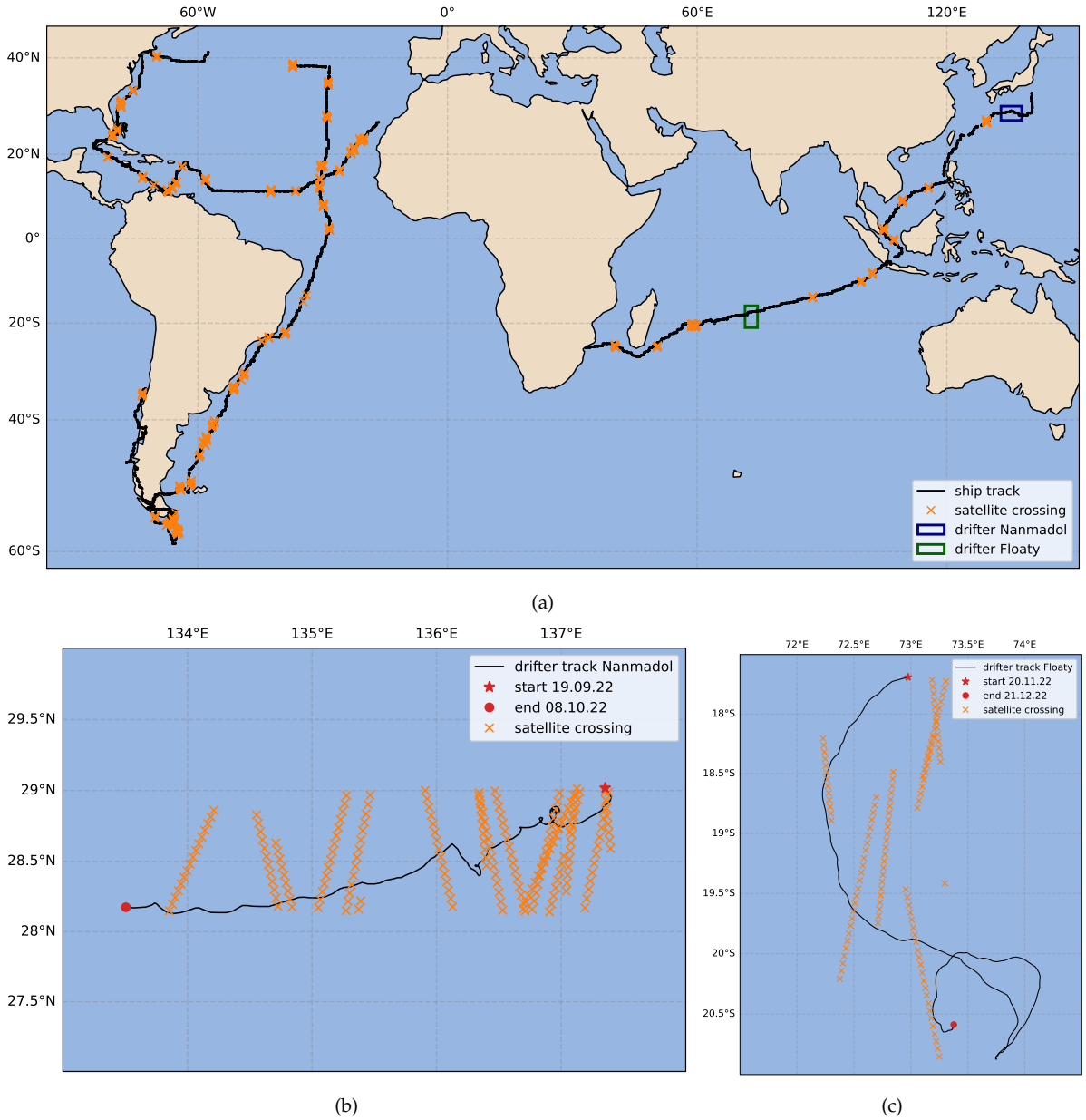


Figure 16: An overview of the collocated satellite crossings along the ship track (a) and the drifter tracks of Nanmadol (b) and Floaty (c).

### 3.4 Validation Statistics

The variance of the measurements is described by the average standard deviation. It is the square root of the sum of variances over all 30-minute files. The standard deviation has the same unit as the data input (Wilks, 2011a).

$$\overline{s} = \sqrt{\frac{s_1^2 + s_2^2 + .... + s_i^2}{i}} \tag{17}$$

The variance within each 30-minute file is calculated as follows:

$$s^2 = \frac{1}{n-1}\sum_{i=1}^{n}(x_i - \overline{x})^2 \tag{18}$$

Several validation statistics are used to compare the wave observations to model and satellite data. The variables are reversed compared to World Meteorological Organization, 2021. The wave model and satellite data are treated as the "ground truth" instead of the observations since the purpose is to quantify the measurement system.

- $x_o$ is the observed values of the chosen parameter
- $x_v$ is the value to evaluate against as the "ground truth" (satellite and model)
- $N$ is the number of collocated values to be used for verification

Bias or mean deviation (MD) is the difference between the average observations and ground truth. Positive MD indicates that the observation is too large on average, while negative MD means that the observation is too small on average. It has the same units as the input data. MD is also known as a systematic error but gives no information about the typical magnitude of the observation error (Warner, 2014).

$$\text{Bias} = \text{MD} = \frac{1}{N}\sum_{i=1}^{N}(x_o - x_v)_i \tag{19}$$

Root mean squared deviation (RMSD) is the square root of the average squared difference between the observation and ground truth. Squaring the difference produces positive terms, increasing from zero as discrepancies between the pairs increase. The squaring will also weigh large deviations more than minor deviations. RMSD has the same physical dimension as the input data. It is a measure of accuracy and can be interpreted as a typical magnitude for the error (Warner, 2014).

$$\text{RMSD} = \sqrt{\frac{1}{N}\sum_{i=1}^{N}(x_o - x_v)_i^2} \tag{20}$$

The correlation coefficient is a dimensionless, single-value measure of the association between observation and the ground truth. The Pearson product-moment correlation coefficient is used, following the convention from Wilks, 2011c. It is defined as the ratio of the covariance between observation and ground truth to the product of the standard deviations of each. If the correlation coefficient is zero, there is no correlation between the variables. A correlation coefficient of 1 implies perfect positive correlation, while -1 implies perfect negative correlation (Wilks, 2011c).

$$R_{o,v} = \frac{cov(x_o, x_v)}{std(x_o) \cdot std(x_v)} \tag{21}$$

The linear regression line describes the linear relationship between observation and ground truth. The observation is treated as the predictor variable (x), while the ground truth is the predictand (y). Equation 22 is found by calculating the interception (a) and the slope (b) that minimize the vertical deviations of the data points from the line (Wilks, 2011b).

$$y = a + bx \tag{22}$$

Quantile-quantile lines illustrate the relation between observations and ground truth at different levels, which the linear regression line does not represent. A quantile divides the data into equal-sized intervals based on the order of the values within the data set. In other words, it divides the probability distribution into segments that contain an equal proportion of the data. Here, percentiles are used, which divide the data set into 100 equal parts. For example, the median, 50th percentile, have equal proportions of the data above and below it (Wilks, 2011b).

# 4 Results

## 4.1 The Surface Elevation

At first, the surface elevation is studied to quality check the raw data which the wave properties are calculated from. Figure 17a - 17c show 60 seconds of the measured distance and surface fluctuation (Equation 3, 4 and 6) from a relatively calm day in the Atlantic Ocean, 22.10.21. Comparing the three altimeter probes, ug1, ug2, and the radar, reveals that the radar originally had an opposite fluctuation. The radar is, therefore, inverted to match the fluctuation of the ultrasonic probes. Fig 17c illustrates that this error was amplified when the IMU position was subtracted when it should be reducing the amplitude. Inverting the sign, the radar fluctuation resembles ug2, as it should, since they are mounted at the same location.

The surface elevation is also studied for the new processing unit mounted 15.09.22. Figure 18 shows the same properties as Figure 17 for another relatively calm day in the Indian Ocean, 15.11.22. All three altimeter probes have unrealistic low and rapid oscillation, compared to Figure 17. Over 30 minutes, the mean amplitude of ug2's surface fluctuation of the new system is 0.01m, which is 69 times smaller than the original system's mean amplitude (0.69m). These large differences are not due to different wave regimes in the different oceans but signify that something went wrong when the processing unit was replaced. It might be related to the wire connections or the hardware assembly of the Arduino shield or the RPI.

The altimeter probes of the new processing unit are not functioning correctly, but the main IMU and processing unit are. Figure 18c shows that the vertical fluctuation of the IMU is the reason for the surface fluctuation, with no contribution from the altimeter probes, compared to Figure 17c. It is possible to calculate the wave properties for the IMUs fluctuation only, but it will be shown in Section 4.2.1 that the combination of altimeter probes and IMU is better. Hereby, only data from the original processing unit will be considered further (black track in Figure 8), comprising 140 days at sea.

The values from the different altimeter probes and IMUs are studied further. Figure 19a shows the 30-minute minimum, mean, and maximum values for each altimeter probe. Table 8 summarizes the overall values and the number of values exceeding specified thresholds. Probe ug1 has the highest mean value of 11.23m because it is mounted highest at the ship (Figure 1). Probe ug2 has the lowest mean value, and even though the radar is mounted at the same location as ug2, the radar has a 2.77m higher mean value. All three altimeter probes exceed their maximum datasheet values of 15.2m and 15m for the ultrasonic and radar probe, respectively. This is acceptable and probably due to some noise introduced by the analog and digital electronics involved.

Table 8: Minimum, maximum and mean distance measured by each altimeter probe and the number of measurements exceeding specified thresholds.

| Distance | Min [m] | Mean [m] | Max [m] | Exceeding 15.2m [%] | Exceeding 15.8 [%] | Exceeding 0m [%] |
|---|---|---|---|---|---|---|
| ug1 | 0.65 | 11.23 | 15.78 | 2.73 | - | - |
| ug2 | 0.82 | 7.02 | 15.50 | 0.001 | - | - |
| radar | -1.82 | 9.79 | 15.57 | 4.13 | - | 0.006 |
| inverted radar | -0.52 | 9.79 | 30.94 | 2.89 | 1.99 | - |

The number of values exceeding the threshold of 15.2m indicates the saturation of the probes, meaning the value recorded when the signal cannot reach the sea surface. The saturation is 4.13% for the radar, 2.73% for ug1, and negligible for ug2. The original radar fluctuation has some negative values below 0m, which are physically impossible. The inverted radar fluctuation has only one event with negative values but some unrealistic large maximum values, reaching 30.94m. These maximum values are not measured but are a consequence of inverting

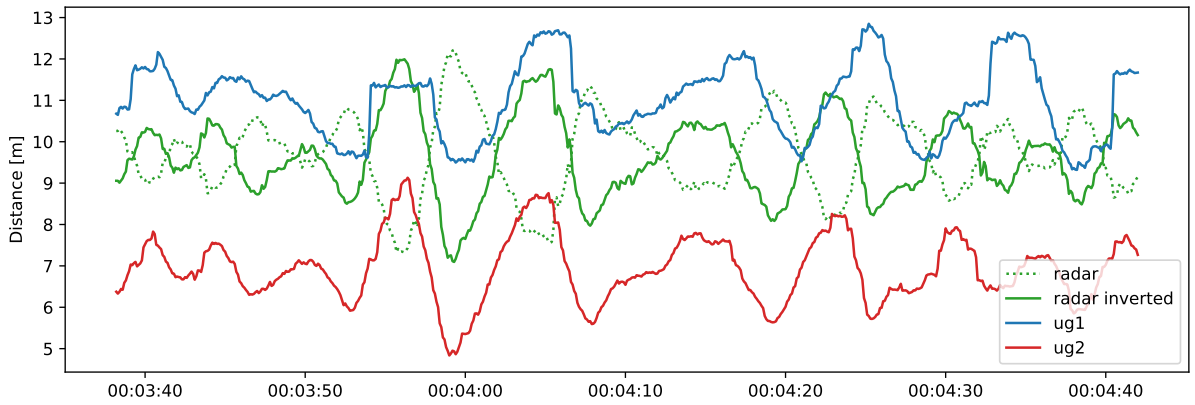


(a)

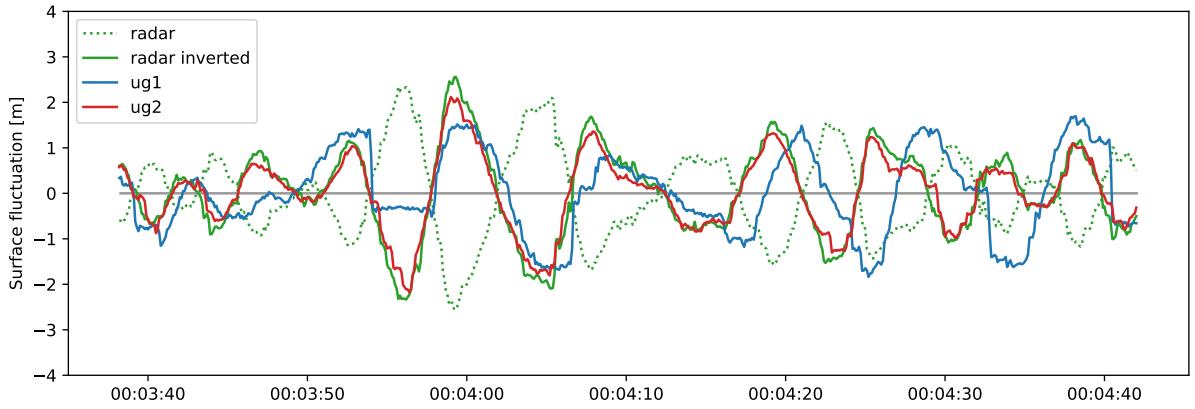


(b)

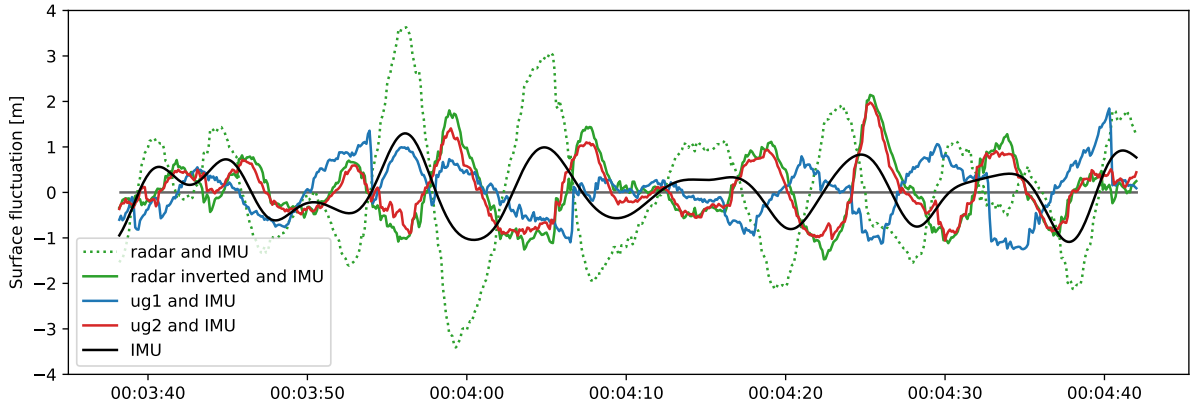


(c)

Figure 17: Raw data from the original processing unit 22.10.21, showing 60 seconds of the (a) total distance measured by the probes, (b) surface fluctuation calculated from the probes only, and (c) surface fluctuation calculated from the combination of probes and IMU, compared to IMU only.

the fluctuation and should be neglected. Therefore the measurements exceeding 15.8m are neglected, which discards 1.99% of the unrealistic radar values but does not affect the ultrasonic probes.

The surface fluctuation of each probe and IMU is also studied further (Figure 19b). Table 9 lists the total minimum and maximum values and the average standard deviation (Equation 17). The radar probe has the highest standard deviation of 1.72m, ug1 second highest of 1.27m, while ug2 has the lowest deviation of 0.77m. Figure 19b shows that the IMU fluctuations have smaller amplitudes than the probe fluctuations, and there is less variation between the IMUs

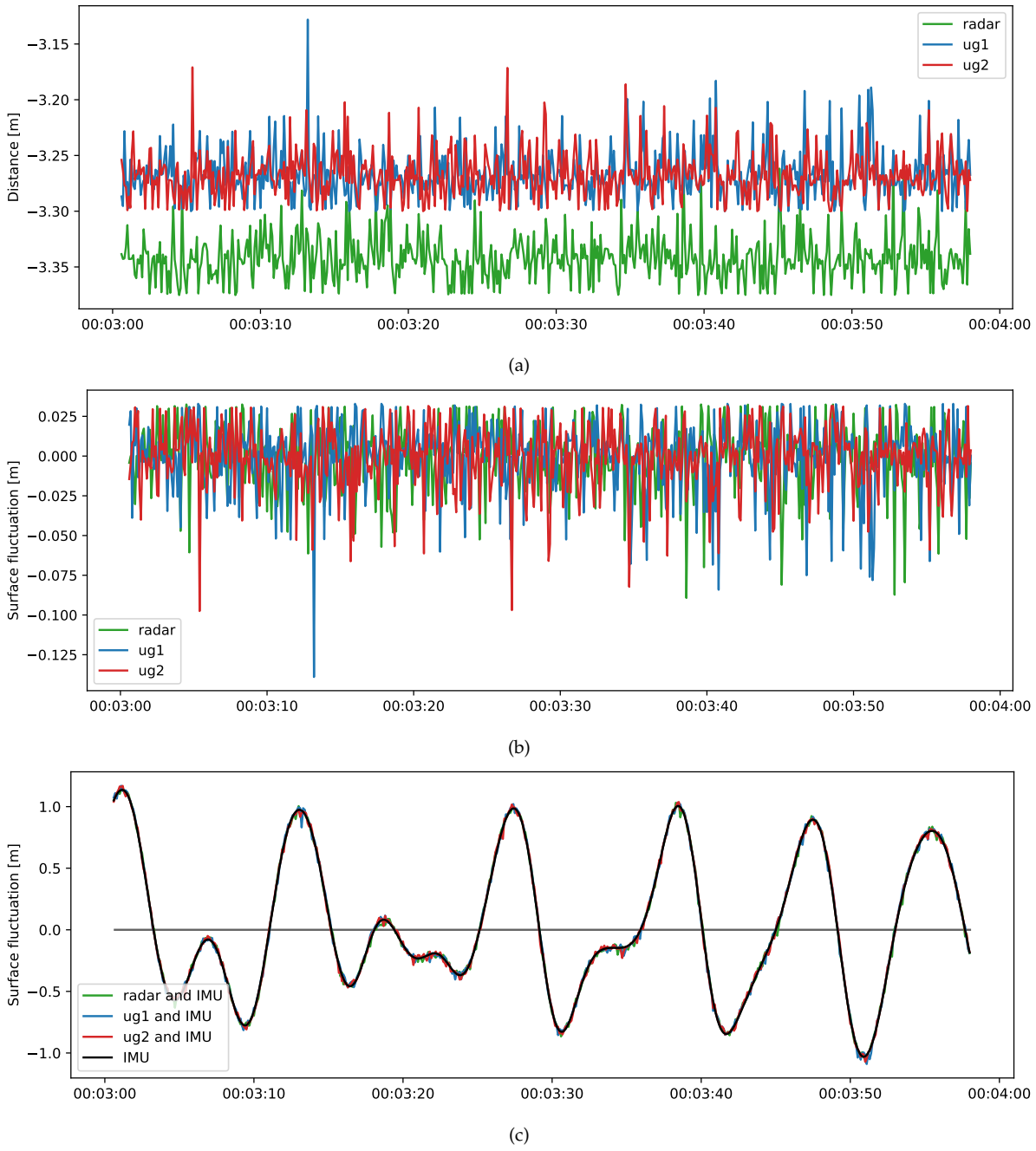


Figure 18: Raw data from the new processing unit 15.11.22, showing 60 seconds of the (a) total distance measured by the probes, (b) surface fluctuation calculated from the probes only, and (c) surface fluctuation calculated from the combination of probes and IMU, compared to IMU only.

than between the probes. All three IMUs have standard deviations of the surface fluctuation within the range of 0.71-0.79m, similar to ug2. Main IMU has the lowest standard deviation for both surface fluctuation, pitch, and roll. The time series of the IMU's roll and pitch fluctuation is shown in Appendix A. The absolute maximum roll and pitch values for the main IMU are 30.33° and 14.45°, corresponding to a factor of minimum 0.83 multiplied with the distance (Equation 4). Therefore the roll and pitch values do not make a significant impact on the distance measurements.

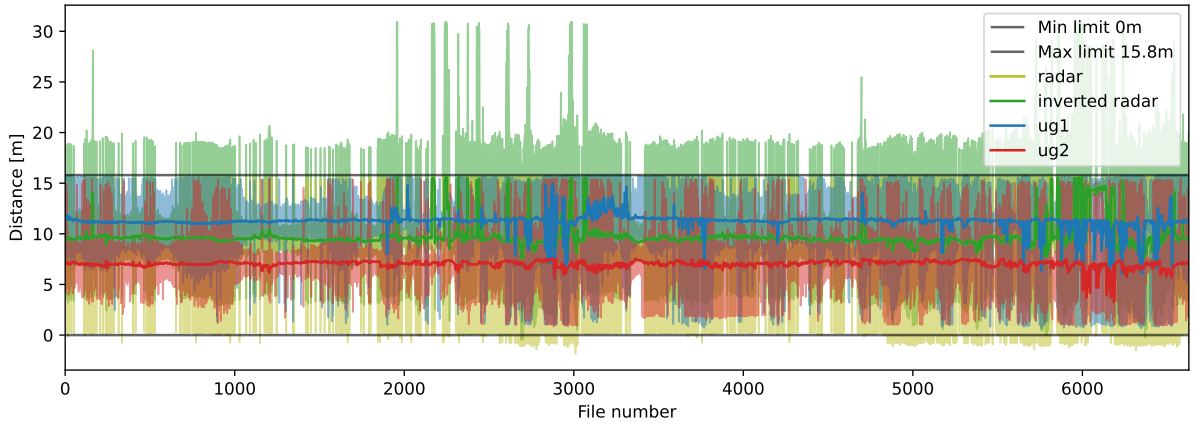


(a)

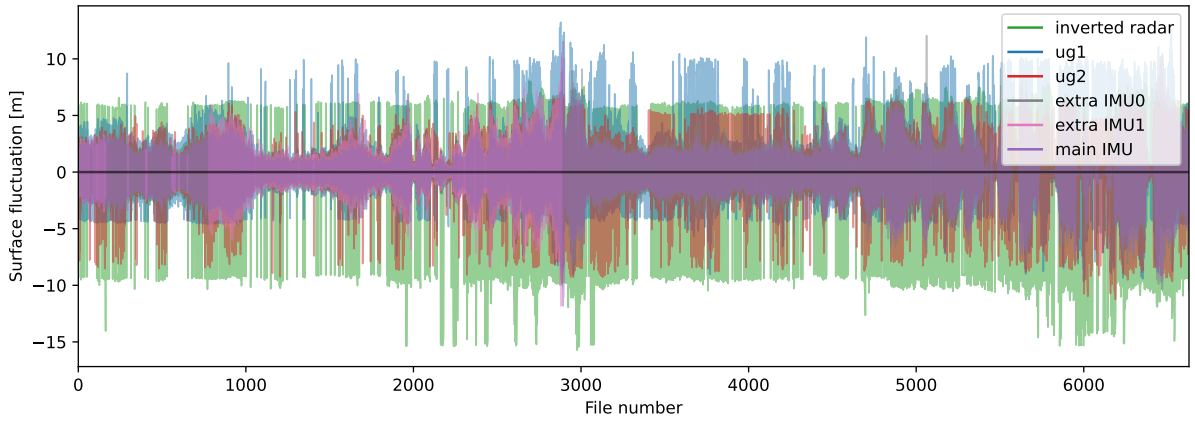


(b)

Figure 19: Minimum, maximum, and mean values for each 30-minute files of (a) distance measured by the altimeter probes and (b) surface fluctuation measured by the altimeter probes and the IMUs.

Table 9: Minimum and maximum value and average standard deviation of the surface fluctuation measured by each probe and IMU, and the values for pitch and roll fluctuation for each IMU.

| | | Min | Max | Std |
|---|---|---|---|---|
| Surface fluctuation [m] | radar | -15.73 | 8.05 | 1.72 |
| | ug1 | -10.00 | 13.23 | 1.27 |
| | ug2 | -11.25 | 6.49 | 0.77 |
| | extra IMU0 | -10.35 | 12.06 | 0.75 |
| | extra IMU1 | -11.82 | 10.11 | 0.79 |
| | main IMU | -11.81 | 11.54 | 0.71 |
| Pitch [°] | extra IMU0 | -22.01 | 22.13 | 1.55 |
| | extra IMU1 | -22.58 | 14.73 | 1.24 |
| | main IMU | -12.11 | 14.45 | 0.94 |
| Roll [°] | extra IMU0 | -34.21 | 35.80 | 2.21 |
| | extra IMU1 | -42.90 | 37.30 | 2.69 |
| | main IMU | -30.33 | 25.76 | 1.75 |

## 4.2 Software Development

I have enhanced the post-processing procedure developed by Fabian Knoblauch (Knoblauch, 2022). Figure 20a shows the significant wave height during leg 2 (red track in Figure 8) calculated with the original post-processing procedure, equivalent to Figure 5.4 in Knoblauch, 2022. Note that I am calculating the significant wave height with Hs = $4\sqrt{m_0}$, instead of SWH = $4\sigma(\eta)$. But Figure 5.1 of Knoblauch, 2022 shows that the method used for calculating signifi-

cant wave height gives very similar results.

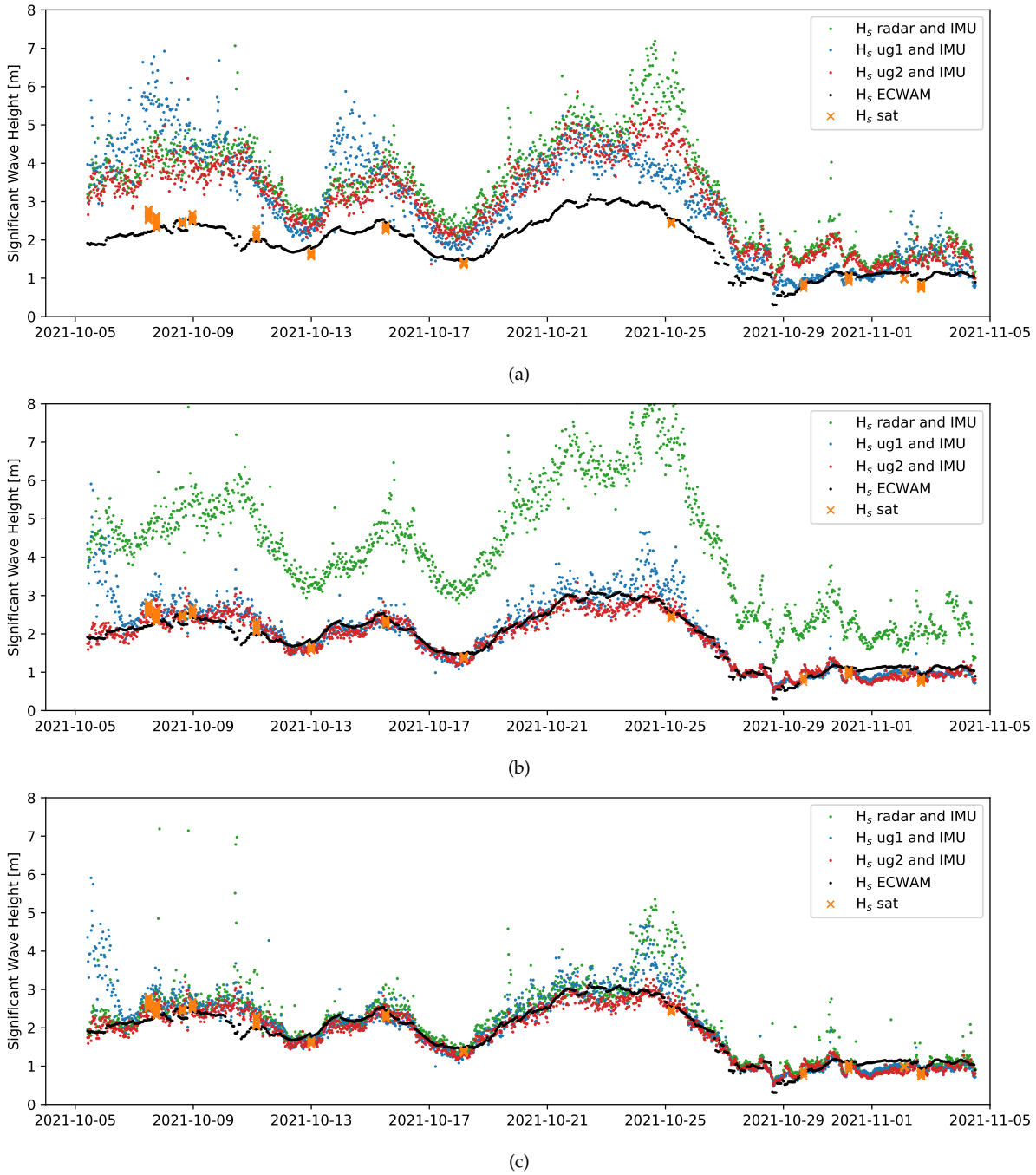


Figure 20: Significant wave height during leg 2 for (a) the original processing procedure and the new procedure with (b) original radar fluctuation and (c) inverted radar fluctuation, compared to ECWAM and satellite data.

Firstly, there was an error in the IMU readings, taking the roll value as the pitch value. Correcting the pitch value improved the fit for ug1 but not the ug2 and radar probes. This is because the original post-processing procedure was concentrated on ug1. Data was originally cut off at the beginning and end of each ug1 and IMU file because the Fourier transformation might cause some errors. But the ug2 and radar elevation was not cut off, which caused the ug2 and radar fluctuations to be shifted in time relative to the IMU fluctuation. In addition, the occurrences where ug1 measured a distance exceeding 14.75m were removed from all three altimeter probes. Since the probes are mounted at different locations, the timing of maximum ug1 elevation does not correspond to maximum ug2 and radar elevation. In the new proce-

dure, the cut off is implemented also for the ug2 and radar probes, and ug1's elevation limit is removed.

These changes improved the measurements by ug1 and ug2 as illustrated in Figure 20b, but the radar values actually obtained larger discrepancies from the ECWAM and satellite data. Inverting the radar fluctuation, as discussed in Section 4.1, results in a good fit for the radar as well, shown in Figure 20c. However, outliers of 4-5m for ug1 and radar probes are evident in the time series, but no filtering has been applied to better understand the uncertainties related to the different system components.

### 4.2.1 The System Components

The ship mounted wave system consists of multiple sensors at different locations on the ship to obtain the best combination (Figure 1). The extra IMUs were mounted at the probe locations because they were expected to resemble the vertical fluctuation of the altimeter probes better than the main IMU below deck. Since the extra IMUs were not expected to function for the entire expedition, Knoblauch, 2022 developed several alternative functions for fitting the main IMU to the motion of the extra IMUs. This function-fitting algorithm requires more post-processing than using the main IMU directly and is therefore evaluated. Significant wave height is used as the evaluation parameter because it will be shown in Section 4.3 that it has a better fit with ECWAM and satellite data than the peak period.

The statistical values of the significant wave height calculated for different system combinations, compared to ECWAM and satellite data, are summarized in Table 10. An illustration of the differences during leg 2 is found in Appendix A.

Table 10: Statistical values of the significant wave height using different system combinations compared to ECWAM and satellite data. The system combination with the best statistics (ug2 and main IMU) is marked in bold.

| | | ECWAM | | | Satellite | | |
|---|---|---|---|---|---|---|---|
| | | ug1 | ug2 | radar | ug1 | ug2 | radar |
| RMSD [m] | Probe solely | 1.91 | 1.01 | 2.81 | 1.74 | 1.03 | 2.74 |
| | Probe and main IMU | 1.63 | **0.53** | 2.67 | 1.27 | **0.36** | 2.37 |
| | Probe and fit IMU | 1.60 | 0.50 | 2.55 | 1.33 | 0.38 | 2.35 |
| | Probe and extraIMU | 1.66 | 0.66 | 2.59 | 0.66 | 0.52 | 2.37 |
| | extra IMU solely | 1.47 | 1.06 | 1.06 | 1.01 | 1.05 | 1.05 |
| | main IMU solely | 0.86 | 0.86 | 0.86 | 0.83 | 0.83 | 0.83 |
| MD [m] | Probe solely | 1.59 | 0.60 | 1.86 | 1.44 | 0.59 | 1.88 |
| | Probe and main IMU | 0.81 | **0.17** | 1.55 | 0.52 | **0.15** | 1.41 |
| | Probe and fit IMU | 1.10 | 0.08 | 1.36 | 0.85 | 0.06 | 1.37 |
| | Probe and extraIMU | 0.74 | 0.31 | 1.43 | 0.29 | 0.29 | 1.44 |
| | extra IMU solely | 1.14 | 0.74 | 0.74 | 0.71 | 0.72 | 0.72 |
| | main IMU solely | 0.54 | 0.54 | 0.54 | 0.53 | 0.53 | 0.53 |
| R | Probe solely | 0.76 | 0.78 | 0.69 | 0.77 | 0.79 | 0.72 |
| | Probe and main IMU | 0.76 | **0.93** | 0.73 | 0.64 | **0.96** | 0.75 |
| | Probe and fit IMU | 0.78 | 0.91 | 0.70 | 0.69 | 0.94 | 0.74 |
| | Probe and extraIMU | 0.72 | 0.92 | 0.73 | 0.83 | 0.95 | 0.77 |
| | extra IMU solely | 0.86 | 0.90 | 0.90 | 0.84 | 0.91 | 0.91 |
| | main IMU solely | 0.91 | 0.91 | 0.91 | 0.93 | 0.93 | 0.93 |
| N | Probe solely | 3050 | 3050 | 3050 | 56 | 56 | 56 |
| | Probe and main IMU | 3050 | **3050** | 3050 | 56 | **56** | 56 |
| | Probe and fit IMU | 3050 | 3050 | 3050 | 56 | 56 | 56 |
| | Probe and extraIMU | 1132 | 3050 | 3050 | 17 | 56 | 56 |
| | extra IMU solely | 1132 | 3050 | 3050 | 17 | 56 | 56 |
| | main IMU solely | 3050 | 3050 | 3050 | 56 | 56 | 56 |

Using the altimeter probes solely with no motion compensation from IMU gives the largest

deviation for ug1 and radar. For these two probes, the IMUs solely actually give better correlation and less deviation than in combination with the probes. The best correlation and lowest deviation are found for ug2 in combination with the main IMU, marked with bold text in Table 10. Only this combination will be studied further in this thesis.

### 4.2.2 Effect of Correcting Roll, Pitch and Yaw

The IMUs are not mounted perfectly horizontally or perfectly aligned with the ship's x-axis, as ideally shown in Figure 4. Knoblauch, 2022 describes a method for correcting the default offset angles of pitch, roll, and yaw. The method returns the offset angles listed in Table 11, and compensates the offset for each IMU. To validate the effect of correcting the angles, the statistics listed in Table 10 are calculated for the corrected angles.

Table 11: The offset angles for roll, pitch, and yaw for each IMU.

| | Roll [°] | Pitch [°] | Yaw [°] |
|---|---|---|---|
| main IMU | -0.17 | 1.78 | 3.00 |
| extra IMU0 | 11.43 | -7.98 | 31.80 |
| extra IMU1 | 10.99 | -30.97 | -2.50 |

The largest improvement is found for ug1 in combination with extra IMU0, with the RMSD decreasing from 1.66m to 1.62m for ECWAM and from 0.66m to 0.56m for satellite data. For ug2 in combination with extra IMU1, the correction also lowers the RMSD by a few decimals, but in combination with the main IMU, the values remain unchanged. This indicates that large offset angles (30°) benefit the correction, but small offsets, such as the main IMU angles in Table 11, do not need correction. Since I am using ug2 in combination with the main IMU further in this thesis, no angle corrections will be performed.

## 4.3 Wave Properties

The significant wave height and peak period measured by the ship mounted system are further quantified by ECWAM and satellite data. The time series of all the data is found in Appendix A. The significant wave height fits very well with satellite data, with a correlation coefficient of 0.96 and RMSD of 0.36m, shown in Figure 21a. It should be noted that the maximum wave height collocated with satellite data is 5.18m, which is 0.25m lower than the satellite value, both measured while rounding the Cape Horn.

The significant wave height compared to ECWAM includes larger wave heights as illustrated in Figure 21b. Nevertheless, there is a good fit, with a correlation coefficient of 0.93 and RMSD of 0.53m. The quantile-quantile line in Figure 21b shows that the fit is best for significant wave heights up to 6m. The largest observations are overestimated, resulting in a positive MD of 0.17m. The mean observed wave height is 2.07m, located within the range that correlates well with model and satellite data. The maximum significant wave heights, marked blue in Figure 21b, are a maximum of 5.09m larger than the model, discussed further in Section 4.3.1. The second largest waves of 9.73m, were measured on the south coast of Chile the 26.04.22 and are 3.32m larger than estimated by ECWAM. The third largest waves were measured while rounding Cape Horn the 03.03.22 with a good agreement between the measured (6.62m) and forecasted wave height (6.50m).

The effect of Doppler shifting the significant wave height is lowering the correlation coefficient to 0.92, and increasing the RMSD by 0.17m and 0.12m according to satellite and ECWAM data, respectively (not shown). Therefore, only the original significant wave height will be studied further in this thesis. On the other hand, the statistical values remain similar for the original, and Doppler shifted peak period, shown in Figure 21c and 21d.

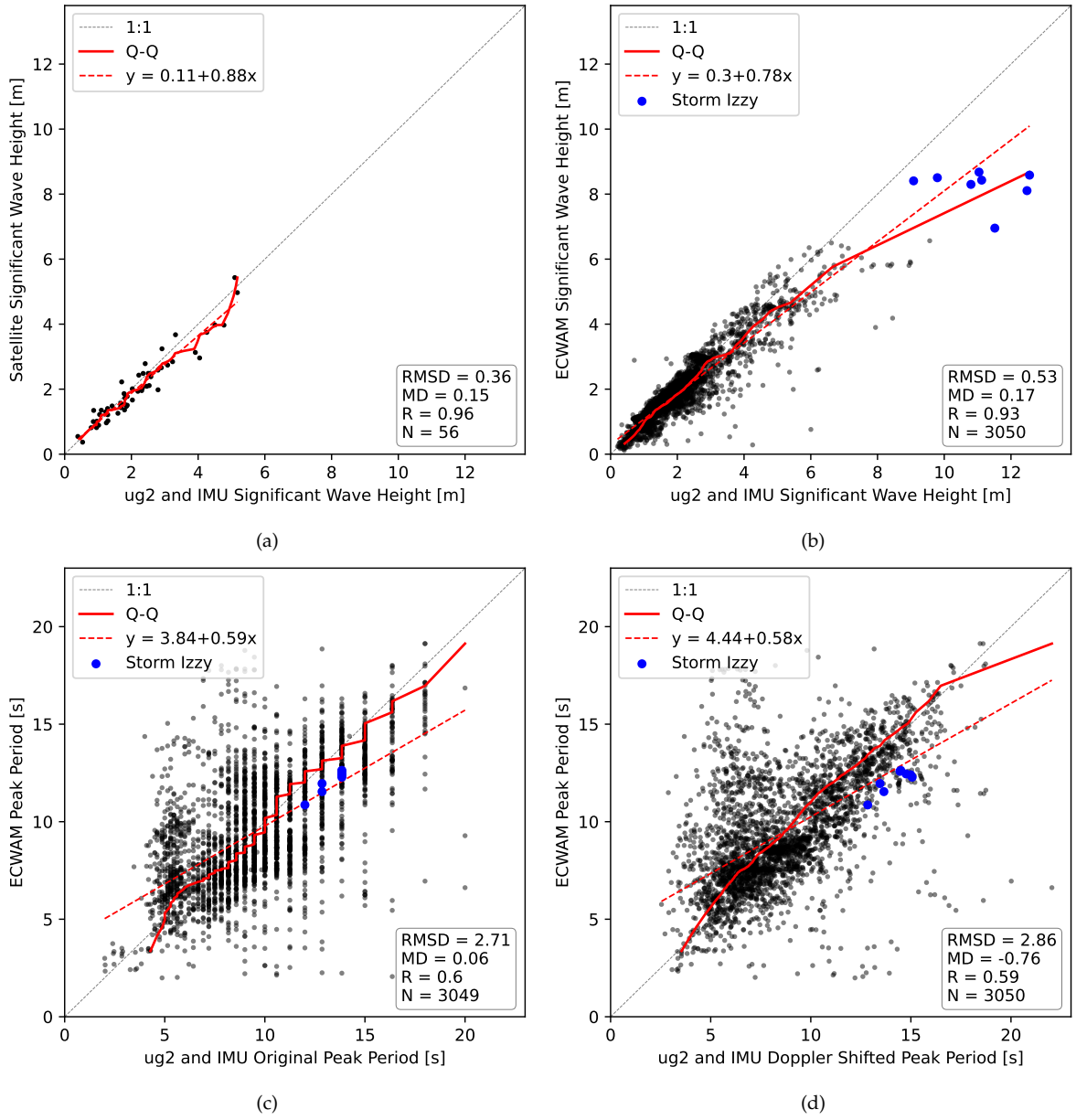


Figure 21: Significant wave height measured by ug2 and IMU compared to satellite data (a) and ECWAM (b). Original peak period (c) and Doppler shifted peak period (d) measured by ug2 and IMU compared to ECWAM. The solid red line is the quantile-quantile fit (Q-Q), while the red dotted line is the linear regression (y). Blue dots are values measured during storm Izzy.

The original peak period has a step-behavior as a consequence of the sampling rate and calculation method (Equation 16). Even though the frequencies are evenly spaced, the division with small frequencies has a larger spacing (1/0.1Hz = 10s, 1/0.2Hz=5s) than the division with high frequencies (1/0.4Hz = 2.5s, 1/0.5Hz=2s). The Doppler shift introduces a disturbance dependent on the frequency (Equation 12) so that frequencies are not evenly spaced and the resulting Doppler shifted peak period does not have the step-behavior. Both the original and Doppler shifted peak periods will be studied further in this thesis and evaluated in Section 5.1.1.

There is more spread between observations and ECWAM for the peak period than for significant wave height (Figure 21c and 21d). The RMSD is larger (2.71s), and the correlation coefficient is lower (0.6). The original peak period is limited by the frequency range 0.05-0.5Hz, corresponding to a maximum peak period of 20s and a minimum of 2s. The maximum and

minimum Doppler shifted peak periods are shifted to higher values of 22.04s and 2.54s, respectively. But on average, the original peak period (9.52s) is larger than the Doppler shifted (8.80s). Since the original peak period has no significant MD compared to the ECWAM, the Doppler shifted peak period obtains a negative MD of 0.76s. The linear regression line illustrates that the short peak periods are underestimated while the long peak periods are overestimated. The maximum peak periods do not correspond to the storm Izzy, but the rounding of Cape Horn, where ECWAM estimated a 14.02s shorter peak period (Figure 21c and 21d).

The relation between peak period and significant wave height is studied further. Figure 22a illustrates that there is a positive correlation between the original peak period and the significant wave height, with a correlation coefficient of 0.37. Statistics are similar for the Doppler shifted peak period (not shown). The blue circles identify the storm Izzy, with very large wave heights and a peak period of 10-15s. The maximum peak periods of 20s correspond to significant wave heights of maximum 7m. Thus, the highest peak periods do not necessarily correspond to the highest waves. This is due to the dispersion of waves in deep water since the propagation speed of wave energy depends on the frequency of the wave components (Equation 10). Low-frequency waves travel faster than high-frequency waves. The initially random, short-crested wave field with steep waves generated in a storm will disintegrate into individual, long-crested wave fields (Holthuijsen, 2007d).

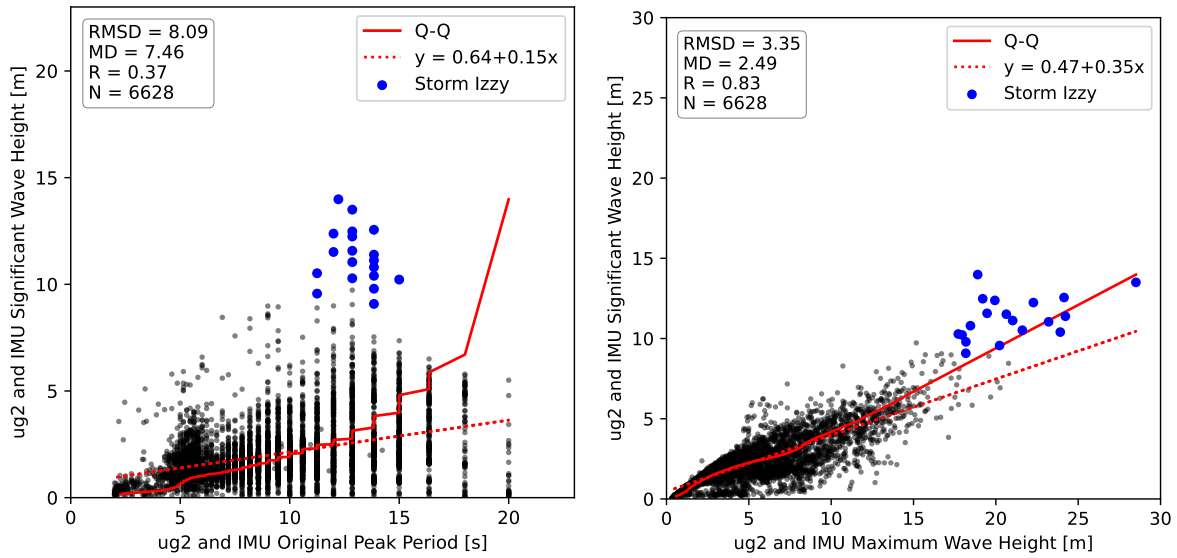


Figure 22: Original peak period (a) and maximum wave height (b) in relation to significant wave height measured by ug2 and IMU. The solid red line is the quantile-quantile fit (Q-Q), while the red dotted line is the linear regression (y). Blue dots are values measured during storm Izzy.

Moreover, the relation between maximum and significant wave height is investigated. The two wave heights have a good fit, with a correlation coefficient of 0.83, shown in Figure 22b. As expected, the maximum wave height is larger than the significant wave height. On average, the maximum wave height is 2.46 times larger than the significant wave height, remarkably larger than the estimated value $H_{max} \approx 2H_s$ (Holthuijsen, 2007c).

### 4.3.1 Storm Izzy in the North Atlantic Ocean

The largest significant wave height of 13.99m was measured during the major winter storm Izzy in the North Atlantic Ocean ("extra IMU1 broken" in Figure 8). This storm is studied in detail to understand the discrepancies between the measurements and ECWAM 21b.

The storm system entered the Atlantic Ocean the 14.01.22 at 12:00 and traveled North-East until it reached the maximum wind speed of 36.49m/s and significant wave height of 11.57m at the southern tip of Greenland 17.01.22 (not shown). Unfortunately, extra IMU1 got destroyed on 15.01.22 at 05:00, which caused a breakdown of the wave system and no wave measurements during the rest of the storm. The destruction of extra IMU1 is probably due to mechanical forces from the severe sea; maybe a large wave hit the bowsprit. In addition, three of the storm sails were destroyed during the storm. Storm sails are the most solid sails, which are always set first and recovered at last during a storm (Officer Statsraad Lehmkuhl, personal communication, October 2022).

The visual observations by the officer on Statsraad Lehmkuhl are storm on the Beaufort scale and 9-14m wave height on the Douglas scale. This is the only event during the parts of the expedition I have studied, with levels 10 and 8 on the Beaufort and Douglas scale, respectively. Figure 23 illustrates the conditions onboard Statsraad Lehmkuhl during the storm, with large roll angles and sea spray over board.

A maximum wind speed of 26.02m/s was measured at the ship the 14.01.22 at 23:00, shown in Figure 24a. ECWAM's wind field the 15.01.22 at 00:00 has a maximum wind speed of 25.03m/s in the vicinity of the ship. Moreover, the maximum wind speed observed by satellites in the same area was 21.81m/s. Satellite data was not available within the time constraint of 15 minutes (Table 7), but the crossing of Sentinel-6A was found within 20 minutes.

Statsraad Lehmkuhl was located in the center of the storm when the maximum wave height was measured, illustrated in Figure 24b. The maximum significant wave height measured by the ship mounted system is 5.07m and 5.09m larger than satellite and ECWAM values, respectively. Since there is only a 0.02m difference between the ECWAM and satellite values, it is anticipated that the measurement system has overestimated the significant wave height. Figure 24b also displays ECWAM's mean wave direction compared to the partition into the direction of wind sea and swell. The arrow length is scaled with the significant wave height of each partition. The maximum significant wave height of the wind sea (8.90m) is larger than the maximum significant wave height of the swell (5.81m), as expected during a storm.

As for significant wave height, the measurement system is also overestimating the peak period. Figure 24c illustrates that the maximum original peak period measured during the storm was 15.00s, while ECWAM estimated a maximum peak period of 12.38s. The arrow length in Figure 24c is scaled with the wind sea peak period, swell peak period, and peak wave period. The wind sea direction fits well with the anticlockwise rotation of the wind direction in Figure 24a. The mean wave direction is aligned with the swell direction outside the center of the storm (30N, 45W), while it follows the wind sea where the wind speed is strong (35N, 70W). At the ship's location, the mean wave direction is aligned with the wind sea direction, and the waves are coming towards the starboard bow of the ship. Since the ship is sailing into waves, the frequencies are Doppler shifted to lower values, and thus the maximum Doppler shifted peak period is 0.73s higher than the original. In some areas, the mean wave direction resembles neither wind sea or swell, such as south of the ship (35N, 60W).

Figure 23: Pictures onboard Statsraad Lehmkuhl in the North Atlantic Ocean the 14.01.22 (Photographer: Torjus Håven/Statsraad Lemkuhl).

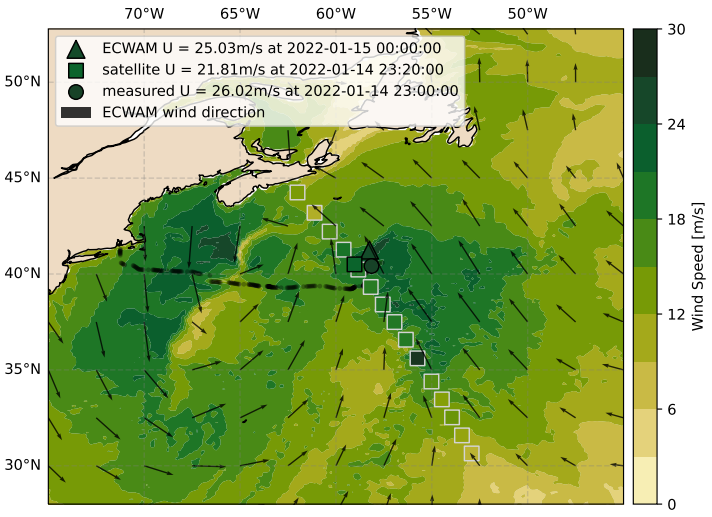


(a)

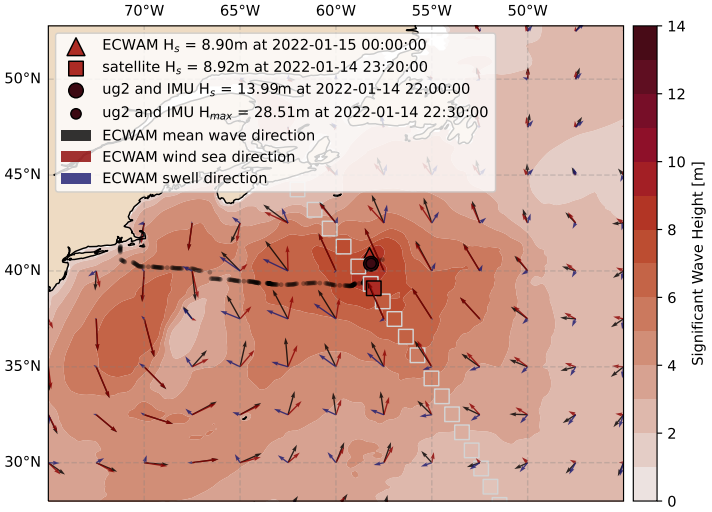


(b)

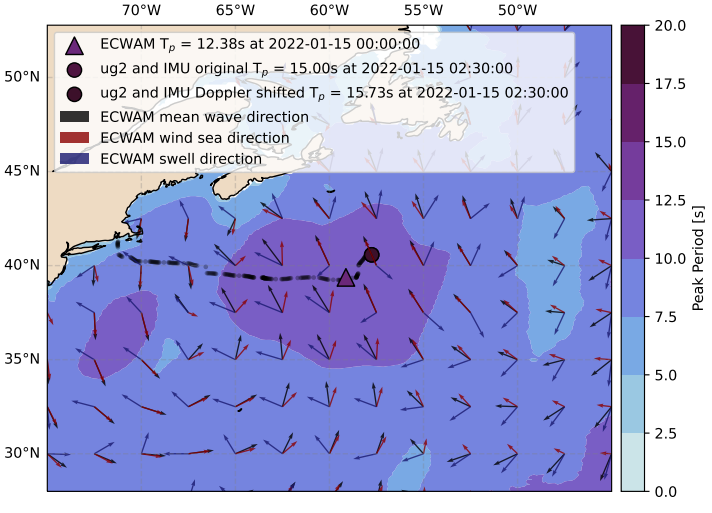


(c)

Figure 24: ECWAM's (a) wind speed and direction (b) significant wave height and (c) peak period in the North Atlantic east of New York the 15.01.22 00:00. Arrows for mean wave direction, wind sea direction, and swell direction is scaled with each partition's (b) significant wave height and (c) peak period. The maximum ECWAM value is marked with a triangle, the maximum satellite value is marked with a square, and the maximum value measured at the ship is marked with a circle. The ship track from New Port is dotted in black.

The maximum wave height during the storm was measured by ug2 and IMU to be 28.51m, 2.04 times the significant wave height. This wave is defined as a freak wave by the generally accepted criterion $H_{max} > 2H_s$ (Dysthe, Krogstad, and Müller, 2008; Holthuijsen, 2007c). Figure 25a illustrates that ug2 and IMU measured a crest height of 13.89m and a trough of 14.62m. The crest height is 0.99 times the significant wave height, not considered a freak wave by another frequently used criterion $\eta_c > 1.25H_s$ (Dysthe, Krogstad, and Müller, 2008). A trough larger than the crest is unexpected because nonlinear processes generally make the wave crest sharper and higher, and the wave troughs flatter and shallower (Holthuijsen, 2007c).

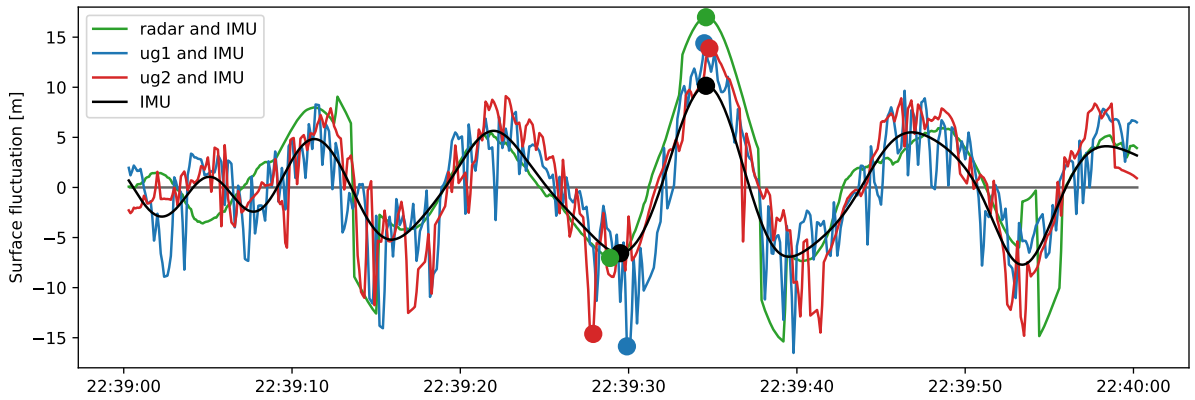


(a)

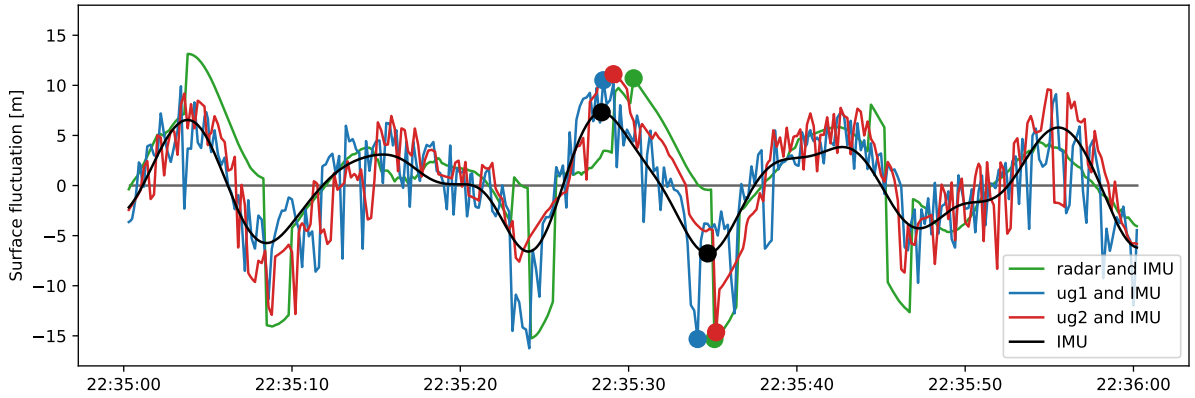


(b)

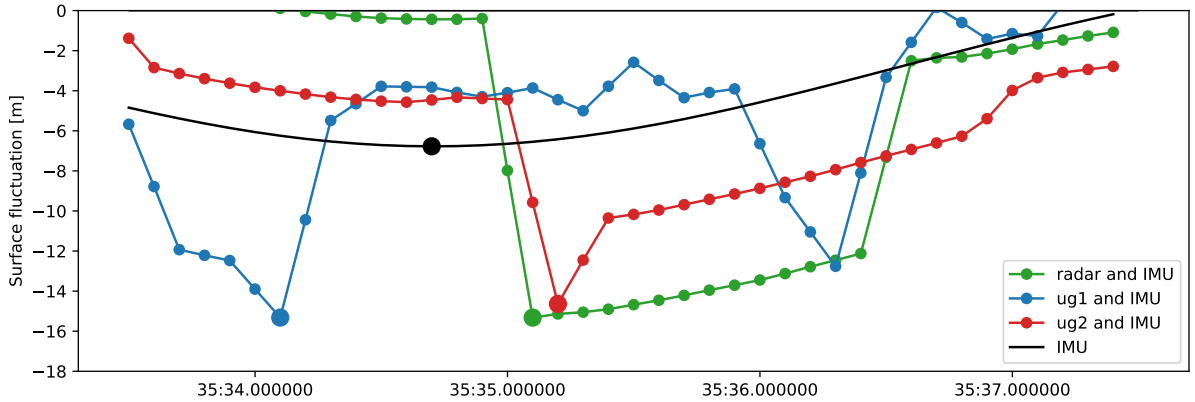


(c)

Figure 25: The surface fluctuation over 60 seconds showing the maximum wave height (a) according to the downcross definition measured at 14.01.22 22:39:30 and (b) according to the upcross definition measured at 14.01.22 22:35:30, (c) zoomed in at the minimum values of the upcross definition 22:35:35.

Similar values were measured by ug1 and IMU with a crest height of 14.39m and a trough of

15.85m, but it was not defined as a wave due to a fluctuation around the zero-crossing (Figure 25a). In this event, the radar probe and IMU measured more realistic values, with crest height (16.99m) larger than the trough (6.66m). The IMU fluctuation alone is also more realistic, with a crest of 10.15m, and a trough of 6.56m (Figure 25a).

If the upcross definition of a wave is used instead of the downcross definition, the maximum wave height values differ. For the radar and IMU, the successive trough in Figure 25a is deeper (15.38m), resulting in a maximum wave height of 32.36m. However, this wave is not defined by ug2 and IMU due to a fluctuation around the zero-crossing. Instead, the maximum wave height is measured 4 minutes earlier, shown in Figure 25b. The maximum wave height is 25.75m, which is 2.76m lower than the downcross definition. For ug1 and radar in combination with IMU, similar wave heights are measured of 25.83m and 26.02m, respectively. But neither is this wave defined as a wave by ug1 due to a fluctuation around the zero-crossing (Figure 25b).

The deep trough in Figure 25b is measured by all three altimeter probes and studied further in Figure 25c. For all three probes, the minimum value is not a single point but has neighboring low values. However, the height varies by 12m for the ultrasonic probe and 16m for the radar probe within 0.2 seconds. These rapid fluctuations are not realistic and indicate that the distance measurements are disturbed in the rough sea. Moreover, the fluctuation is more frequent than on a calm day (Figure 17c). The radar fluctuation during the storm is less rapid and actually more realistic than the ultrasonic probes, even though it measured some very large changes over a short time. This example argues that both the instruments and calculation method are very sensitive to outliers which makes the estimation of freak waves unreliable.

## 4.4 Factors Influencing the Wave Measurements

Several external factors may be influencing the ship mounted wave measurements. To achieve a better understanding, these factors are studied in the following.

### 4.4.1 Wave Direction and Ship Speed

Firstly the direction of the wind, waves, and ship might influence the wave measurements. The wind speed measured at the ship has a correlation coefficient of 0.71 and 0.74, with satellite data and ECWAM, respectively, and can therefore be relied upon (Figure 33 Appendix B). However, the wind direction measured at the ship does not correlate with ECWAM's estimated wind direction (Figure 34 Appendix B). Since the observed wind direction is very spread and fluctuating, the ECWAM wind direction is studied further in this thesis instead.

The wave direction is mainly West and South-West, in the same direction as the wind, illustrated in Figure 26b and 26a. This relation is expected since ECWAM forecasts the wave spectrum from wind generation, among others. The heading of the ship is mainly South-South-West during the sailing route that I have studied (Figure 8). The wave direction relative to the ship $\theta$ (Equation 8), is illustrated in Figure 26d. Waves are mainly coming towards the stern, as expected since the wave direction and wind direction are similar, and Statsraad Lehmkuhl is preferably sailing with the wind inclined from behind (Officer Statsraad Lehmkuhl, personal communication, October 2022).

Secondly, the influence of the ship's speed is studied. The mean speed during the expedition route that I have studied was 2.96m/s, reaching a maximum ship speed of 6.34m/s. Cifuentes-Lorenzen et al., 2013 divided their ship mounted measurements into three categories, station (ship speed < 1m/s), slow (1m/s <= ship speed <= 3m/s), and fast (3m/s < ship speed < 6m/s). According to these categories, Statsraad Lehmkuhl was at station 10% of the route, 46% at slow

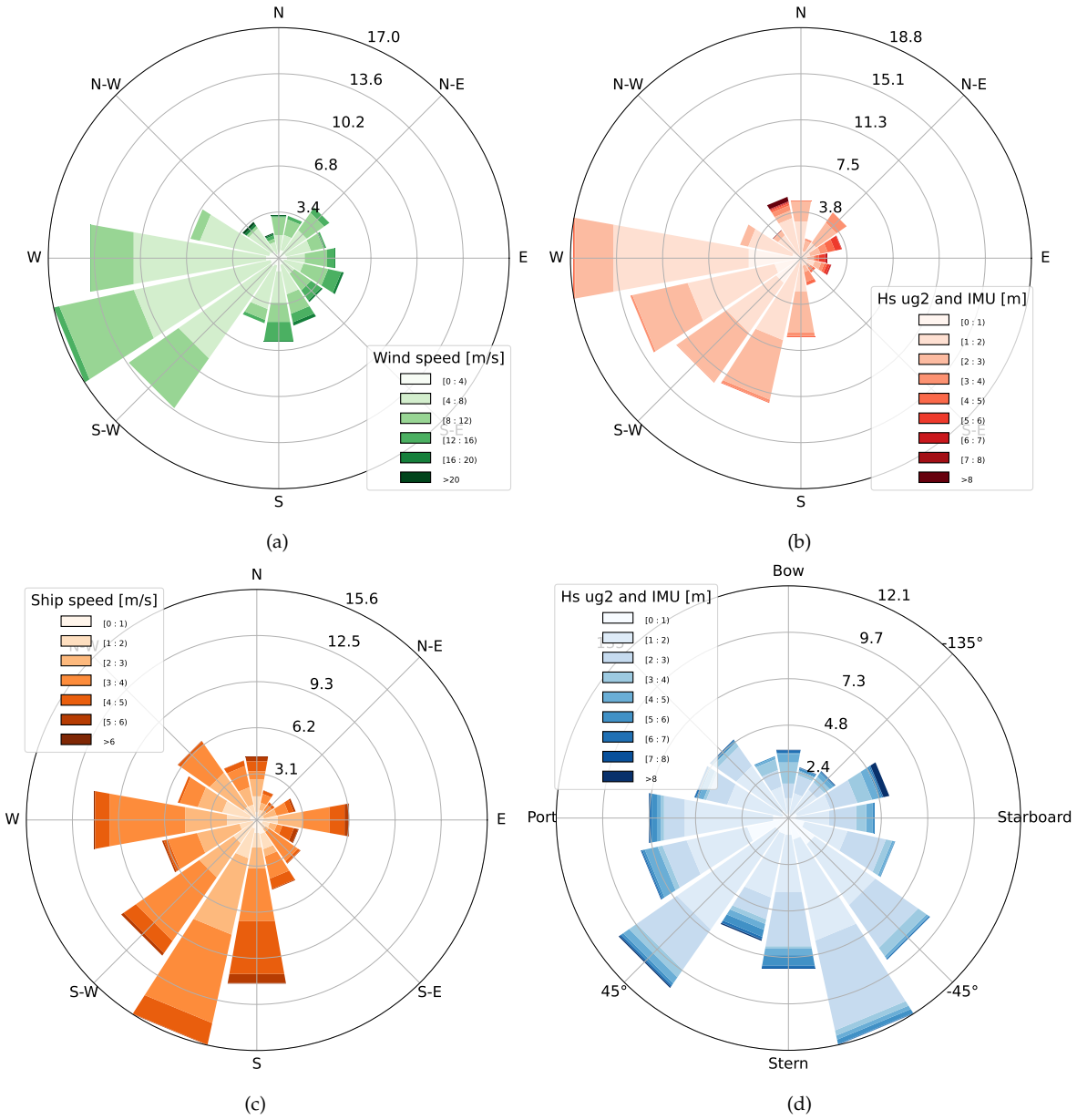


Figure 26: Directional roses for ECWAM (a) wind, (b) wave direction and (c) ship heading and (d) wave direction relative to ship ($\theta$). Directions are defined with oceanographic convention: going towards. The color contours represent (a) ECWAM wind speed, (b,d) significant wave height, and (c) ship speed. The number represents the percentage of values within each of the 16 directional bins.

speed, and 44% at fast speed. The speed categories are relatively spread out during the sailing route, and the stations are not related to the harbors, which are already discarded. Instead, the stations are related to CTD measurements in the open ocean. Since Statsraad Lehmkuhl is a sailing vessel, a still position is nearly accomplished by bracing the sail of the foremast and mainmast perpendicular to each other (Officer Statsraad Lehmkuhl, personal communication, October 2022).

I have studied the effect of ship speed in combination with wave direction. Cifuentes-Lorenzen et al., 2013 only considered waves opposing the ship within $\pm$ 90°, to avoid shadowing effects by the ship. Instead, I will consider all wave directions to evaluate whether this effect is present. Since the ug2 altimeter probe is positioned on the starboard side of the bow, I have separated the wave directions at $\pm$ 180°. Waves towards starboard, have negative $\theta$ angles

and are considered as opposing the sensor (right side of Figure 26d). The division provides a similar amount of waves towards starboard (49%) and port side (51%).

The statistical values for significant wave height and peak period compared to ECWAM data are listed in Table 12. The significant wave height has the lowest RMSD of 0.26m at station for waves towards port, and the deviation increase to a maximum of 0.91m at high ship speed for waves towards starboard. The correlation coefficient varies by a maximum of 0.05 between all wave directions and ship speeds. The statistics vary more for the peak period than the significant wave height (Table 12). The RMSD increases from minimum 1.76s at station to maximum 3.20s at high speed. Also, the correlation coefficient varies from a maximum of 0.80 at station to a minimum of 0.35 at high speed. Peak periods of waves towards starboard are better represented than waves towards port, especially at slow ship speed, with a difference in RMSD of 0.82s. This indicates that high ship speed and the shadowing effect of waves towards port side negatively impact the peak period measurements. Doppler shifting the peak periods is not improving the results in any direction or speed categories (not shown).

Table 12: Statistical values of the significant wave height and the peak period for different ship speeds and wave directions compared to ECWAM. Station is ship speed < 1m/s, slow is 1m/s <= ship speed <= 3m/s, and fast is 3m/s < ship speed < 6m/s. Waves toward port side have $\theta$ values between 0-180°, while waves towards starboard have $\theta$ values between 0-(-180°).

| | | Significant Wave Heigth | | | Original Peak Period | | |
|---|---|---|---|---|---|---|---|
| | | Station | Slow | Fast | Station | Slow | Fast |
| Port | RMSD [m] | 0.26 | 0.55 | 0.53 | 1.96 | 2.86 | 3.20 |
| | MD [m] | -0.14 | 0.12 | 0.27 | -0.04 | -0.70 | 0.09 |
| | R | 0.95 | 0.92 | 0.94 | 0.79 | 0.59 | 0.35 |
| | N | 100 | 615 | 835 | 100 | 615 | 835 |
| Starboard | RMSD [s] | 0.41 | 0.46 | 0.91 | 1.76 | 2.04 | 2.65 |
| | MD [s] | 0.05 | 0.12 | 0.59 | -0.39 | 0.12 | -0.71 |
| | R | 0.90 | 0.93 | 0.91 | 0.80 | 0.77 | 0.66 |
| | N | 87 | 647 | 758 | 87 | 647 | 758 |

I have further investigated which wavelengths are interrupted by shadowing effects. The waves are categorized as short for peak periods below 10s and long for peak periods above 10s, which are typical peak periods for swell (Rabault, Nose, et al., 2022). The division provides a similar amount of short waves (55%) and long waves (45%). The statistics for significant wave height and peak period compared to ECWAM are listed in Table 13.

Table 13: Statistical values of the significant wave height and the peak period for different wavelengths and wave directions compared to ECWAM. Short waves have a peak period below 10s, while long waves have a peak period above 10s. Waves toward port side have $\theta$ values between 0-180°, while waves towards starboard have $\theta$ values between 0-(-180°).

| | | Significant Wave Heigth | | Original Peak Period | |
|---|---|---|---|---|---|
| | | Short | Long | Short | Long |
| Port | RMSD [m] | 0.41 | 0.62 | 3.18 | 2.78 |
| | MD [m] | 0.14 | 0.24 | -1.60 | 1.33 |
| | R | 0.91 | 0.93 | 0.32 | 0.47 |
| | N | 827 | 727 | 827 | 727 |
| Starboard | RMSD [s] | 0.49 | 0.58 | 2.23 | 2.55 |
| | MD [s] | 0.17 | 0.12 | -0.25 | 1.21 |
| | R | 0.85 | 0.94 | 0.37 | 0.66 |
| | N | 868 | 626 | 868 | 626 |

The wavelengths are difficult to compare for significant wave height because both the RMSD and the correlation coefficient increase for longer waves (Table 13). However, the peak period of waves towards port side has a higher RMSD (3.18s) and lower correlation coefficient (0.32) for short waves than long waves. Moreover, the MD is larger for short waves towards port

(-1.60s) than towards starboard (-0.25s), suggesting that the ship dampens short waves toward port side. The statistical values differ less for long waves, indicating that long peak periods are less affected by shadowing effects than short peak periods.

### 4.4.2 Sailing Versus Motoring

The wave system described in this thesis is more likely to be used on motoring vessels than sailing vessels for future work. Therefore, I have studied whether there are any differences in the wave properties when the ship is sailing or not. During the route I have studied, the ship has utilized motor 21%, marked black in Figure 27a. When a combination of sail and motor is utilized, it is categorized as motoring. The motor is utilized in and out of harbor and when the ship has to go against the wind. When the ship is motoring, it is rather directed against the waves than perpendicular to the waves (Officer Statsraad Lehmkuhl, personal communication, October 2022). While sailing, the wave direction corresponds to the preferred wind direction, inclined from behind (Figure 27b). However, while motoring, the wave direction is mainly towards the bow and port side (Figure 27c). Moreover, there is a larger wave direction spread while motoring than sailing.

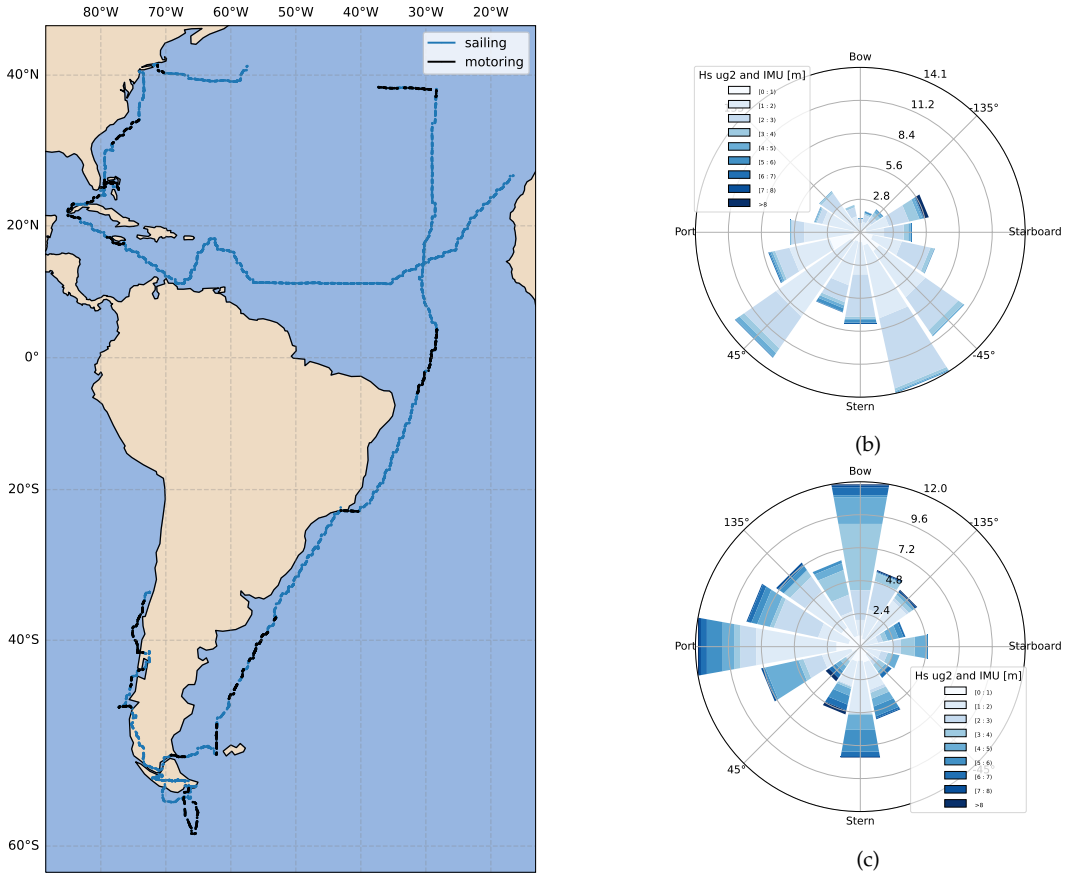


(a)

(b)

(c)

Figure 27: The track of the expedition route by motoring (black) or sailing (blue) (a) and wave direction relative to the ship ($\theta$) while (b) sailing and (c) motoring. Directions are defined with oceanographic convention: going towards. The color contours represent the significant wave height and the number represents the percentage of values within each of the 16 directional bins.

The statistical values for sailing or motoring compared to satellite and ECWAM are listed in Table 14. The significant wave height has a larger RMSD while motoring, but the correlation is also higher. For the peak period, the deviation is smallest, and the correlation is largest while

motoring. Similar values are found for the Doppler shifted peak periods (not shown).

Table 14: Statistical values of the significant wave height and peak period measured while the ship is sailing or motoring compared to ECWAM and satellite data.

| | | ECWAM | | Satellite | |
|---|---|---|---|---|---|
| | | Motor | Sailing | Motor | Sailing |
| Significant wave height | RMSD [m] | 0.71 | 0.46 | 0.50 | 0.28 |
| | MD [m] | 0.41 | 0.10 | 0.37 | 0.06 |
| | R | 0.95 | 0.91 | 0.98 | 0.95 |
| | N | 684 | 2364 | 16 | 40 |
| Original peak period | RMSD [s] | 2.51 | 2.95 | | |
| | MD [s] | -0.04 | -0.97 | | |
| | R | 0.64 | 0.58 | | |
| | N | 684 | 2364 | | |

These results do not agree with ship speed and wave direction findings. While motoring, the ship was 4% less on station, 8% less at slow ship speed, and 12% more at fast speed than while sailing. On average, the ship's speed was 0.33m/s larger while motoring, which should impact the peak periods negatively. Moreover, the wave direction is 60% towards port side while motoring, which is the least favored direction according to table 12. However, there is a significant difference in the number of collocated values in Table 14, which makes the results less statistically robust. Moreover, the largest significant wave heights and peak periods were measured during sailing, which was found to be overestimated and consequently impacts the statistics negatively. In addition, the differences may be related to different wave regimes.

### 4.5 Comparison with Drifter Measurements

The ship mounted wave measurements are compared to the wave measuring drifters deployed from the ship. However, the new wave system was not fully functioning where the drifters were deployed: Nanmadol in the South Pacific and Floaty in the Indian Ocean (Figure 8). Therefore the measurements are not compared directly but rather in terms of statistical values compared to ECWAM and satellite data.

The time series of significant wave height for Nanmadol and Floaty is illustrated in Figure 28, while scatter plots are shown in Appendix C. The significant wave height measured by satellite actually fits better with the drifters measurements than with ECWAM, such as for Nanmadol 21.09.22 and Floaty 28.11.22. The significant wave height measured by the drifters also agrees well with ECWAM with an RMSD of 0.20-0.29m and a correlation coefficient of 0.95-0.96. The drifter Nanmadol measured two periods with wave heights higher than the forecast. The 22.09.22, the measured value was 0.88m higher than the forecast and 0.68m higher than satellite data. The second highest wave measured at 30.09.22 was 0.95m higher than forecast. These discrepancies from model data are notably smaller than the 5.09m difference in significant wave height measured by the ship mounted wave system (21b).

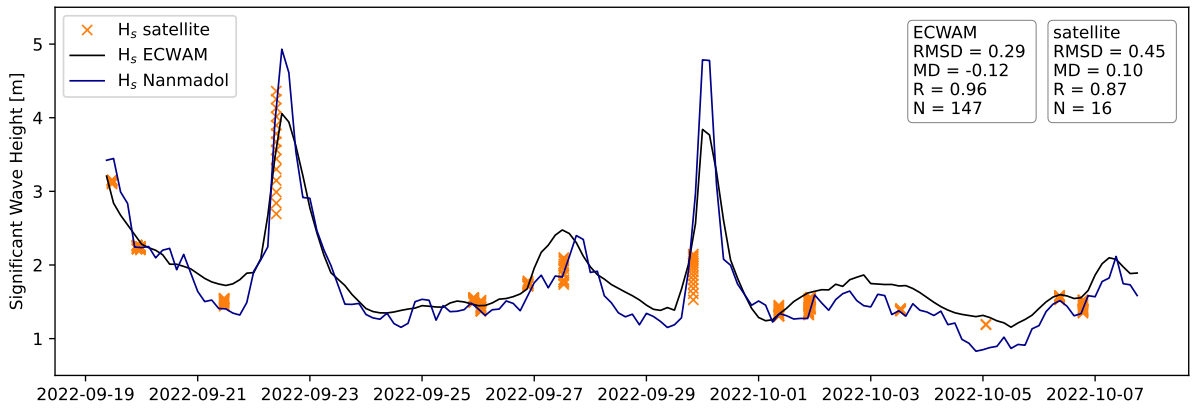


(a)

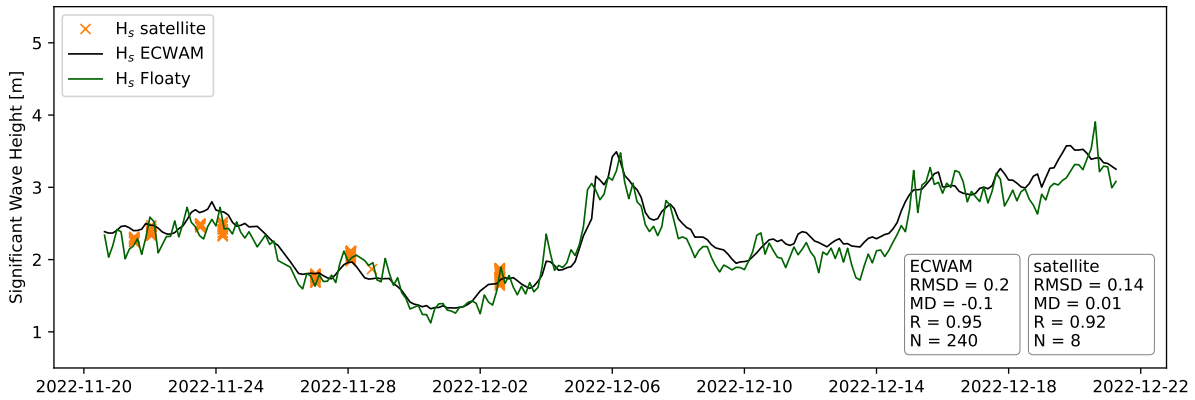


(b)

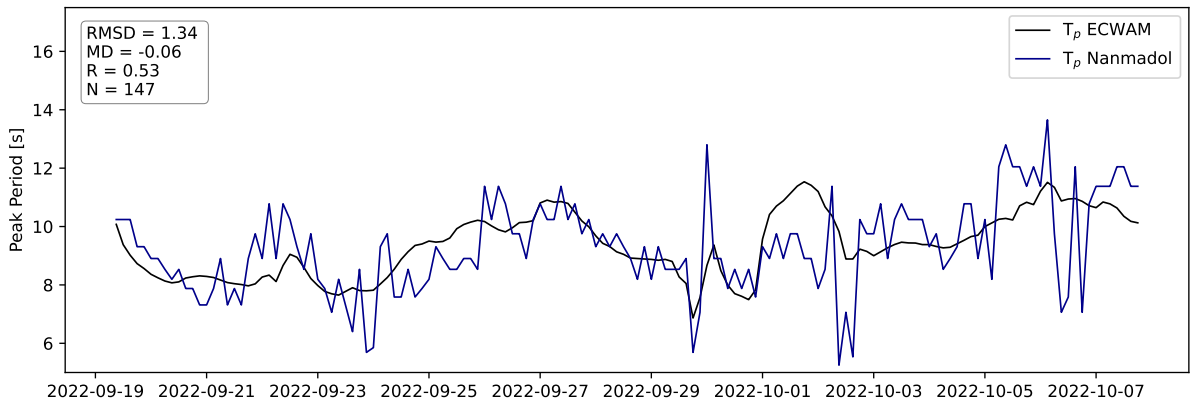


(c)

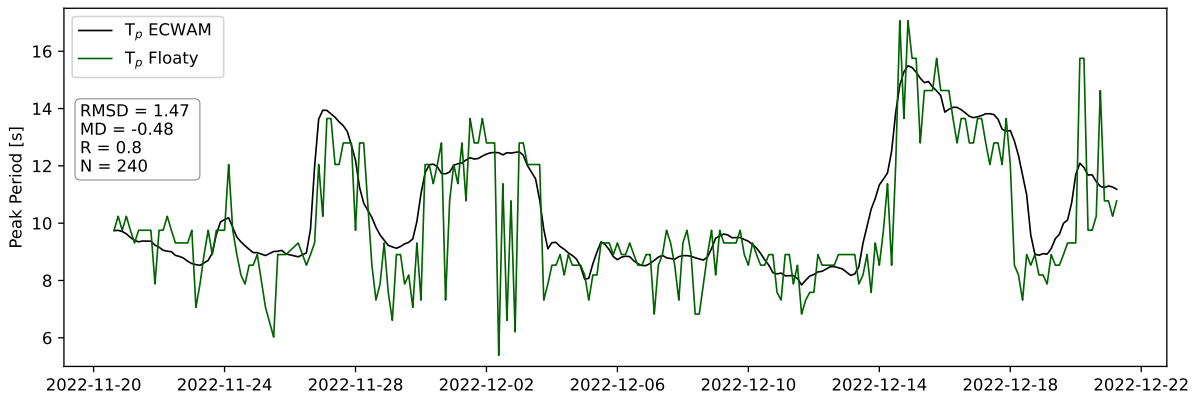


(d)

Figure 28: Significant wave height (a-b) and peak period (c-d) measured by the drifters Nanmadol (blue) and Floaty (green) compared to ECWAM and satellite data.

The peak period measured by the drifters fluctuates more than the ECWAMs estimation, shown in Figure 28c and 28d, even though both parameters have the same resolution of 3 hours. The deviation is larger than the significant wave height for both drifters (1.34-1.47s), and the correlation is lower (0.53-0.80). For Nanmadol, the maximum peak period measured the 06.10.22 is 2.14s higher than the forecast value. For Floaty, the maximum value measured at 14.12.22 is 1.58s larger than the forecast value. For both drifters, the minimum periods are more than 5s lower than the peak period estimated by ECWAM. Still, the difference is significantly lower than the 14.02s difference in peak period found for the ship mounted wave system (21c).

The statistical values for significant wave height and peak period measured by the ship mounted system and the drifters are summarized in Table 15. The drifters' significant wave height has a better correlation and lower deviation than the ship mounted system, according to ECWAM. Moreover, drifter Floaty has the highest correlation for the peak period, the ship mounted system has the second highest, while drifter Nanmadol has the lowest correlation. This indicates that it is generally hard to estimate the peak period. According to satellite data, the significant wave height measured by the ship mounted system has the highest correlation, but there are too few satellite values collocated with the drifters to trust these results.

Table 15: Statistical values of the significant wave height and peak period measured by the ship mounted system (ug2 and IMU) and the wave measuring drifters Nanmadol and Floaty compared to ECWAM and satellite data.

| | | ECWAM | | | Satellite | | |
|---|---|---|---|---|---|---|---|
| | | Ship mounted | Nanmadol | Floaty | Ship mounted | Nanmadol | Floaty |
| Significant wave height | RMSD [m] | 0.53 | 0.29 | 0.20 | 0.36 | 0.45 | 0.14 |
| | MD [m] | 0.17 | -0.12 | -0.10 | 0.15 | 0.10 | 0.01 |
| | R | 0.93 | 0.96 | 0.95 | 0.96 | 0.87 | 0.92 |
| | R | 3050 | 147 | 240 | 56 | 16 | 8 |
| Peak Period | RMSD [s] | 2.71 | 1.34 | 1.47 | | | |
| | MD [s] | 0.06 | -0.06 | -0.48 | | | |
| | R | 0.60 | 0.53 | 0.80 | | | |
| | N | 3049 | 147 | 240 | | | |

# 5 Discussion

The measurements from the ship mounted system fit well with satellite and ECWAM data for significant wave height but have a larger deviation for peak periods. The reasons for discrepancies between the data sets will be discussed further in the following.

## 5.1 Measurement Errors

The ship mounted system consists of multiple sensors at different locations on the ship (Figure 1), combined to obtain the best results. Therefore both the sensor type and position of the sensor are evaluated.

Firstly, the three altimeter probes are evaluated. Knoblauch, 2022 expected the radar probe to give better results but found no advantage with the radar probe over the ultrasonic probe. I found that both ultrasonic probes have a better fit with satellite and ECWAM than the radar probe (Table 10). The radar probe has a larger standard deviation than the ultrasonic probes and some unrealistic outliers (Figure 19b). I also found that the radar probe had an inverted fluctuation and higher mean value than ug2, even though they are mounted at the same location (Figure 17b). This error may be introduced by the instrument or the analog-to-digital electronics involved. It is possible that the ultrasonic probes are inverted instead of the radar, but the steep crests and shallow troughs measured by the radar and IMU indicate that the inverted radar fluctuation is correct (Figure 25). However, the wave properties are calculated from the fluctuation from the mean, and the sign of the fluctuation is not important as long as the altimeter probes and IMU balance each other instead of amplifying, as originally performed by the radar (Figure 17c).

There might be several reasons why the ultrasonic probe functions better than the radar probe in this study. Firstly, the ship is built of metal, so the radar may record nontrivial reflections of radar waves on the ship's hull instead of the sea surface. Secondly, the radar has a 32% smaller footprint diameter at the sea surface than the ultrasonic probe at their maximum distance range. A smaller footprint should measure the distance at one location more accurately than a large footprint. However, the average over a larger footprint may be more robust at measuring sea surface fluctuations from a moving platform. It should be noted that the radar shows more realistic fluctuations during the storm Izzy than the ultrasonic probes (Figure 25c), which argues that the smaller footprint may be an advantage during rough sea conditions. Lastly, the radar could potentially perform better if inversion of the fluctuation were not required.

The ultrasonic probe at the starboard side of the bow (ug2) has a better fit with the ECWAM and satellite data than the ultrasonic probe at the bowsprit (ug1) (Table 10). There may be some small differences between the electronics of ug1 and ug2, but their location with different heights and accelerations is probably the main reason for the discrepancy. The ug1 probe has larger fluctuations than ug2 (Figure 19a), which are not adequately compensated by the IMUs. Surprisingly, only the ug2 in combination with IMU, gives better results than IMU solely. The combination of an altimeter probe paired with an IMU was expected to perform better, but the radar and ug1 measurements are too contaminated (Table 8).

Therefore I do recommend placing the ultrasonic probe further back on the bowsprit, where the magnitude of motion is smaller, also argued by Knoblauch, 2022. He argued further that measurements too close to the ship would are disturbed by reflection at the ship's hull. However, I found this effect to impact the measurements less than the shadowing effects by the ship, which is prominent for waves with peak periods below 10s (Table 13). However, the shadowing effect is worth future investigations from sensors mounted at the bow instead of the starboard side. Moreover, the altimeter probe should be mounted as close to the surface as

possible, or have a larger range than 15.2m, to avoid saturation and increase accuracy. Since the mean height of ug1 is 11.23m, it is only 3.97m from saturating, which occurs more often for ug1 than ug2 mounted closer to the surface (Table 8).

Secondly, the three IMUs are considered. The main IMU was found to have a better fit with ECWAM and satellite data than the extra IMUs, both solely and in combination with altimeter probes (Table 10). The extra IMUs have a larger standard deviation than the main IMU for all properties (Table 9). Knoblauch, 2022 also found that the recordings made by the extra IMUs are subject to more errors than the main IMU recordings. There might be some differences between the instruments, but the impact of wind and waves causing vibrations is probably the main reason for the extra IMU errors. These impacts are avoided inside the ship or by building a more robust, heavy, and well-fastened enclosure for the IMUs.

For ug1, we did expect the extra IMU1 at the bowsprit to resemble the motion of ug1 better than the main IMU. But, according to ECWAM, the result is slightly better in combination with the main IMU (Table 10). This indicates that the 19.95m horizontal and 4.82m vertical distance is sufficient to resemble the motion of ug1 without including compensating terms as Løken et al., 2021. In addition, the extra IMU0 has a higher correlation and lower deviation than the extra IMU1, even though the sensors are identical. This confirms that the bowsprit tip is experiencing very large motion amplitudes that are not representative of the sea surface fluctuation.

Therefore, I do not recommend placing the IMU at the exact altimeter probe location unless the IMU is very well protected. The two IMUs mounted at exposed locations were protected in waterproof casing but were still destroyed after 3 and 8 months, which caused errors in the measurement system. In contrast, Knoblauch, 2022 recommends mounting the IMUs directly at the altimeter probe locations. He argues that the distance between IMU and the altimeter probe is the primary error source because the motion of the probes is not adequately accounted for. Instead, I found the main errors to be related to the post-processing (Section 4.2). Moreover, the IMUs need to be mounted as horizontally and aligned with the ship axis as possible to avoid correcting the offset angles with post-processing (Section 4.2.2).

The position of the instruments must be adapted to the ship's construction. The bowsprit is not an available option on regular vessels. Instead, Christensen et al., 2013 mounted the altimeter probe in a steel frame extending forward from the bow. The IMUs were mounted on a mast on the bow, with 1 and 3m horizontal and vertical distance to the probe, respectively. Another option is to mount the instruments on a rigid pole extending vertically downwards from the bow or through the hawsehole on the bow. The advantage is a shorter distance to the sea surface, but the measurements were found to be contaminated by vibrations caused by the ship engines (Christensen et al., 2013; Løken et al., 2021). Cifuentes-Lorenzen et al., 2013; Lund, Zappa, et al., 2017 successfully mounted the laser altimeter and IMUs on the jack staff 10m above mean sea level. The altimeter probe was deployed with a 15°incident angle to clear the bow of the ship.

Regardless of where the instruments are mounted, the loading of the ship, and the navigation in relation to wave direction, will influence the roll and pitch values and, hence, the estimation of the surface elevation (Equation 4). Statsraad Lehmkuhl is a sailing ship and thus rolls more in the water than motoring vessels (Officer Statsraad Lehmkuhl, personal communication, October 2022). However, the ship speed of Statsraad Lehmkuhl is comparable to research vessels (Cifuentes-Lorenzen et al., 2013; Clarence O Collins, Blomquist, et al., 2016). The vessels mounted with instruments should cruise as slowly as possible, for the best quality of the wave measurements, especially for the peak period (Table 12).

Other events that cannot be controlled are sea spray in rough seas, heavy rain, and objects

passing under the sensors, such as sea mammals and floating plastic pollution. For future work, these uncertainties can be compensated by applying proper filtering methods. In this thesis, no filtering has been applied beyond limiting the frequency range (0.05-0.5Hz) and the maximum distance measured by the radar (15.8m). I have found that the altimeter probe measurements are the main cause of outliers, while the IMU measurements are reliable (Figure 25 and Table 9). However, filtering needs to consider the combination of the altimeter probe and IMU measurements at the same time instance to avoid shifting the components relative to each other. This shift proved to be a major complication in the original post-processing procedure (Figure 20).

### 5.1.1 Effect of Doppler Shift

The Doppler effect correction requires a lot of post-processing and additional data but does not improve the results as expected. Doppler shifting the significant wave height lowers the MD by 0.14m, but the RMSD is 0.12m higher and the correlation coefficient 0.1 lower, compared to ECWAM (Figure 21c and 21d). The Doppler shifted peak periods' MD is increased by 0.70s, RMSD increased by 0.15s, and the correlation coefficient lowered by 0.01. Moreover, the Doppler correction does not improve the measurements at certain speeds or wave directions. In contrast, Clarence O Collins, Blomquist, et al., 2016 found the Doppler correction to improve the peak period MD with 0.29s, RMSD with 1.11s, and the correlation coefficient by 0.3 for a ship mounted laser rangefinder.

Knoblauch, 2022 argues that the Doppler effect must be compensated to gain a realistic peak period by the ship mounted system on Statsraad Lehmkuhl. Instead, I argue that the original peak period is realistic (Section 4.3) and that the Doppler correction method needs improvements.

The first reason why the Doppler correction is not satisfied may be that high frequencies in the wave spectrum are cut off when sailing with waves, as Statsraad Lehmkuhl mainly is (Figure 26d). Figure 29a illustrates the Doppler shifted wave spectrum compared to the original wave spectrum the 22.10.21, already shown in Figure 14b.

Frequencies are excluded when the square root of Equation 12 becomes negative:

$$-v_o > \frac{g}{8\pi f_o} \tag{23}$$

The cutoff only occurs for negative velocities $v_o$ in the range (-7.80m/s, -0.78m/s) for the respective range of $f_o$ (0.05Hz, 0.5Hz). For the example in Figure 29a, the ship speed is 3.40m/s, and wave direction relative to the ship is 196°, corresponding to an observers velocity $v_o$ of -3.26m/s (Equation 7). Frequencies above 0.12Hz are excluded because, at higher frequencies, the observer's velocity needs to be larger than -3.26m/s to satisfy Equation 23. Therefore the maximum value retained in the Doppler shifted spectrum is 0.2Hz, instead of the original maximum frequency of 0.5Hz. For positive $v_o$ i.e., sailing into waves, the square root never becomes negative. Therefore the cutoff is only present when sailing with waves. On the other hand, it should not impact the peak period because the peak period is usually found in the low-frequency range, which is retained. Instead, it may contribute to the negative effect on the Doppler shifted significant wave heights.

The second reason for the uncorrected Doppler effect may be related to the assumptions in the derivation of Equation 12. We assume the phase speed of the waves to be decided by the gravitational constant and the angular frequency. This simplification is only valid in deep water but is used at all times, also when the ship is sailing in the proximity of land. We also

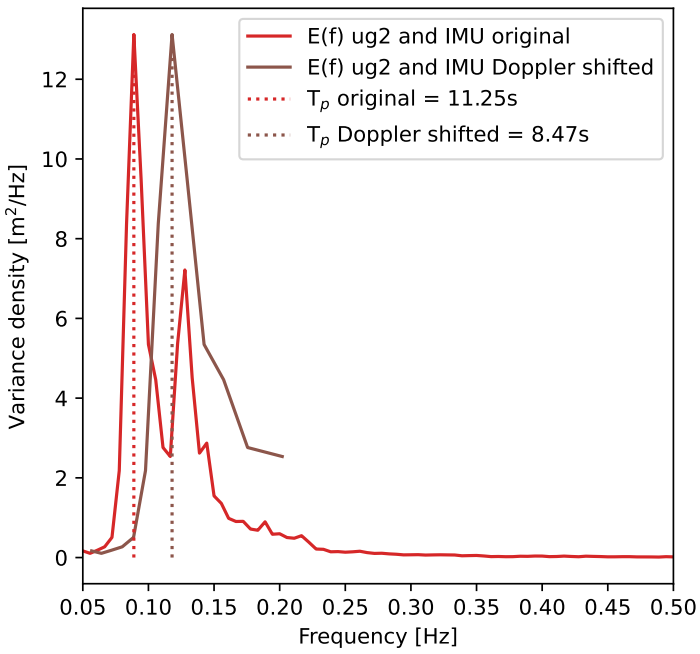


(a)

Figure 29: The variance density spectrum over 30 minutes the 22.10.21 00:00 for original (red) and Doppler shifted (brown) frequencies and the corresponding peak periods ($T_p$).

assume that no ocean currents are present. Additional data on ocean depth, current speed- and direction will be needed to include the effect of shallow water and ocean currents.

Other reasons why the Doppler correction is not satisfied may be related to uncertainties in the data for ship speed, ship heading, and wave direction. The mean wave direction does not always represent a realistic sea state (Figure 24c). For future work, the ship mounted system should be combined with a marine navigation X-band radar to obtain high-resolution wave direction, current speed, and current direction, also suggested by Lund, Zappa, et al., 2017. The additional data on coordinates, ship speed, and heading can be read from the ship's system and stored together with the wave measurements. With proper post-processing routines, this combination would also allow broadcasting the Doppler shifted peak period, as already is done for the significant wave height.

## 5.2 Model and Satellite Errors

It may be argued that comparing a new measurement method and model data cannot properly validate either product. A comparison with in situ measurement, particularly the wave measuring drifters, would be desirable but unavailable in this study at the same time and location. Instead, wave model data provides wave parameters near the ship location at any time. But models are based on discretized equations, parameterizations, and numerical techniques that introduce uncertainties (Warner, 2014).

The wave model ECWAM is regularly evaluated against observations from about 400 buoys and platforms (Haiden et al., 2019). Table 16 shows the RMSD and MD for significant wave height and peak period estimated from the figures of the last four reports [19]. One report is published for three months, i.e., SON is for September, October, and November. The maximum RMSD for significant wave height is found in DJF, 0.18m lower than in comparison with the ship mounted instrument (Figure 21b). The MD is positive, meaning that ECWAM overestimates the wave height, opposite to my findings. Ponce De León and Guedes Soares, 2012 found a correlation coefficient of 0.84-0.94 for the WAM model forced with ECMWF reanalysis wind data during a severe winter period in the seas around Norway. This is similar to the correlation coefficient of ECWAM compared to the ship mounted system of 0.93 (Figure 21b).

For peak periods, the maximum RMSD in SON is notably 0.71s smaller than the results in this thesis. However, the RMSD for ship speeds lower than 3m/s with waves opposing the sensor or ship at station (1.76-2.04s) is comparable to the values in Table 16. ECWAM generally underestimates peak periods, which also occur for the long periods measured by the ship mounted system (Figure 21c). Spectral wave models tend to overestimate the short peak periods and underestimate the long peak periods (Bidlot et al., 2002). Table 16 quantifies that the significant wave height has higher accuracy than the peak period, as suspected by the ship mounted and drifter measurements (Table 15).

Table 16: Verification values of ECWAM compared to about 400 buoys and platforms [19]. The capital letters represent three months, i.e., SON is September, October, and November.

| Parameter | Time period | RMSD | MD |
|---|---|---|---|
| Significant Wave Height [m] | SON 2021 | 0.25-0.30 | 0-0.05 |
| | DJF 2021/2022 | 0.30-0.35 | 0-0.05 |
| | MAM 2022 | 0.20-0.25 | 0-0.05 |
| | JJA 2012 | 0.15-0.20 | 0-0.05 |
| Peak Period [s] | SON 2021 | 1.90-2.00 | 0- 0.20 |
| | DJF 2021/2022 | 1.40-1.50 | 0-(-0.20) |
| | MAM 2022 | 1.40-1.50 | 0-(-0.20) |
| | JJA 2022 | 1.70-1.80 | 0-(-0.20) |

Satellite altimetry is also regularly validated against in situ wave buoys (Taburet et al., 2022), with statistics for the relevant satellite missions listed in Table 17. The RMSD is the largest for HaiYang-2B, 0.03m smaller than the comparison with the ship mounted measurements. The MD is positive for all missions, meaning that the satellite altimeter overestimates. This is opposite to what is found in my results, but with a similar magnitude (0.15m). The correlation coefficient compared to in situ wave buoys is 0.96, 0.96, 0.98 for CryoSat-2, Sentinel-3A, and Sentiel-3B, respectively (Abdalla, 2014; Yang and Zhang, 2019), identical to the ship mounted systems correlation coefficient of 0.96.

The ship mounted wave measurements better fit with satellite altimetry than the wave model ECWAM. This is expected since the altimetry product is already quality controlled, monitored,

[19] `https://confluence.ecmwf.int/display/WLW`

inter-calibrated, and filtered for noise (Taburet et al., 2022). The peak period from remote sensing techniques would complement the peak period from model data but is not as readily available as the altimeter product. Although the peak period is not available from the altimeter, it has become available with other remote sensing techniques in recent years. Several C-band SARs are equipped with wave mode providing directional wave spectra (Wang et al., 2021). Also, the Surface Waves Investigation and Monitoring instrument (SWIM) carried by CFOSAT is designed to measure the spectral properties of surface ocean waves (Hauser et al., 2020).

Table 17: Validation statistics of significant wave height for Level-3 satellite altimeter products compared to in situ data (Taburet et al., 2022).

| Parameter | Satellite Name | RMSD | MD |
|---|---|---|---|
| Significant Wave Height [m] | CryoSat-2 | 0.20 | 0.09 |
| | Sentinel-3A | 0.22 | 0.08 |
| | Sentinel-3B | 0.21 | 0.08 |
| | HaiYang-2B | 0.33 | 0.10 |
| | CFOSAT | 0.21 | 0.11 |
| | Sentinel-6A | 0.23 | 0.07 |

# 6 Conclusion

This thesis evaluates the design and post-processing aspects of the wave measurement system deployed on the sailing ship Statsraad Lehmkuhl. The wave measurement system combines downward facing altimeter probes with inertial motion units to estimate the sea surface fluctuation as a time series.

Software updates were developed and implemented based on the work presented by Knoblauch, 2022, resulting in significantly improved alignment with satellite and model data. Several errors were identified, including the misinterpretation of roll as pitch values, an inverted fluctuation in one of the altimeter probes, and distance measurements not synchronized with motion measurements. The post-processing procedure was further simplified by eliminating unnecessary and time-consuming calculations. It was determined that the main inertial measurement unit yielded better results than function fitting the motion of the extra inertial measurement units. Additionally, it was deemed unnecessary to correct offset roll, pitch, and yaw angles.

The software developments have yielded statistical results comparable to those obtained from wave measuring drifters. The root mean squared deviation for significant wave height is 0.36m and 0.53m compared to satellite altimetry and ECWAM model data, respectively. The correlation coefficients are 0.96 and 0.93 when compared to the same datasets. The best fit is observed for significant wave heights below 6m. The system tends to overestimate the largest wave heights, particularly during extreme events such as the major winter storm Izzy in the North Atlantic Ocean. Therefore, caution should be exercised when interpreting freak wave occurrences. For future work, appropriate filtering of the altimeter probe measurements may resolve the overestimation issue.

Regarding the peak period, the ship mounted system exhibits a relatively high root mean squared deviation of 2.71s and a low correlation coefficient of 0.60 compared to the wave model ECWAM. The statistics are only comparable to wave measuring drifters when the ship's speed is below 3m/s with the sensor facing the waves or when the ship is at station. In such scenarios, the root mean squared deviation ranges from 1.76s to 2.04s, and the correlation coefficients range from 0.77 to 0.80 compared to ECWAM. The method employed for Doppler shifting the peak periods did not yield satisfactory results. However, if combined with a navigation X-band radar, the method may perform better, providing directional wave- and current measurements.

For future work, the instrumentation and positioning on the ship should be carefully selected. In this study, the best results were obtained with the combination of an ultrasonic sensor placed on the starboard side of the bow along with an IMU protected below deck. It is worth noting that the IMUs do not necessarily need to be placed directly at the altimeter probe locations. Instead, they should be shielded from potential impacts caused by wind and waves. It should also be highlighted that the shadowing effect by the ship's hull caused waves towards the ship's port side to be obstructed. However, the long waves with peak periods exceeding 10 seconds remained unaffected by this shadowing effect.

The findings of this study indicate that significant wave height obtained from ship mounted instruments is suitable for real-time broadcasting during research expeditions and conventional shipping routes. Furthermore, the significant wave height measurements can serve as calibration and validation of remote observations and have the potential for assimilation into forecast models. The system has demonstrated effective and reliable operation over six months, even in rough sea conditions. I recommend deploying wave measuring devices on multiple ships and floating offshore structures to explore the capabilities of such systems across different platforms and oceanic regions. Expanding the network of offshore observations will contribute to a

deeper understanding of the ocean-atmosphere interface and enhance the safety and efficiency of offshore operations.

# References


Abdalla, Saleh (2014). "Active techniques for wind and wave observations: radar altimeter." In: *Seminar on Use of Satellite Observations in Numerical Weather Prediction, 8-12 September 2014*, pp. 1–18. URL: https://www.ecmwf.int/node/7618.

Amador, Andre, Sophia T. Merrifield, and Eric J. Terrill (2022). "Assessment of Atmospheric and Oceanographic Measurements from an Autonomous Surface Vehicle." In: *Journal of Atmospheric and Oceanic Technology* 40.3, pp. 305–326. ISSN: 0739-0572. DOI: 10.1175/JTECH-D-22-0060.1.

Aviso (2022). *Pulses and waveforms*. URL: https://www.aviso.altimetry.fr/en/techniques/altimetry/principle/pulses-and-waveforms.html (visited on 02/02/2022).

Bidlot, Jean Raymond (2016). "Ocean wave model output parameters." In: p. 27. URL: https://confluence.ecmwf.int/download/attachments/59774192/wave_parameters.pdf?version=1modificationDate=1470841648343api=v2.

Bidlot, Jean Raymond et al. (2002). "Intercomparison of the performance of operational ocean wave forecasting systems with buoy data." In: *Weather and Forecasting* 17.2, pp. 287–310. ISSN: 08828156. DOI: 10.1175/1520-0434(2002)0173C0287:IOTPOO3E2.0.CO;2.

Bohlinger, Patrik, Øyvind Breivik, et al. (2019). "A novel approach to computing super observations for probabilistic wave model validation." In: *Ocean Modelling* 139.February, p. 101404. ISSN: 14635003. DOI: 10.1016/j.ocemod.2019.101404.

Bohlinger, Patrik, Theodoros Economou, et al. (2023). "A general framework to obtain seamless seasonal–directional extreme individual wave heights—Showcase Ekofisk." In: *Ocean Engineering* 270.December 2022, p. 113535. ISSN: 00298018. DOI: 10.1016/j.oceaneng.2022.113535.

Christensen, Kai Håkon et al. (2013). "Surface wave measurements using a ship-mounted ultrasonic altimeter." In: *Methods in Oceanography* 6, pp. 1–15. ISSN: 22111220. DOI: 10.1016/j.mio.2013.07.002.

Cifuentes-Lorenzen, Alejandro et al. (2013). "A multisensor comparison of ocean wave frequency spectra from a research vessel during the southern ocean gas exchange experiment." In: *Journal of Atmospheric and Oceanic Technology* 30.12, pp. 2907–2925. ISSN: 07390572. DOI: 10.1175/JTECH-D-12-00181.1.

CNES and CNSA (2012). *CFOSAT (Chinese-French Oceanography Satellite)*. URL: https://www.eoportal.org/satellite-missions/cfosat#mission-capabilities (visited on 05/14/2022).

Collins, Clarence O, B. Blomquist, et al. (2016). "Doppler Correction of Wave Frequency Spectra Measured by Underway Vessels." In: *Journal of Atmospheric and Oceanic Technology* 34.2, pp. 429–436. ISSN: 0739-0572. DOI: https://doi.org/10.1175/JTECH-D-16-0138.1.

Collins, Clarence O, W Erick Rogers, et al. (2015). "In situ measurements of an energetic wave event in the Arctic marginal ice zone." In: *Geophysical Research Letters* 42, pp. 1–8. DOI: 10.1002/2015GL063063.

Donlon, Craig J. et al. (2021). "The Copernicus Sentinel-6 mission: Enhanced continuity of satellite sea level measurements from space." In: *Remote Sensing of Environment* 258.March. ISSN: 00344257. DOI: 10.1016/j.rse.2021.112395.

Drennan, William et al. (1994). "Directional Wave Spectra from a Swath Ship at Sea." In: *Journal of Atmospheric and Oceanic Technology* 11.4, pp. 1109–116. DOI: 10.1175/1520-0426(1994)0113C1109:DWSFAS3E2.0.CO;2.

Dysthe, Kristian, Harald E Krogstad, and Peter Müller (2008). "Oceanic Rogue Waves." In: *Annual Review of Fluid Mechanics* 40.1, pp. 287–310. DOI: 10.1146/annurev.fluid.40.111406.102203.

ECMWF (2021a). *Forecast User Guide - Ocean Wave Model ECWAM*. URL: https://confluence.ecmwf.int/display/FUG/2.2+Ocean+Wave+Model+-+ECWAM (visited on 02/02/2022).
– (2021b). "IFS DOCUMENTATION – Cy47r3 Operational implementation 12 Oct 2021 PART VII : ECMWF WAVE MODEL." In: pp. 1–110. URL: https://www.ecmwf.int/en/elibrary/81274-ifs-documentation-cy47r3-part-vii-ecmwf-wave-model.
– (2022). *Ocean Wave Model high resolution 10-day Forecast (Set II - HRES-WAM)*. URL: https://www.ecmwf.int/en/forecasts/datasets/set-ii (visited on 02/02/2022).
Gulev, Sergey K., David P. Cotton, and Andreas Sterl (1998). "Intercomparison of the North Atlantic wave climatology from voluntary observing ships, satellite data and modelling." In: *Physics and Chemistry of the Earth* 23.5-6, pp. 587–592. ISSN: 00791946. DOI: 10.1016/S0079-1946(98)00075-5.
Haddon, Sarah (2015). *Sea State and Swell*. URL: https://blog.metservice.com/Sea_State_and_Swell (visited on 05/10/2022).
Haiden, Thomas et al. (2019). *WMO Lead Centre for Wave Forecast Verification established at ECMWF*. URL: https://www.ecmwf.int/en/newsletter/161/news/wmo-lead-centre-wave-forecast-verification-established-ecmwf.
Hauser, Danièle et al. (2020). "New observations from the SWIM radar on board CFOSAT : instrument validation and ocean wave measurement assessment." In: 59.1, pp. 5–26. DOI: 10.1109/TGRS.2020.2994372.
Holthuijsen, Leo H (2007a). "Chapter 2 - Observation techniques." In: *Waves in Oceanic and Coastal Waters*. Cambridge University Press, pp. 10–23. DOI: 10.1017/CBO9780511618536.003.
– (2007b). "Chapter 3 - Description of ocean waves." In: *Waves in Oceanic and Coastal Waters*. Cambridge University Press, pp. 24–55. DOI: 10.1017/CBO9780511618536.004.
– (2007c). "Chapter 4 - Statistics." In: *Waves in Oceanic and Coastal Waters*. Cambridge University Press, pp. 56–105. DOI: 10.1017/CBO9780511618536.005.
– (2007d). "Chapter 5 - Linear wave theory (oceanic waters)." In: *Waves in Oceanic and Coastal Waters*. Cambridge University Press, pp. 106–144. DOI: 10.1017/CBO9780511618536.006.
Jiang, Liguang et al. (2017). "CryoSat-2 altimetry applications over rivers and lakes." In: *Water* 9.3. ISSN: 20734441. DOI: 10.3390/w9030211.
Knoblauch, Fabian (2022). "Measurement of Wave Properties with a Custom Built Sensor System as Part of the One Ocean Expedition (2021-2023)." In: Master's Thesis at The Univeristy of Oslo.
Løken, Trygve K. et al. (2021). "Wave measurements from ship mounted sensors in the Arctic marginal ice zone." In: *Cold Regions Science and Technology* 182.November 2019. ISSN: 0165232X. DOI: 10.1016/j.coldregions.2020.103207.
Lund, Björn, Clarence O. Collins, et al. (2016). "Multi-directional wave spectra from marine X-band radar." In: *Ocean Dynamics* 66.8, pp. 973–988. ISSN: 16167228. DOI: 10.1007/s10236-016-0961-z.
Lund, Björn, Christopher J. Zappa, et al. (2017). "Shipboard wave measurements in the Southern Ocean." In: *Journal of Atmospheric and Oceanic Technology* 34.9, pp. 2113–2126. ISSN: 15200426. DOI: 10.1175/JTECH-D-16-0212.1.
Malila, Mika P. et al. (2022). "A Nonparametric, Data-Driven Approach to Despiking Ocean Surface Wave Time Series." In: *Journal of Atmospheric and Oceanic Technology* 39.1, pp. 71–90. ISSN: 15200426. DOI: 10.1175/JTECH-D-21-0067.1.
Ochi, Michel K (1998a). "Chapter 2 - Spectral analysis." In: *Ocean Waves: The Stochastic Approach*. Cambridge Ocean Technology Series. Cambridge University Press, pp. 13–57. DOI: 10.1017/CBO9780511529559.003.

Ochi, Michel K (1998b). "Chapter 3 - Wave amplitude and height." In: *Ocean Waves: The Stochastic Approach*. Cambridge Ocean Technology Series. Cambridge University Press, pp. 58–102. DOI: 10.1017/CBO9780511529559.004.

Passaro, Marcello et al. (2014). "ALES: A multi-mission adaptive subwaveform retracker for coastal and open ocean altimetry." In: *Remote Sensing of Environment* 145, pp. 173–189. ISSN: 00344257. DOI: 10.1016/j.rse.2014.02.008.

Pettersson, Heidi et al. (2003). "Directional wave measurements from three wave sensors during the FETCH experiment." In: *Journal of Geophysical Research: Oceans* 108.3, pp. 1–15. ISSN: 21699291. DOI: 10.1029/2001jc001164.

Ponce De León, S. and C. Guedes Soares (2012). "Distribution of winter wave spectral peaks in the seas around Norway." In: *Ocean Engineering* 50, pp. 63–71. ISSN: 00298018. DOI: 10.1016/j.oceaneng.2012.05.005.

Rabault, Jean, Takehiko Nose, et al. (2022). "OpenMetBuoy-v2021: An Easy-to-Build, Affordable, Customizable, Open-Source Instrument for Oceanographic Measurements of Drift and Waves in Sea Ice and the Open Ocean." In: *Geosciences (Switzerland)* 12.3, pp. 1–25. ISSN: 20763263. DOI: 10.3390/geosciences12030110. arXiv: 2201.08384.

Rabault, Jean, Graig Sutherland, et al. (2020). "An open source, versatile, affordable waves in ice instrument for scientific measurements in the Polar Regions." In: *Cold Regions Science and Technology* 170.January 2019. ISSN: 0165232X. DOI: 10.1016/j.coldregions.2019.102955. arXiv: 1901.02410.

Reistad, Magnar et al. (2011). "A high-resolution hindcast of wind and waves for the North Sea, the Norwegian Sea, and the Barents Sea." In: *Journal of Geophysical Research: Oceans* 116.5, pp. 1–18. ISSN: 21699291. DOI: 10.1029/2010JC006402.

Robinson, Ian S (2004). "Chapter 11 - Radar altimeters over the ocean." In: *Measuring the oceans from space: the principles and methods of satellite oceanography*. Springer Science and Business Media, pp. 563–638. ISBN: 978-3-540-42647-9.

Sun, Jielun et al. (2005). "Measurement of directional wave spectra using aircraft laser altimeters." In: *Journal of Atmospheric and Oceanic Technology* 22.7, pp. 869–885. ISSN: 07390572. DOI: 10.1175/JTECH1729.1.

Taburet, N. et al. (2022). "Copernicus Marine Service: Quality information document." In: pp. 1–48. URL: https://catalogue.marine.copernicus.eu/documents/QUID/CMEMS-WAV-QUID-014-001.pdf.

Wang, Jiuke et al. (2021). "The Wide Swath Significant Wave Height: An Innovative Reconstruction of Significant Wave Heights From CFOSAT's SWIM and Scatterometer Using Deep Learning." In: *Geophysical Research Letters* 48.6. ISSN: 19448007. DOI: 10.1029/2020GL091276.

Warner, Thomas Tomkins (2014). "Chapter 9 - Verification methods." In: *Numerical Weather and Climate Prediction*. Vol. 48. 04, pp. 48–1788–48–1788. ISBN: 9780511763243. DOI: 10.5860/choice.48-1788.

Welch, Peter D. (1967). "The Use of Fast Fourier Transform for the Estimation of Power Spectra: A Method Based on Time Averaging Over Short, Modified Periodograms." In: *IEEE Transactions on Audio and Electroacoustics* 15.2, pp. 70–73. ISSN: 00189278. DOI: 10.1109/TAU.1967.1161901.

Wilks, Daniel S. (2011a). "Chapter 3 - Empirical Distributions and Exploratory Data Analysis." In: *Statistical Methods in the Atmospheric Sciences*. Ed. by Daniel S Wilks. Vol. 100. International Geophysics. Academic Press, pp. 23–70. DOI: https://doi.org/10.1016/B978-0-12-385022-5.00003-8.

– (2011b). "Chapter 7 - Statistical Forecasting." In: *Statistical Methods in the Atmospheric Sciences*. Ed. by Daniel S Wilks. Vol. 100. International Geophysics. Academic Press, pp. 215–300. DOI: https://doi.org/10.1016/B978-0-12-385022-5.00007-5.

Wilks, Daniel S. (2011c). "Chapter 8 - Forecast Verification." In: *Statistical Methods in the Atmospheric Sciences*. Ed. by Daniel S Wilks. Vol. 100. International Geophysics. Academic Press, pp. 301–394. DOI: https://doi.org/10.1016/B978-0-12-385022-5.00008-7.

World Meteorological Organization (2021). *Manual on the Global Data-Processing System: Global Aspects*. Vol. 1. 485. World Meteorological Organization, p. 132. ISBN: 9789263104854. URL: https://library.wmo.int/doc_num.php?explnum_id=11599.

Yang, Jungang and Jie Zhang (2019). "Validation of sentinel-3A/3B satellite altimetry wave heights with buoy and jason-3 data." In: *Sensors (Switzerland)* 19.13. ISSN: 14248220. DOI: 10.3390/s19132914.

Young, I. R. (1999). "Seasonal variability of the global ocean wind and wave climate." In: *International Journal of Climatology* 19.9, pp. 931–950. ISSN: 08998418. DOI: 10.1002/(SICI)1097-0088(199907)19:9<931::AID-JOC412>3.0.CO;2-O.

# Appendix

## A Time Series

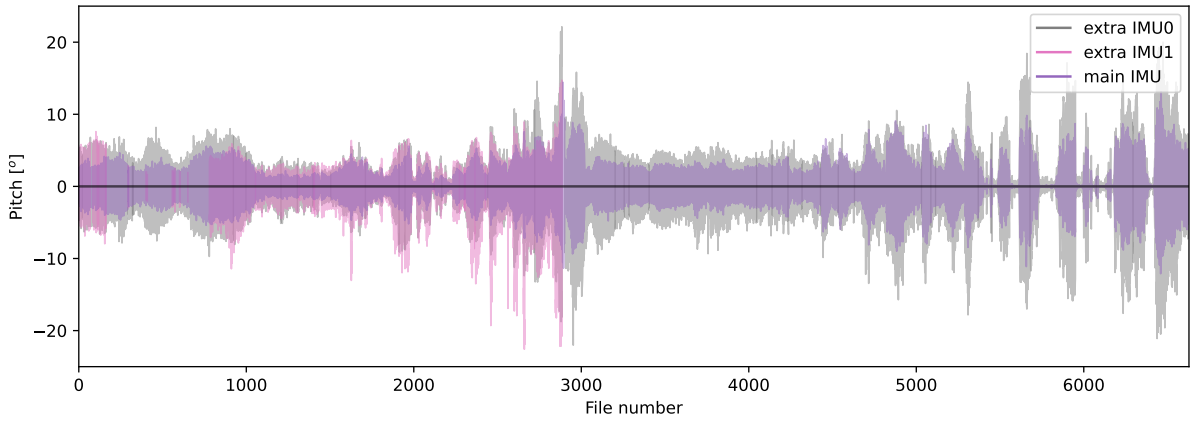


(a)

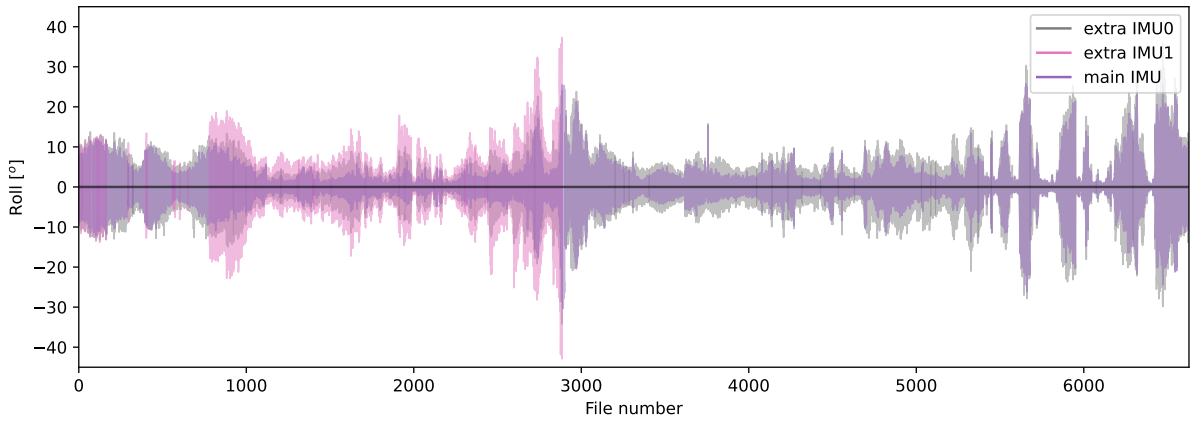


(b)

Figure 30: Minimum and maximum (a) pitch and (b) roll fluctuations (subtracted the mean) measured each 30-minute file by the three IMUs.

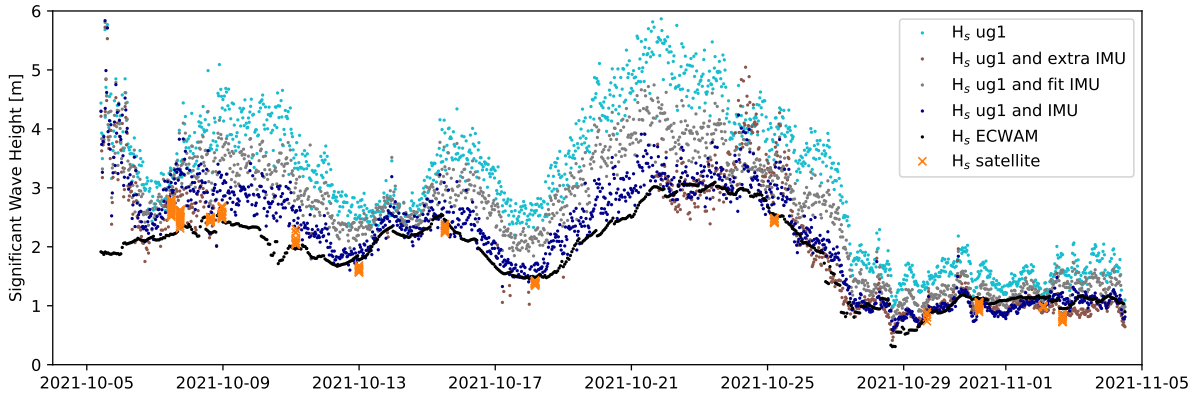


(a)

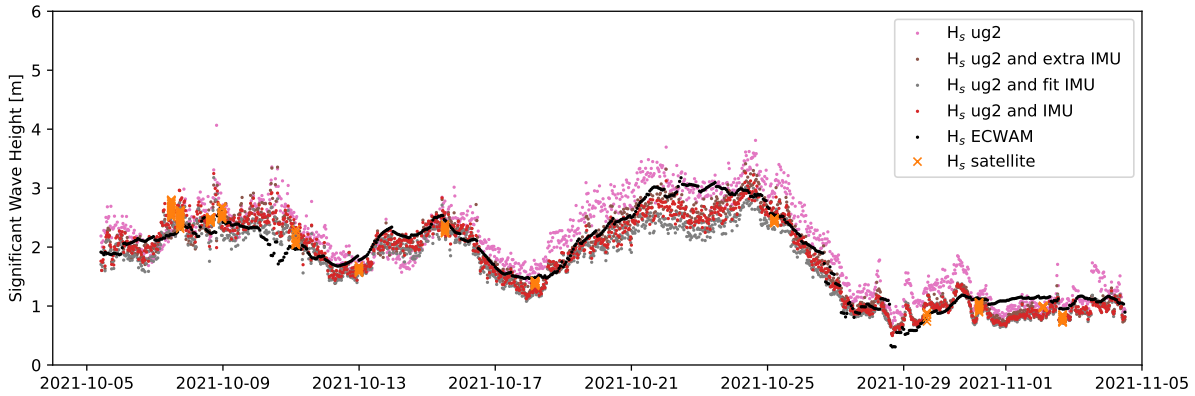


(b)

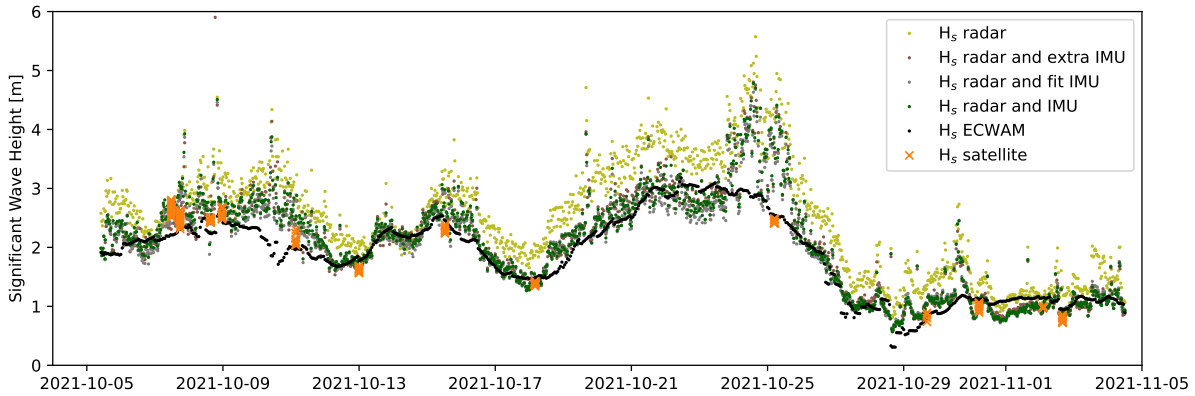


(c)

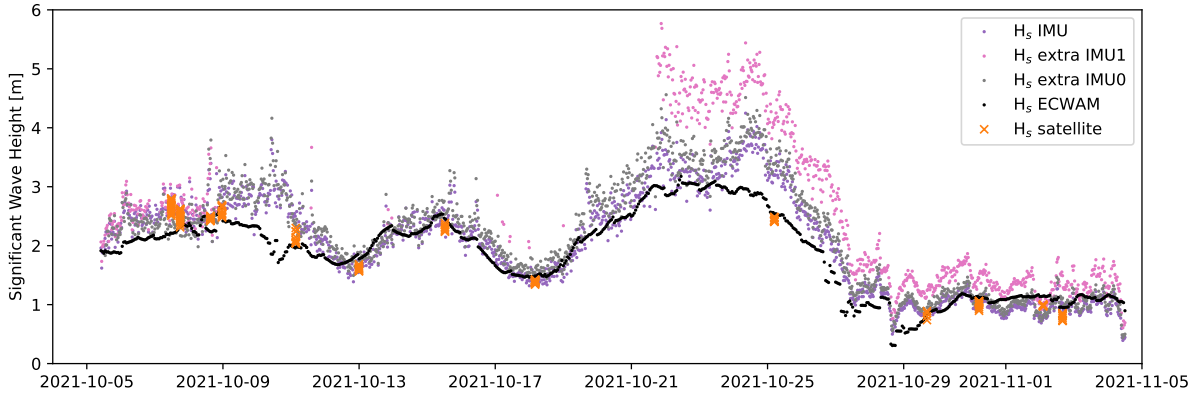


(d)

Figure 31: Significant wave height during leg 2 using different system combinations for (a) ug1, (b) ug2, (c) radar and (d) IMUs, compared to satellite and ECWAM.

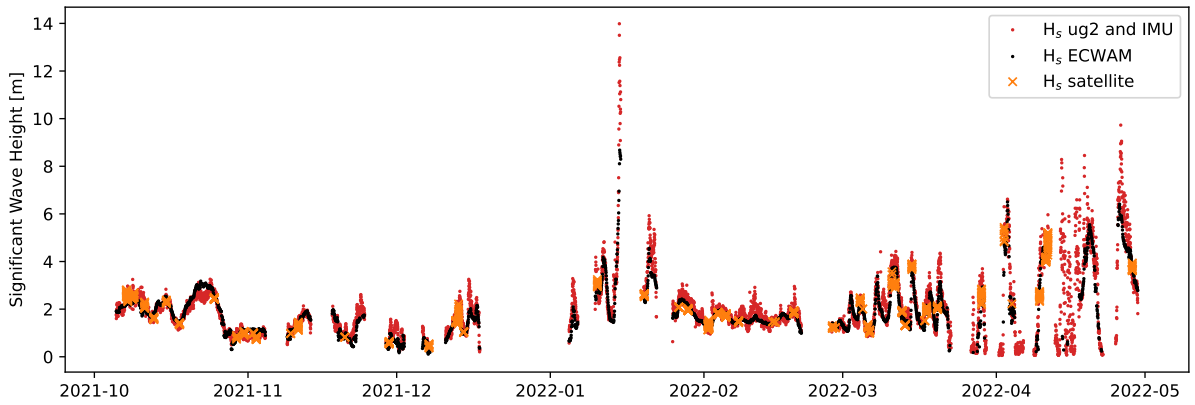


(a)

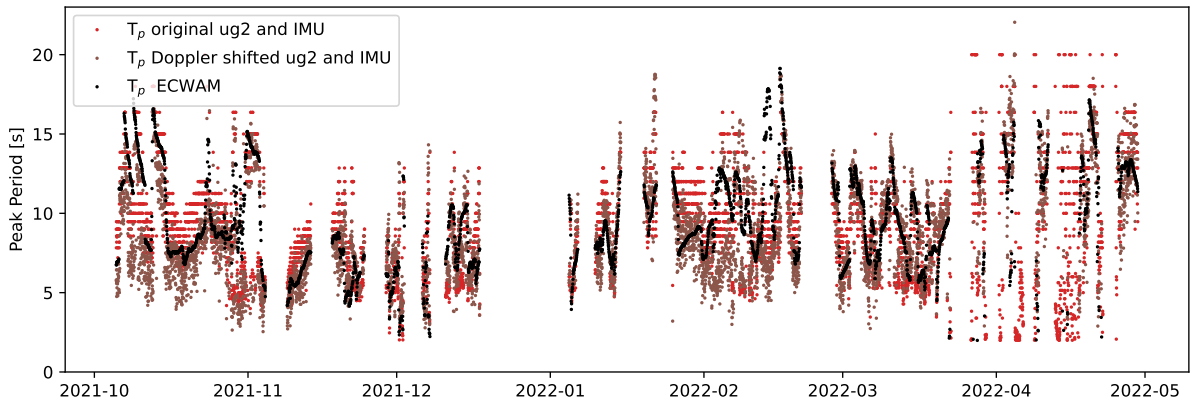


(b)

Figure 32: Significant wave height (a), original (red) and Doppler shifted (brown) peak period (b) measured by ug2 and IMU compared to satellite and ECWAM for the entire period.

# B Wind Measurements

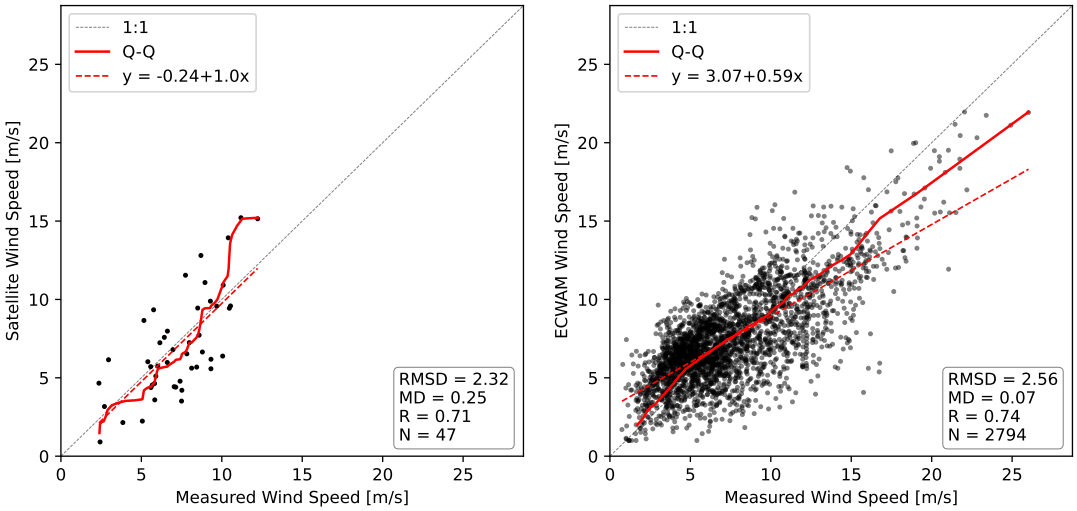


(a) (b)

Figure 33: Wind speed measured at the ship compared to satellite (a) and ECWAM (b). The solid red line is the quantile-quantile fit (Q-Q), while the red dotted line is the linear regression (y).

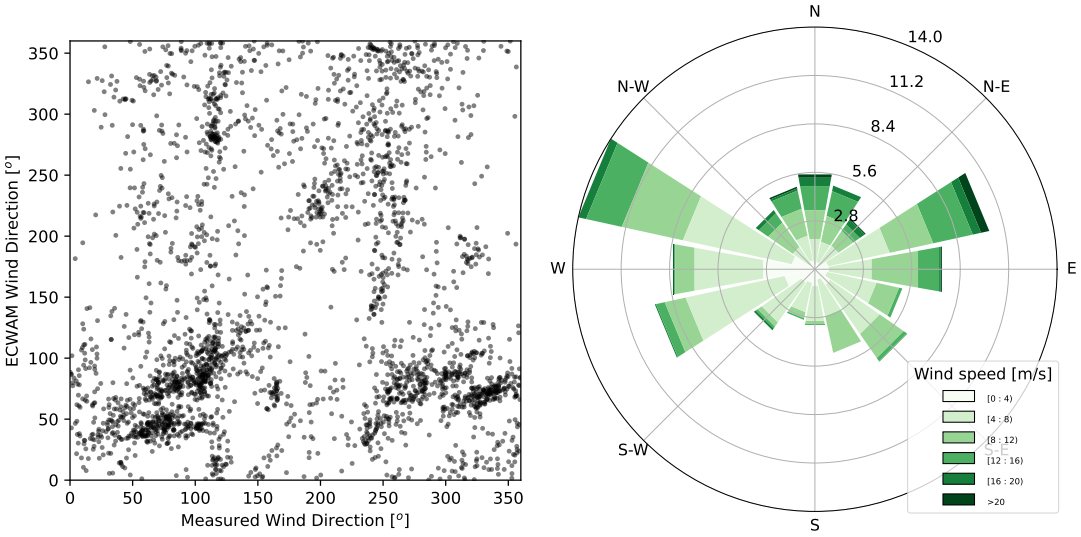


(a) (b)

Figure 34: Wind direction measured at the ship compared to ECWAMs wind direction (a) and (b) directional rose for wind direction measured at the ship. Directions are defined with oceanographic convention: going towards. The color contours represents the measured wind speed and the number represent the percentage of values within each of the 16 directional bins.

# C Scatterplot Drifter Measurements

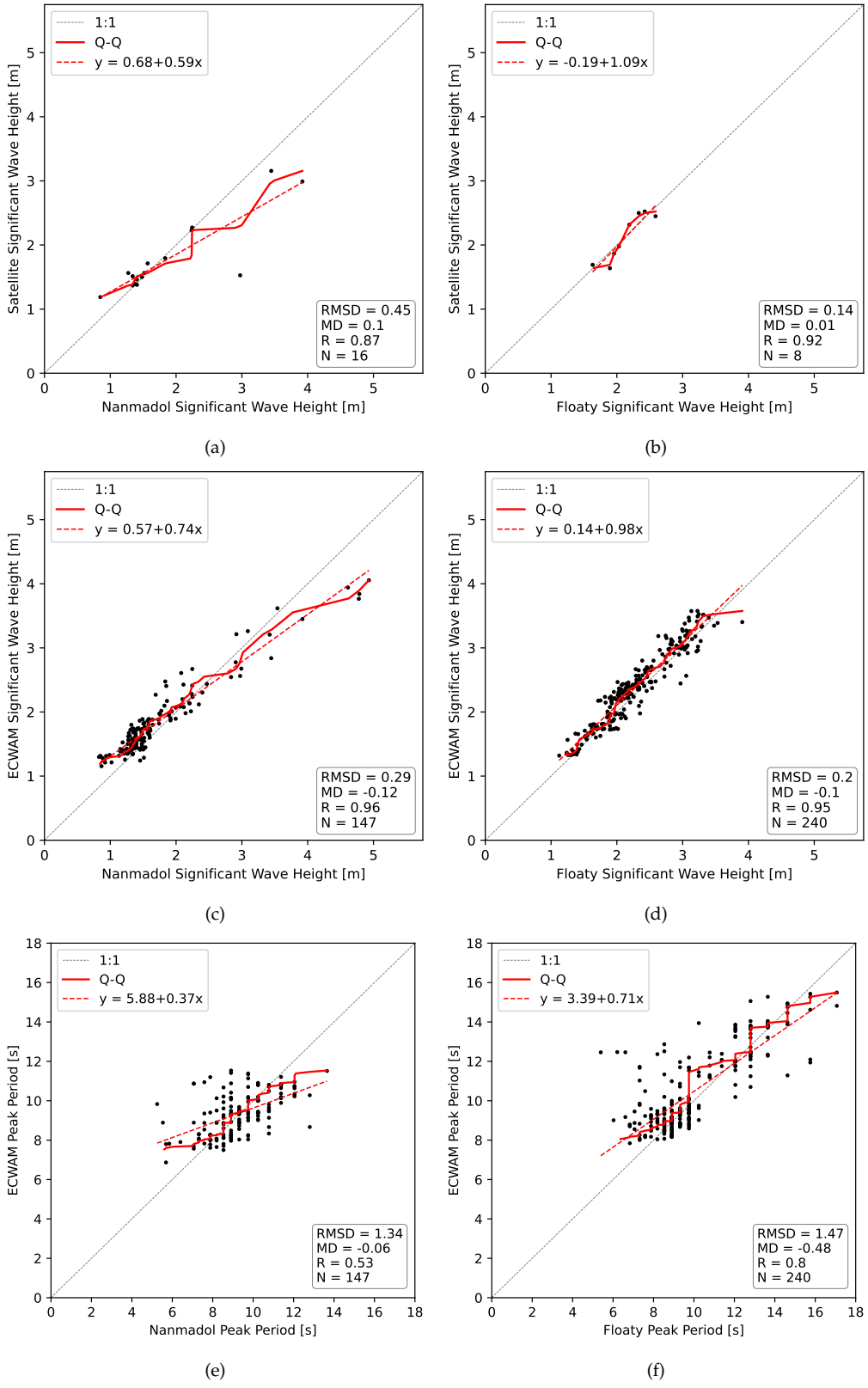


Figure 35: Significant wave height measured by the drifters Nanmadol and Floaty compared to satellite data (a-b) and compared to ECWAM (c-d), and peak period compared to ECWAM (e-f). The solid red line is the quantile-quantile fit (Q-Q), while the red dotted line is the linear regression (y).